RIDE DYNAMIC ANALYSIS OF GUIDED PNEUMATIC-TIRED SUBWAY CAR

Yasser Rafat

A Thesis

in

the Department

of

Mechanical & Industrial Engineering

Presented in Partial Fulfillment of the Requirements
for the Degree of Master of Applied Science at
Concordia University
Montreal, Quebec, Canada

June 2007

Your file Votre référence
ISBN: 978-0-494-34600-6
Our file Notre référence
ISBN: 978-0-494-34600-6

ABSTRACT

RIDE VIBRATION ANALYSIS OF A GUIDED PNEUMATIC-TIRED SUBWAY CAR

Yasser Rafat

In the Montreal metro system, the metro cars operate on pneumatic tires as opposed to the steel wheels and rail tracks used in most subway systems. This type of traction system provides relatively quieter and smoother operation. Despite the use of pneumatic tires and a very smooth concrete track, the Montreal metro cars exhibit complex vibration environment, that arises from dynamic tire-track interactions, and coupled dynamics of vehicle components, namely, axle, bogie and the car body.

In this investigation, a 23 degrees-of-freedom, three dimensional ride dynamic mathematical model of the Montreal metro car is developed to study the ride performance under deterministic as well as measured track excitations. The model integrates excitations due to left- and right track surface roughness, and wheel non-uniformity. The wheel non-uniformity is modeled as a combination of an equivalent mass unbalance and out-of-roundness of the tread geometry. The validity of the model is demonstrated by comparing the response characteristics with available measured data. The ride quality of the vehicle at operator's level is assessed in relation to the proposed guidelines upon applying the recommended frequency-weighting filters. The ride responses revealed comprehensive vertical vibration in the vicinity of 6 Hz to which the human body is known to be more sensitive. High magnitude of vertical s vibration near 6 Hz became evident at near the nominal operating speed of 60 km/h, and was associated with wheel non-uniformity and vertical mode resonance of the bogie.

The influence of variations in design and operating variables on the ride performance of the metro car is investigated through a comprehensive parametric study. The variations in operating conditions include the forward speed of the metro car and passenger load. The parametric study on design variables includes the variations in the inertial properties of the vehicle components, namely, car body, bogie and axle and variations in suspension properties. The results of the study are discussed to highlight the contributions of these parameters on the ride quality, and to identify most desirable design and operating conditions. Finally, a set of optimal parameters is identified and then comparison is made between nominal and optimal set of design parameters.

ACKNOWLEDGEMENTS

I am sincerely grateful to his supervisors, Dr. Subhash Rakheja and Dr. Rama Bhat for their help and guidance throughout the course of this research and during the preparation of this thesis. Furthermore, the financial support provided by them helped in keeping my concentration fixed to this project.

I also wish to thank CONCAVE (Concordia Computer-Aided Vehicle Engineering) Research Center, Department of Mechanical and Industrial Engineering, Concordia University, and IRSST (Institut de recherché Robert-Sauve en sante et en securite du travail). It was due to the technical data supplied by them that this project could be realized.

I would like to thank my family and all my friends, especially Asad and Shahid for supporting and encouraging me, without their help it would have been difficult.

I dedicate this thesis to the experiences which I gained during my stay in Montreal.

TABLE OF CONTENTS

LIST OF FIGURES

LIST OF TABLES

NOMENCLATURE

SYMBOL	DESCRIPTION
a	Semi-major axis of the elliptical portion of the non-uniform tire (m)
a_{lj}	Lateral spacings between the left elastomeric springs and the car body c.g., $(j = F, R)$ (m)
a_{rf}	Lateral spacings between the right elastomeric springs and the car body c.g., $(j = F, R)$ (m)
a_1, a_2 and a_3	Transverse distances of the measurement locations from the c.g of carbody, bogie and axle mass centers, respectively.
b	Semi-minor axis of the elliptical portion of the non-uniform tire (m)
b_{1i}	Longitudinal distance of inner rubber mounts with respect to c.g. of the bogie of axle i (m)
b_{2i}	Longitudinal distance of outer rubber mounts with respect to c.g. of the bogie of axle i (m)
b_{li}	Lateral spacing of the left tires of axle i (m)
b_{mi}	Longitudinal distance of motor mounts with respect to c.g. of the bogie of axle i (m)
b_{ri}	Lateral spacing of the right tires of axle i (m)
$[C]$	Damping matrix of the vehicle model
$[C_F]$	Forced damping matrix
c_{li}	Lateral spacing of the left rubber mounts of axle i (m)
c_m	Motor mount damping coefficient (kN-s/m)
c_r	Rubber mount damping coefficient (kN-s/m)
c_r'	Radial rubber mount damping coefficient (kN-s/m)
c_{ri}	lateral spacing of the right motor mounts of axle i (m)

c_s	Elastomeric spring damping coefficient (kN-s/m)
c_t	Tire damping coefficient (kN-s/m)
c_t'	Radial tire damping coefficient (kN-s/m)
c_θ	Torsion bar rotational damping coefficient (kNms/rad)
d_{li}	Lateral spacing of the left motor mounts of axle i (m)
d_{ri}	lateral spacing of the right motor mounts of axle i (m)
e_F	Longitudinal distance of the springs with respect to c.g. of the front bogie (m)
e_i^p	Eccentricity due to mass unbalance (m)
$\{E\}$	Vector of mass eccentricities
e_R	Longitudinal distance of the springs with respect to c.g. of the rear bogie, (m)
F_{ip}^m	Vertical force due to motor mount (N) ($i=1,..,4$), ($p=l,r$)
F_{ip}^n	Force due to tire-wheel assembly non-uniformity (N) ($i=1,..,4$), ($p=l,r$)
F_{ik}^r	Vertical force due to rubber mount (N) ($i=1,..,4$), $(k=1,..,4)$
F_{jp}^s	Vertical force due to elastomeric spring (N) $(j=F,R)$,($p=l,r$)
F_{ip}^t	Vertical force due to tire (N) ($i=1,..,4$), ($p=l,r$)
$F_{ip}^{t'}$	Lateral force due to tire (N) ($i=1,..,4$), ($p=l,r$)
F_{ip}^u	Force due to mass unbalance in the tire (N) ($i=1,..,4$), ($p=l,r$)
f	Excitation frequency (Hz)
f_{ni}	Natural frequency of the i^{th} mode (Hz)
f_{ndi}	Frequencies of damped oscillations (Hz)
$\{f(t)\}$	Excitation force vectors due to track roughness
$\{f^u(t)\}$	Excitation force vectors due to mass unbalance
$\{f^n(t)\}$	Excitation force vectors due to tire non-uniformity
h	Vertical distance between the axle c.g. and the track datum (m)

h_1	Vertical distance between the rubber mounts and axle c.g. (m)
h_t	Vertical distance between the rubber mount and bogie c.g. (m)
I_{ar}	Axle roll mass moment of inertia (kg m^2)
I_{bp}	Bogie pitch mass moment of inertia (kg m^2)
I_{br}	Bogie roll mass moment of inertia (kg m^2)
I_{cp}	Carbody pitch mass moment of inertia (kg m^2)
I_{cr}	Carbody roll mass moment of inertia (kg m^2)
i	Number of axles $i = 1,..,4$
$[K]$	Stiffness matrix of the vehicle model
$[K_F]$	Forced stiffness matrix
k_m	Motor mount stiffness (kN/m)
k_r	Rubber mount stiffness (kN/m)
k_r'	Radial rubber mount stiffness (kN/m)
k_s	Elastomeric spring stiffness (kN/m)
k_t	Tire stiffness (kN/m)
k_t'	Radial tire stiffness (kN/m)
k_θ	Torsion bar rotational stiffness (kNm/rad)
l_1 and l_2	Longitudinal distances of measurement locations from the carbody and bogie mass centers, respectively,
l_j	Longitudinal distance of elastomeric spring from bogie c.g. $(j = F, R)$
$[M]$	Mass matrix of the vehicle model
m_a	Axle mass (kg)
m_b	Bogie mass (kg)
m_c	Carbody mass (kg)
N_{ik}	Lateral force due to rubber mount (N) $(i = 1,..,4)$, $(k = 1,..,4)$

$\{q\}$	Vector of generalized coordinates
$\{q_o\}$	Displacement excitation vector due to track roughness
y_{bj}, y_{ai}	Lateral motions of bogie and axle
z_c, z_{bj}, z_{ai}	Vertical motions of car body, bogie and axle
$\theta_c, \theta_{bj}, \theta_{ai}$	Roll motions of car body, bogie and axle
ϕ_c, ϕ_{bj}	Pitch motions of car body and bogie
v	Forward velocity of the vehicle
r	Wheel radius of the loaded car

1 INTRODUCTION AND LITERATURE REVIEW

1.1 INTRODUCTION

Urban rail transportation system has become an essential service for the modern society. The metro system, particularly, has proven as an economical, efficient and environment friendly transportation system across major urban areas in the entire world. Additional systematic efforts have been consistently mounted to enhance the rider comfort in an attempt to promote the usage of metro transportation. These include improved ventilation, noise reduction, faster speed, more frequent service etc. In Montreal, the metro cars operate on rubber tires as opposed to the steel wheel and track used in subway system in vast majority of cities in North America. This type of traction system provides relatively quieter and smoother operation, while the pneumatic tires provide further cushioning to reduce magnitudes of ride vibration. The pneumatic tires, however, may yield increased car body roll and pitch as compared to cars rolling on steel wheels and track. The Montreal metro cars also employ lateral guiding wheels to achieve better curving performance. The interaction of these wheels with the guide rails may also cause comprehensive levels of vibration along the translational and rotational axes.

Despite the use of pneumatic tires and a very smooth concrete track, the Montreal metro cars exhibit complex vibration environment, that arises from dynamic wheel-track interactions, and coupled dynamics of axle, bogie and car body. A recent study has shown that the vibration developed along the horizontal and vertical axes mostly predominate in the 1.5-40 Hz frequency range [1]. Considerably larger levels of vertical

vibration near 6 Hz are frequently encountered. This particular vibration causes significant perception of discomfort, since the human body is most sensitive to vertical vibration in the vicinity of this frequency [53]. While such vibrations cause discomfort and annoyance among the riders who are exposed to subway environment only for a shorter duration, this may impose certain health and safety risks among the operators who are exposed for longer durations on a daily basis. A detailed ride dynamic analysis of metro cars operating with pneumatic tires could provide considerable insight into sources of vibration and thereby some guidance for attenuation of important components of vibration. Such ride dynamic analysis of metro cars has not yet been reported. Moreover, such analyses could provide additional guidance on the operating speed that would yield better rider comfort from the point of view of vibration.

The design of pneumatic-tired metro cars used in Montreal is quite similar to passenger rail vehicles, with the exception of the vehicle-track interface. The dynamic interactions between the wheel set and steel rails, and complex geometry of both the wheel set and the rail contribute to complex high-frequency contact vibration in rail vehicles, which would be considerably different for pneumatic-tired metro cars. The low frequency components of the car body vibration, however, are expected to be comparable with those of the rail.

One of the major sources of low frequency vibration excitation in metro is tire non-uniformity. The vehicle tires often exhibit non-uniformity of the tread, which may give rise to larger magnitudes of vibration, particularly when wheel angular speed is close to a vibration mode of the vehicle. Tire-wheel non-uniformities such as geometric imperfections and mass concentrations can lead to measurable dynamic tire force

variations, which has been associated with ride discomfort. Dynamic force variations due to unbalance and non uniformities occur in the vicinity of the wheel rotation frequency and higher harmonics [2]. The operating speed of the vehicle thus plays a major role in the ride responses of the vehicle.

In this dissertation research, the ride dynamics of a metro car is investigated through development and analysis of a lumped parameter model, comprising of car, bogies, wheel sets and the tires. The track surface roughness is characterized and the ride responses of the car are investigated under excitations arising from random track roughness and wheel non-uniformities. The analytical model is validated using the available field-measured data. A parametric sensitivity analysis is finally performed to identify design parameters that could provide improved control of ride vibration.

1.2 LITERATURE REVIEW

1.2.1 Ride vibration environment of subway cars

Direct long term whole body vibration, (WBV), stemming from engines and vehicles, has been recognized as a mechanical stress factor for accelerated degenerative spine disease, back pain, and prolapsed disks [54]. Although these studies did not establish a direct relation between the exposure level and back pain among subway operators, many epidemiological studies have established direct association between lower back pain and WBV exposure [58, 59]. Owing to the health and safety risks, a vast number of studies have characterized and assessed vibration environment of various vehicles. The unguided, wheeled and tracked vehicles, employed in construction, forestry, agricultural and industrial applications, have been the primary focus of these

studies due to significantly high magnitude of vibration of such vehicles. A few studies have also investigated ride vibration dynamics of rail vehicles through analysis of ride dynamic models and measurement of vibration environment. These studies have invariably shown that enhancement of passenger comfort in rail vehicle continues to be a design challenge.

Unlike the guided and unguided rail vehicles, only minimal efforts have been made for characterizing and assessing the vibration environments of subway or metro cars. The vibration related passenger comfort was perhaps not considered to be of serious concern, since the passengers generally ride the metro for relatively short duration. The exposure duration for the operator, however, could be as high as 8 hour per day, which has raised many concerns related to health and safety risks of metro vibration. These concerns have prompted a few studies on subway operator vibration during the past decade.

A study on exposure to whole body vibration environment in the New York City subway system revealed that the vertical and lateral vibration levels clearly exceed the 8-h "fatigue decrease proficiency" limits defined in the earlier version of ISO-2631 (1978) [55]. A survey of 492 subway operators conducted in 1989 concluded that nearly three fourth of operators surveyed complained of recurrent neck, back or lower back pain [56]. The vibration levels in the New York subway car were also measured in another study [54] which also confirmed that the average lateral or vertical exposure levels exceed the 8-hour exposure limit. Bongers and Boshuizen [57] found that low back disorders formed the only category of disorders that showed a statistically significant correlation with whole body vibration exposure. According to Dupuis [58], a sequence of events related to

whole body vibration exposure may lead to structural damage of lumbar spine. Vibration close to or at resonant frequencies of the spine leads to an increased spinal load which then lead to fatigue injury of the passive spinal structures [59].

Ozkaya et al. [61] reported the results of a two-year comprehensive field study conducted on train operators of the New York City (NYC) subway system. The primary purpose of the study was to measure mechanical vibrations transmitted to the train operators, in order to calculate daily whole-body vibration exposure levels. The exposure level were assessed in view of maximum acceptable exposure levels in accordance with the fatigue decreased proficiency guideline defined in ISO 2631 (1978) standard on whole-body vibration. The study also sought to identify factors that might influence mechanical vibrations transmitted to the operators and quantify their effects on the measured vibration levels. As a result of the study, 6 out of 20 subway lines were determined to have vibration levels higher than daily exposure limits provided in the ISO 2631 (1978) standard.

The studies on ride vibration of metro or subway cars have been mostly limited to analyses of the field-measured acceleration data. Such data permit for exposure assessment and the influence of operating factors, such as speed and passenger load. Only minimal information, however, could be gained on the influences of various design factors. The study by Ozkaya et al. [61] involved total of five different types of car. The analysis of measured vibration data showed nearly 31% lower overall vibration levels of cars equipped with air suspension than those with steel spring suspensions. The ride dynamic responses of a metro car can be attributed to dynamic interactions among the various major components as in the case of road and guided rail vehicles. The

development of an analytical ride model of a metro car would thus be desirable for a more systematic analysis of various influencing design factors. The reported relevant studies are thus reviewed and discussed below in order to build necessary background and formulate scope of this study.

1.2.2 Vehicle model

A wide range of vehicle models for analysis of guided as well as unguided vehicles have evolved during the past many decades. These include linear and non-linear lumped-parameter as well as continuous system models. It has been suggested that the type of vehicle model employed in a dynamic study mainly depends on frequency range of interest for a specific problem that is under investigation [3]. A common first step usually involves identification of static and dynamic properties or physical relations for the essential subsystems. Over the years, a number of analytical models of varying complexities have been developed to describe static and dynamic behaviors of the subsystems of the vehicle-terrain system [5]. The model complexity generally derives from a trade-off between the analytical complexity and simulation realism [4]. The "quarter-vehicle" and "half-vehicle" models are perhaps best examples of this trade-off, which have been most widely employed for studies on various design concepts in road vehicles. In rail vehicles, simplified single bogie or half-body models have been used to study rail-vehicle interactions, which involve a trade-off between inaccuracy and analysis efficiency [6].

The vehicle curving, stability and ride quality analyses are mostly limited to low frequencies (below 20 Hz). Vehicle suspensions are usually designed to ensure that rigid body modes of a vehicle bogie and body occur at frequencies less than 10 Hz. In this

frequency range, the track behaves as relatively stiff and its effect on vehicles behavior is relatively small, especially in the vertical direction. The vehicle is thus usually modeled as a lumped-parameter system. In the 20-100 Hz frequency range, the coupled resonances of vehicle track system may be caused by long wavelength irregularities on the wheel, tire tread and in track support. In studies involving community noise, very high frequencies (up to 5000Hz) may be of concern. The elasticity of the wheels and wheel sets are thus taken into account using finite element methods. The analysis involving high frequency models thus include wheel-rail noise, wheel-rail impacts in the presence of wheel or rail defects, and structural integrity. In the relatively lower frequency range (<20 Hz), the dynamic behavior of railway vehicles is particularly important and vehicle can be modeled in a relatively simple manner, whereas at higher frequencies the track is more significant.

Frohling [5] developed and validated an 11 DOF mathematical model to predict track deterioration due to dynamic vehicle loading considering nonlinear and spatially varying track stiffness. Valesek [6] studied a three dimensional truck model for suspension control using SIMPACK. A number of other studies have also formulated three dimensional models of freight cars [7, 8, 9]. These studies have shown that lateral forces and motions are strongly coupled with car body roll. Railway cars are generally treated as if they were single vehicle, although they are coupled together. Masayuki and Hiroshi [10] proposed a new method, referred to as "Single car equivalency model" to analyze frequency response characteristics of intermediate cars in a long train under track irregularities. Using this method, the dynamic responses of intermediate cars could be derived in the presence of coupling with subsequent cars without increasing degrees of

freedom of the model. Multibody dynamics software has also been used for analyses of stability, ride quality, train-track interactions, etc [11, 12]. Some of these models employ a continuous track model to study transmission of vibration to nearby structures.

The vast majority of rail vehicle models employed in wheel- track interactions and ride dynamic analyses are in-plane models, either in the pitch or in the roll plane. The justification for using two dimensional pitch plane models is based on assumption of relatively small roll motions. This approach is widely used in road vehicles, while ride dynamic analyses of rail vehicles are somewhat similar to road vehicles with the exception of wheel-track interactions. Moreover, the wheelbase of majority of the ground vehicles is significantly larger than the track width. The vehicular roll motions can thus be considered negligible compared to magnitudes of vertical and pitch motions to realize a simplified pitch plane model [13]. These models can be used to study the ride dynamics and tire or wheel force responses subjected to road/track and self-excited vibration sources, such as wheel unbalance and tire non-uniformities. The dynamic interactions between the track and tire can be modeled using a variety of tire models reported in published studies [4].

Owing to the similarity of a pneumatic tire metro car with a road vehicle, the modeling techniques employed for road vehicles could be directly used. A wide range of two and three dimensional models of road vehicles have been developed. These models are applied for studies of pavement vehicle interactions and ride quality. Many vehicle models ranging from a linear quarter-vehicle model with two-degrees-of-freedom (DOF) to complex three-dimensional models with as many as 19-DOF have been reported in the literature [5, 7, 8]. While the majority of the models consider the sprung and unsprung

masses as rigid bodies, a few models have incorporated the flexibility of the trailer structure to study the contributions due to frame bending modes [14, 15,16]. Simple one- and two-DOF linear vehicle models have been used by several investigators to study the dynamic interaction of the heavy vehicle with the pavement [17, 2, 18]. Such models permit the analysis of different suspension concepts under uncoupled vertical motions in a highly convenient manner. These models, however, cannot be used to analyze the total dynamic interactions of road vehicles with the roads, which comprise various vibration modes associated with vertical, roll, and pitch motions of axles and sprung masses, nonlinearities due to friction, and influence of coupled suspension systems.

The contributions of frame bending to ride responses are generally considered small. The lumped-parameter models thus ignore the structural bending modes. Some of the recent works, however, have taken frame flexibility into account for ride models [19, 20]. Ibrahim et al. [19] investigated the ride behavior of a truck with a passive suspension system through analysis of a half vehicle model incorporating cab suspension, frame flexibility and cab structure flexibility. The analyses were conducted for both rigid body and flexible body models, and it was concluded that the frame flexibility strongly affects the driver vertical acceleration and cab pitch acceleration. The rms (root mean square) values of vertical and pitch accelerations were, respectively, 18 and 125% higher when a flexible bodies' model is considered. The flexibility in the truck model, however, yields several high frequency modes, which yields significantly higher rms values. The vibration associated with such modes may not be significant in view of human perception and comfort.

Stribersky et al. [20] investigated dynamics of new rail vehicle designs using virtual prototyping computer tools. The virtual vehicle was used for optimizing ride comfort of future metro trains. The overall system was modeled as a multibody system, taking into account the flexibility of the lightweight structures. The model results revealed different modes of model up to 20 Hz with dominant elastic deformations of the car body structure.

1.2.3 Component modeling

The validity of a vehicle model, whether in-plane or three-dimensional, rigid or flexible bodies strongly rely upon characterization of the components and their interconnections. A vast number of studies have focused on characterization of vehicle components, particularly, the tires and suspension components. Vehicle suspension systems often exhibit nonlinearities associated with Coulomb friction, progressive hardening nature of springs, and variable force-velocity properties of dampers due to bleed and blow-off hydraulic flows [18]. Majority of the analytical investigations, however, have been based on the assumption of linear suspension damping, while the influences of nonlinear and asymmetric suspension damping, on the dynamic behavior of the vehicle have been addressed only in a few studies [18].

The suspension springs are generally modeled as equivalent vertical springs, while rubber isolator is represented by parallel combination of a spring and a viscous dashpot using a Kelvin voigt model. This model generally yields over estimates of stiffness and damping properties at higher frequencies. Nonlinear models that incorporates both amplitude and frequency dependence of the isolator properties have also been proposed [22]. These include a spring in series with a dashpot, thus obtaining a

three parameter Maxwell model, which resulted in better higher frequency description of stiffness while the high frequency damping was underestimated. Better description of rubber characteristics can be obtained by using a summation of Maxwell models; these models, however, increase the complexity and number of parameters needed to accurately describe component or material properties. An alternative method to obtain good description of frequency dependence for viscoelastic material, while reducing the number of parameters is by using fractional derivatives. Koeller [23] discussed fractional derivative components which can replace ordinary dashpots in viscoelastic models. The analyses, however, tend to be quite complex when amplitude of excitation is unknown prior to calculations. Matsudaira [9] also considered shear stiffness of a vertical coil spring, which yields increasing coupling with lateral motions. The rubber isolators also yield flexibility in the shear mode, which is often ignored. A few studies have also considered radial flexibility of rubber isolators that also strengthen couplings between lateral, vertical and roll modes.

1.2.4 Tire models

Ride dynamic analysis of the vehicle traversing over varying road conditions and also subjected to self excited vibration generally demands for accurate modeling of the tire-terrain dynamical system. A wide range of tire models have been proposed for ride dynamic analyses and different tire models can yield considerably different results. The commonly used tire models, however, exhibit similar responses in the low frequency ranges, while the difference become apparent in the mid and high frequency ranges [4, 26]. Four types of tire models are widely used in road vehicles, namely point contact, rigid tread band, fixed footprint and adaptive footprint models [4, 26]. The linear and

nonlinear point contact tire model is most widely used for its simplicity of analyses, which represents a wheel by an equivalent vertical spring/damper assuming a single ground contact point directly beneath the wheel center [27]. The main advantage of the point contact model is that it is very simple to set-up for simulation purposes. The net foot-print force resulting from the vertical motion of a wheel relative to the terrain is assumed to act normal to the local terrain surface. A horizontal component of the net foot-print force can thus be generated whenever the local terrain profile is inclined to the horizontal, and is related to the vertical component through the tangent of the local profile angle. The "Rigid tread band model" is a modified point contact model, where the point follower is replaced by a roller follower having the wheel or tread band radius. Consequently, the terrain contact is not constrained to lie vertically beneath the wheel center, but is free to move fore and aft of the wheel center depending on the local terrain profile. The motion transmitted to the wheel center is thus different from the terrain profile due to the geometrical filtering effects of the rolling wheel. A "Fixed foot-print model" represents the wheel-terrain interaction through a foot print of fixed size. This model is represented as a parallel combination of various vertical springs and damping elements distributed uniformly over the fixed contact length, and has the ability to envelope the terrain irregularities through local deformations within the foot-print. . An "Adaptive foot-print model" of a tire is also considered, which are radially distributed spring and damping elements over the lower circumference of the wheel. Like the fixed foot-print model, this model has the ability to envelope terrain irregularities through local deflections.

Dhir and Sankar [4, 26] presented a comparison of the different lumped parameter tire models. It was concluded that the point contact and rigid tread band models consistently over-estimate the transmitted vertical tire forces, particularly in the 1-100 Hz frequency range. The fixed foot-print model under estimates the tire forces due to excessive enveloping of most irregularities. Moreover, a nonlinear point contact model yields more frequent wheel-hop. A point contact model, due to its simplicity, may thus be considered appropriate when wheel hop motions are not expected. An adaptive foot-print tire model showed a relatively closer agreement with the field-measured tire force spectra. Rigid tread band model could be effectively used when fore-aft forces are not concerned. Furthermore, a rigid tread band model is comparable to the adaptive foot print model.

1.2.5 Wheel non-uniformity modeling

Only a few studies have attempted to investigate the effects of wheel non-uniformity on the vehicle ride responses, although these are known to affect the vehicle ride in a highly adverse manner. Wheel non-uniformity can be defined as radial, tangential or lateral geometric variation of the tire or the rim. Among these three factors, it has been reported that the radial variation (or radial run-out) is the most significant source of vibration in the vehicle [28]. The radial run-out of a tire could cause increased vehicle vibration and large variation in the dynamic tire force. The unbalanced forces and moments due to wheel unbalance and non-uniformities can cause ride vibration in the frequency range to which human occupant is more sensitive.

A few models of varying complexity have been proposed to incorporate the tire-wheel non-uniformity. Stutts [30] has proposed a simple model of the effect of

concentrated radial stiffness non-uniformity in a passenger car tire. The model treats the tread band of the tire as a rigid ring supported on a viscoelastic foundation. The distributed radial stiffness is lumped into equivalent horizontal (fore-and-aft) and vertical stiffness coefficients. The concentrated radial stiffness non-uniformity is modeled by treating the tread band as fixed, with rotating stiffness non-uniformity at the nominal angular velocity of the wheel. This type of non-uniformity results in force transmission to the wheel spindle at twice the angular frequency of tire.

Bohler [31] investigated the generation of load spectra for the tractor chassis using multi body system package, SIMPACK, to account for the tire non circularity. The tire model based on Pacejka model [32] was used in the source code in conjunction with empirical relations. Demic [33] defined the limits of admissible peak-to-peak radial and lateral force variation, and peak-to-peak first harmonic radial and lateral force variations associated with non uniformity using a vehicle vibration model. It has been reported that the tire non-uniformity yields stronger influence on the ride dynamics of a vehicle at lower speeds since the suspension system can not fully isolate the lower frequency vibration [34, 35]. Kenny [36] analyzed six sources of wheel assembly vibration including, vehicle stud run-out, hub hole eccentricity, rim flange run-out, variations in tire run-out, variations in tire stiffness, and uneven tire weight distribution. It was reported that each run-out induces both restoring and unbalance forces. The total force due to each type of run-out was quantified as summation of radial force (product of the spring constant of the tire and the magnitude of the particular eccentricity) and the unbalance centrifugal force due to the particular run-out (product of mass of the tire-rim assembly, the magnitude of run-out, and square of the angular velocity of the tire). Ni

[37] proposed a mathematical model to account for radial and lateral run outs of the tire-wheel assembly. It has been reported that a tire mounted on an eccentric wheel is forced to be eccentric from the center and produces a new static unbalance.

Dorfi [38] analyzed role of the tire in generating non-uniformity induced dynamic force variations. The influences of mass, stiffness and geometric non-uniformities were investigated using both analytical and numerical approaches. The study considered four different types of non-uniformities. These included: (i) variations in radial and tangential sidewall stiffness; (ii) belt run-out, defined as the offset of the geometric centre of the belt with respect to centre of rotation, which also implies mass unbalance; (iii) variation in the Belt mass that is required to balance the run-out statically is retained; and (iv) tread gauge variation and belt run-out. Tread gauge variation is another component of tire non-uniformity that refers to relative height of tread blocks with respect to the belt surface. Tread gauge variations occur because of the extrusion thickness variations and rubber splices. Both belt run-out and tread gauge variations are geometric imperfections. Depending on the phasing of both imperfections, the total 'out-of-roundness' can increase and decrease. Dorfi [38] concluded that at higher speeds the first in plane resonance is excited by the belt run-out non-uniformity. The rolling radius variation drives the angular acceleration, which in turn gives rise to a longitudinal force in the footprint. This force dominates the tangential force response at high speeds. The rolling radius variation is strongly dependent on the belt radius variations and weakly dependent on the tread gauge variations. Figure 1.1 illustrates the combined effect of belt run-out and tread gauge variation.

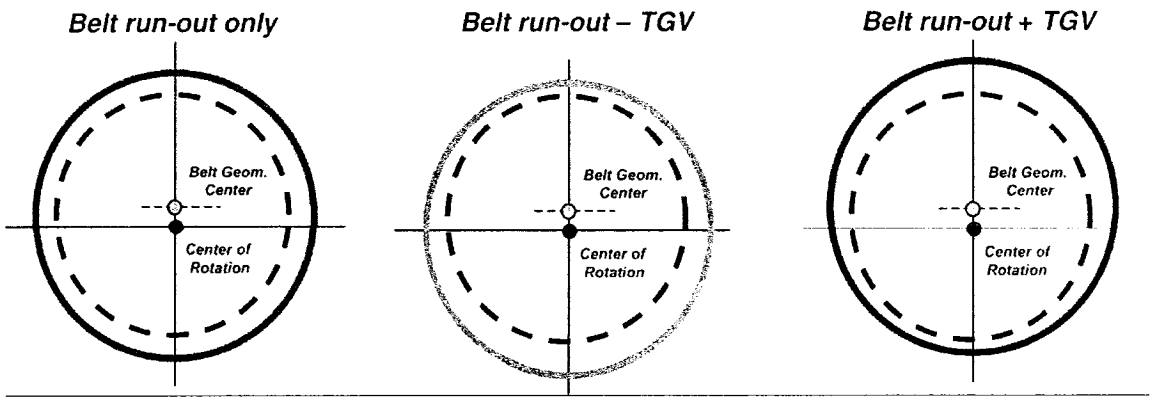

Figure 1.1: Conceptual diagram of geometric tire imperfections; Belt run-out and tread gauge variation (TGV) are shown.

In a Recent study, Deodhar [39] investigated the effects of wheel unbalance and wheel non-uniformity on the vehicle ride and dynamic tire force responses. The specific objectives included development of a comprehensive mathematical model of a commercial vehicle using a non-linear adaptive foot-print tire model, incorporating wheel unbalance and wheel non-uniformity and analysis of effects of wheel unbalance and wheel non-uniformity on the performance measures relevant to ride and dynamic tire forces. The wheel was assumed to have an elliptical shape with very small magnitude of radial run-out. The locus traced by the new wheel with radial run-out was obtained by expressing the radial difference through solution of equations of an ellipse and a circle. The radial difference was used to compute the wheel center height at each time instant, and thus the total force developed due to radial run-out of the wheel was found. This formulation implied that a radial run-out can be considered as an eccentricity, since it also yields an unbalance.

1.2.6 Track model

The railway track is often represented by a periodically supported continuous layer, and could include many layers representing sleeper support, ballast, sub-ballast,

sub-grade, etc. The track deformation mode, however, occur at relatively higher frequencies, well above the important ride frequencies. The road surfaces on the other hand are modeled as undeformable and randomly rough surfaces in most applications. The pneumatic-tired metro runs on tracks made of cemented blocks resting on concrete structure. Such tracks can thus be considered similar to an undeformable road surface. The roughness properties of metro track has been characterized in a recent study [63], which concluded that the track surface closely represent a very smooth road. For railway dynamics, when the curving behavior of rail vehicles is evaluated, the track profile and geometry are given special emphasis [40]. From the ride quality analysis point of view, track unevenness represents the main excitation function. The track descriptions thus include surface irregularities, consisting of either deterministic functions or stochastic functions. The track and road roughness models are usually expressed in terms of power spectral density (PSD) function of elevation. All of the track roughness models have been developed under a number of simplifying assumptions, which typically idealize the track profile as a stochastic process and exclude all the singular events. When vehicles have multiple axles, these track irregularities disturb the vehicles in a correlated fashion: the same input occurs at the following axle with a time delay as a function of vehicle speed and wheelbase. These correlations cause significant deviations from cases in which both deterministic and random inputs are assumed to be uncorrelated [41]. In cases where the unsprung masses of vehicles are modeled with damping, not only the irregularities at a displacement level but also at a velocity level must be considered.

1.2.7 Ride assessment methods.

Ride quality is concerned with driver's sensation of the terrain-induced vibration environment of a vehicle, and is generally difficult to assess. Numerous studies have been conducted to establish the ride assessment criteria for preservation of driver comfort, health, safety, and performance. These methods can be classified into four types as described by Wong [42].

1. Subjective Ride Measurements: The traditional method for comparing vehicle ride quality in the automobile industry is to compare vehicles driven over a given road section with a trained ride jury. With a large enough and well-designed evaluation scheme, this method could provide a meaningful comparison of the ride quality of different vehicles. However, this type of subjective evaluation cannot quantitatively determine the degree of difference in ride quality. Even though, it is still widely used by researchers to evaluate those human sensations that can not be quantified yet.

2. Shake Table Tests. In attempts to put more meaning and rigor into the study of human response to vibration by quantitative analysts, a great number of shake table experiments have been conducted over the years. Most of this research pertains to human response to sinusoidal vibration. It is intended to identify zones of comfort/discomfort for occupants in terms of vibration amplitude, velocity or acceleration in a given direction over a specific Frequency range.

3. Ride Simulator Tests. In these tests, computer controlled ride simulators are used to duplicate the vibration of a vehicle traveling over different road surfaces. In some studies, an actual vehicle body is mounted on hydraulic actuators, which reproduce vehicle motions in bounce, pitch, and roll. It is feasible to establish a human subjective tolerance limit in terms of vibration parameters.

4. Ride measurements in Vehicles. Shake table and ride simulator tests mentioned above are carried out under laboratory conditions. They provide only part of the vibration environment to which the passenger exposed to driving on the road. On-the-road ride measurements have become quite popular due to developments in data acquisition and analysis techniques in the recent years. This test method attempts to correlate the response of test subjects in qualitative terms such as "unpleasant", "intolerable" or "fatigue", or in physiological terms such as "blood pressure" or "heart rate" with objective vibration parameters measured at the test subject location.

Parsons et al. [43] investigated human comfort as affected by vibration. Vibration in six road vehicles was measured using accelerometers placed on the vehicle floor and under the buttocks of the test subjects. It was found that low frequency vibrations were amplified from the floor of the vehicle to the seat surface. The authors associated this with the natural frequency of the seat. It was also stated that the vertical direction was the axis which appeared as the predominant cause of discomfort. Goldman [44] analyzed the vibration data acquired from several sources, and deduced three comfort levels in the vertical mode in terms of acceleration and frequency contents. The comfort levels were referred to as *perceptible, unpleasant,* and *intolerable.* The vibration data used by Goldman were obtained from a variety of experiments where the subjective and physical environments varied considerably. Janeway [45] recommended exposure limits for vertical vibration of passenger cars in terms of maximum jerk in the frequency range of 0-6 Hz, and maximum acceleration for middle frequency range of 6-20 Hz. The safe limits of vibration exposure were proposed based on the survey of subjective tolerance

data, which represented an attempt to set a level at which no discomfort is experienced by the most sensitive passenger.

Over the years, numerous objective ride comfort criteria have been proposed, however, a generally acceptable criterion is yet to be established. The vast majority of these have associated vibration discomfort with the acceleration.

The ride performance of a vehicle is assessed in terms of magnitude and frequency contents of vibration transmitted to the driver's location. Human driver is known to be the most fatigue sensitive to vertical and horizontal vibrations in the 4-8 Hz and 1-2 Hz frequency range, respectively. The human sensitivity to rotational vibration is mostly in the 0.5-1.5 Hz frequency range [53]. The International Standard (ISO-2631/1, 1997) has outlined a procedure to assess the human exposure to whole-body ride vibrations in terms of overall frequency-weighted rms acceleration at the driver/passenger–seat interface. The standard defines frequency-weighting W_k for vertical vibration in the 0.5-80 Hz frequency range, and W_e for roll/pitch vibration in the 0.1-80 Hz frequency range. The frequency weighted accelerations are computed as per the band-limiting and weighting filters, defined in ISO-2631.

1.3 SCOPE OF PRESENT RESEARCH WORK

It is evident from the literature review that there is no literature available on ride vibration analysis of pneumatic tire metro cars. The metro cars used in Montreal can be considered as a combination of steel wheeled rail cars and pneumatic tired road vehicles. Furthermore, there are very few studies done to find the effect of vibration levels on the health of subway vehicle operators. Few studies which do exist related to ride analysis of metro cars, analyze effects of operational parameters only. It is thus very essential to

develop a comprehensive mathematical model which would be helpful in analyzing overall effect of different operational and design parameters on the ride environment of the pneumatic tired metro vehicle in regards to operator's health.

The overall objective of this thesis is to contribute towards enhancement of operator-friendliness of the metro car and thus to study the ride vibration responses of a pneumatic tired metro car to excitations arising from track roughness and wheel non-uniformity. The specific objectives include the following:

1. Develop a comprehensive three dimensional model of a metro car to study its vibration responses to track roughness and tire non-uniformity.
2. Develop a model for characterizing the rotating wheel tire non-uniformity and mass unbalance to incorporate them into the vehicle model.
3. Analyze the track surface roughness data and derive the excitation spectrum as a function of forward speed.
4. Perform analysis to derive the ride response to excitations.
5. Evaluate the test conditions and measured data and examine the validity of the model under selected test conditions.
6. Perform parametric sensitivity analysis to analyze effect of different operational and design parameters on performance measures.

2 MODELING OF PNEUMATIC TIRE VEHICLE-TRACK SYSTEM

2.1 INTRODUCTION

The vertical dynamic behavior of vehicle-track system at high speed is primarily dominated by pneumatic tire-track interactions and dynamic behaviors of the coupled vehicle components. The ride dynamic properties of vehicles, whether on road or on track, are thus investigated through analysis of the coupled vehicle dynamic system and vehicle-track interactions. Two or three dimensional ride dynamic models are generally used to study the contributions of different components of the vehicle to derive essential design guidance. For the pneumatic-tired guide vehicle, the ride dynamic analysis would involve study of interactions among various subsystems, namely, axle or wheelset, bogie, car body, suspension, tire and track. Such vehicles are known to cause considerable roll and vertical vibration [1]. A three dimensional model of the vehicle would thus be most appropriate for ride dynamic analyses. The degrees-of-freedom (DOF) of the model, however, should be adequately selected on the basis of known vibration behavior, so as to improve the computational efficiency. In this study, the longitudinal and the yaw modes of the vehicle components could be eliminated on the basis of experimentally observed vibration responses of the vehicle components. The lateral motion of the car body could also be neglected, since the magnitudes of lateral vibration were relatively small [1].

A number of simplifying assumptions are further made to reduce the complexity of the total vehicle and component models. The vehicle is assumed to travel on straight track and thereby the interactions of the guiding wheels with the side rails could be ignored. This is justifiable, since such interactions could occur only while curving and may not contribute greatly to the vertical dynamics of the vehicle. The axle, bogie and car

can be effectively represented by rigid bodies, assuming that the structural deflections occur at relatively high frequencies. Considering that the vehicle ride vibrations mostly dominate at lower frequencies (up to 20Hz); and that the human perception of vibration is most important only at lower frequencies, the structural deformation modes can be conveniently ignored. The vehicle is also assumed to move at a constant forward speed, thereby the traction and braking forces developed by the tires and associated inertial forces can be neglected. The interactions between the adjacent car bodies are expected to contribute mostly to longitudinal dynamics, particularly under braking and acceleration. Owing to the consideration of constant forward speed and relatively small magnitudes of longitudinal vibration, such interactions between the car bodies can be ignored. The tire interactions with the undeformable track are characterized by assuming a point contact of the tire with the track surface, while the tire is considered as a parallel combination of its linear stiffness and viscous damping properties. The car suspension and elastic wheelset mounts are also assumed to possess linear stiffness and damping properties.

In this chapter, the design of a pneumatic tired metro car is described and the essential components are identified for development of a three-dimensional lumped-parameter ride dynamic model. The model also incorporates tire non-uniformity and unbalance, which are known to yield important contribution to the overall vehicle response [2, 38, 39].

2.2 VEHICLE DESCRIPTION

A metro car primarily comprises four axles, two bogies and a car body, which are generally coupled through different elastic elements. Each bogie consists of two axles. Each axle is coupled to the bogie through four rubber mounts, two on each side as

illustrated in Figure 2.1. The car body is supported on two bogies (front and rear) through two elastomeric coil springs and a torsion bar to provide increased torsional stiffness, as shown in Figure 2.1. The Montreal metro employs two different models of metro cars, referred to as MR-63 and MR-73. The primary components of both the models are mostly identical, except for the drive and car body suspension design. The car body of the MR-73 is directly supported on coil springs, while that of MR-63 is supported on similar springs through an elastic spacer. The effective suspension rate of MR-63 car is thus lower.

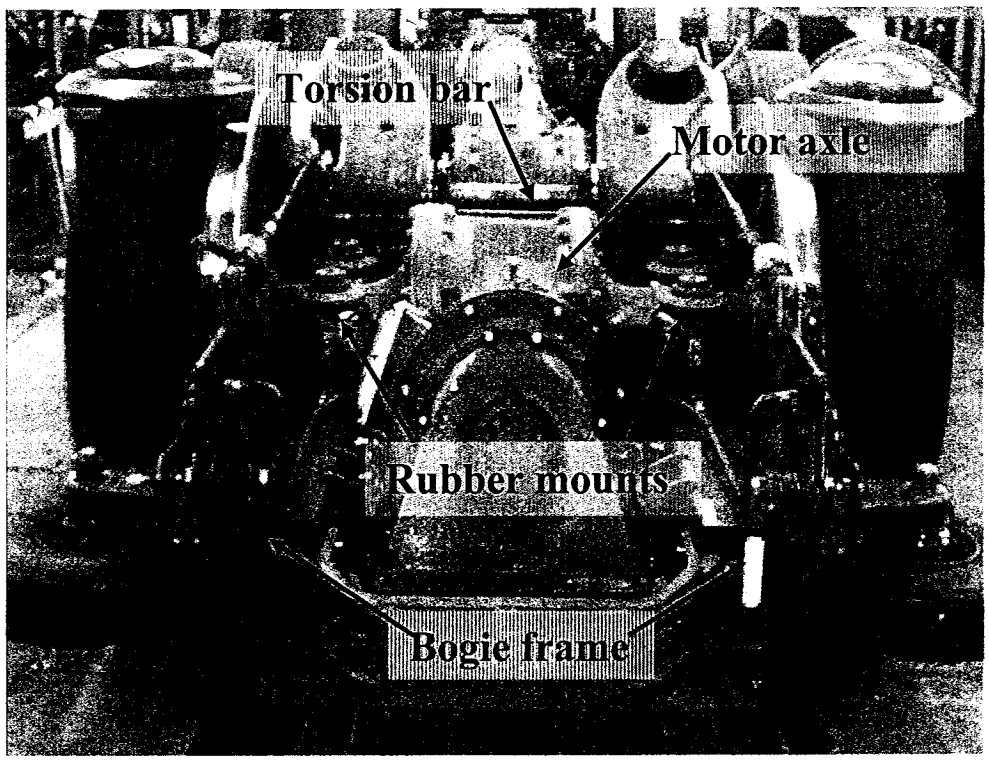

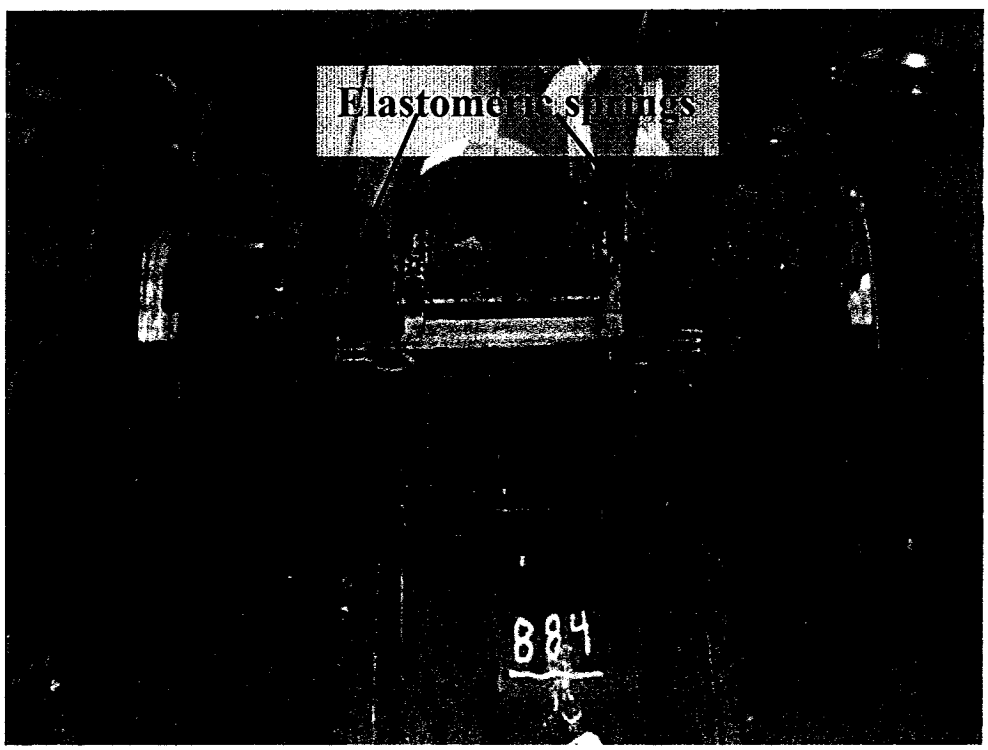

Figure 2.1: Pictorial views of an axle and bogie suspension elements.

2.3 VEHICLE SYSTEM MODEL

A wide range of vehicle models have been developed for ride dynamic analyses of road as well as track vehicles [5, 6, 7]. It is desirable to develop a simple but credible model, which could fully describe the dynamic system, with essential DOF that depend upon focus of the study. Increased complexity of model may often lead to difficulties in interpretations of system behavior, while the model credibility is determined by its capability to simulate the system behavior realistically within the desired accuracy. The measured ride vibration data of both types of cars were reviewed to identify important DOF for model development. A three-dimensional model with a total of 23-DOF was judged to be sufficient to describe the total ride dynamic behavior of the car. These included: 3-DOF for each of the four axles (vertical: z_{ai}, lateral: y_{ai} and roll: θ_{ai}; $i = 1,..,4$), 4-DOF for each of the two bogies (vertical: z_{bj}, lateral: y_{bj}, roll: θ_{bj} and pitch: ϕ_{bj}; $j = F, R$) and 3-DOF of the car body (vertical: z_c, roll: θ_c and pitch: ϕ_c).

Figure 2.2 shows pitch plane of the three-dimensional ride dynamic mathematical model. Inertial properties of the car body are represented by the lumped car body mass (m_c) and pitch mass moment of inertia (I_{cp}) about the mass center. The leading and the trailing bogies are designated as 'Bogie F' and 'Bogie R', respectively. Both the bogies are considered to possess identical mass (m_b) and pitch mass moment of inertia (I_{bp}). Car body is supported on these bogies through elastomeric springs which are modeled by parallel combination of linear stiffness (k_s) and viscous damping (c_s). The parameters l_1 and l_2 define the longitudinal distances of the front and rear elastomeric springs, respectively, from the car body c.g., while e_F and e_R are the longitudinal locations of the

springs with respect to c.g. of the respective bogies. Each bogie is supported on two axles through 8 rubber mounts and 4 motor mounts, as illustrated in Fig. 2.1. The locations of these mounts are schematically illustrated in the plan view of a bogie in Fig.2.3. The rubber mounts are modeled similar to elastomeric springs by parallel combinations of linear stiffness (k_r) and viscous damping coefficient (c_r), while the motor mounts are represented by stiffness (k_m) and damping coefficient (c_m), as shown in Fig. 2.2. The radial elasticity of each axle rubber mount is also considered and represented by its lateral stiffness (k_r') and damping coefficient (c_r'), as shown in Fig. 2.4. The lateral flexibility of the motor mount is neglected due to its considerably lower compression stiffness compared to rubber mounts. The masses due to axle, motor, tires and wheels are lumped together and represented by the unsprung mass (m_a) of each axle assembly. Suspension properties of each tire are represented by parallel combination of a linear stiffness (k_t) and viscous damping (c_t). The lateral compliance and damping properties of the tires are also considered by a linear spring (k_t') and a damping coefficient (c_t'), as illustrated in the roll plane of the model in Fig. 2.4.

Figure 2.4 presents the roll plane of the three dimensional ride dynamic model. The roll mass moments of inertia due to car body, bogie and axle assembly are represented by I_{cr}, I_{br} and I_{ar}, respectively. The anti-roll torsion bar coupling the metro car and the bogie is represented by a linear rotational stiffness (k_θ) and rotational damping coefficient (c_θ). The lateral spacings between the left and right elastomeric springs with respect to the car body c.g. are represented by a_{lj} and $a_{rf}(j = F, R)$, respectively. Notations d_{li} and d_{ri}, similarly, define lateral spacing of the left and right motor mounts of

axle i, respectively, while c_{li} and c_{ri} define those of rubber mounts. The distance b_{li} and b_{ri} define the lateral spacing of the left and right tires of axle i, respectively. The parameters h_t, h_1 and h define the distances between the rubber mount and bogie c.g., rubber mounts and axle c.g. and axle c.g. and the track datum, respectively.

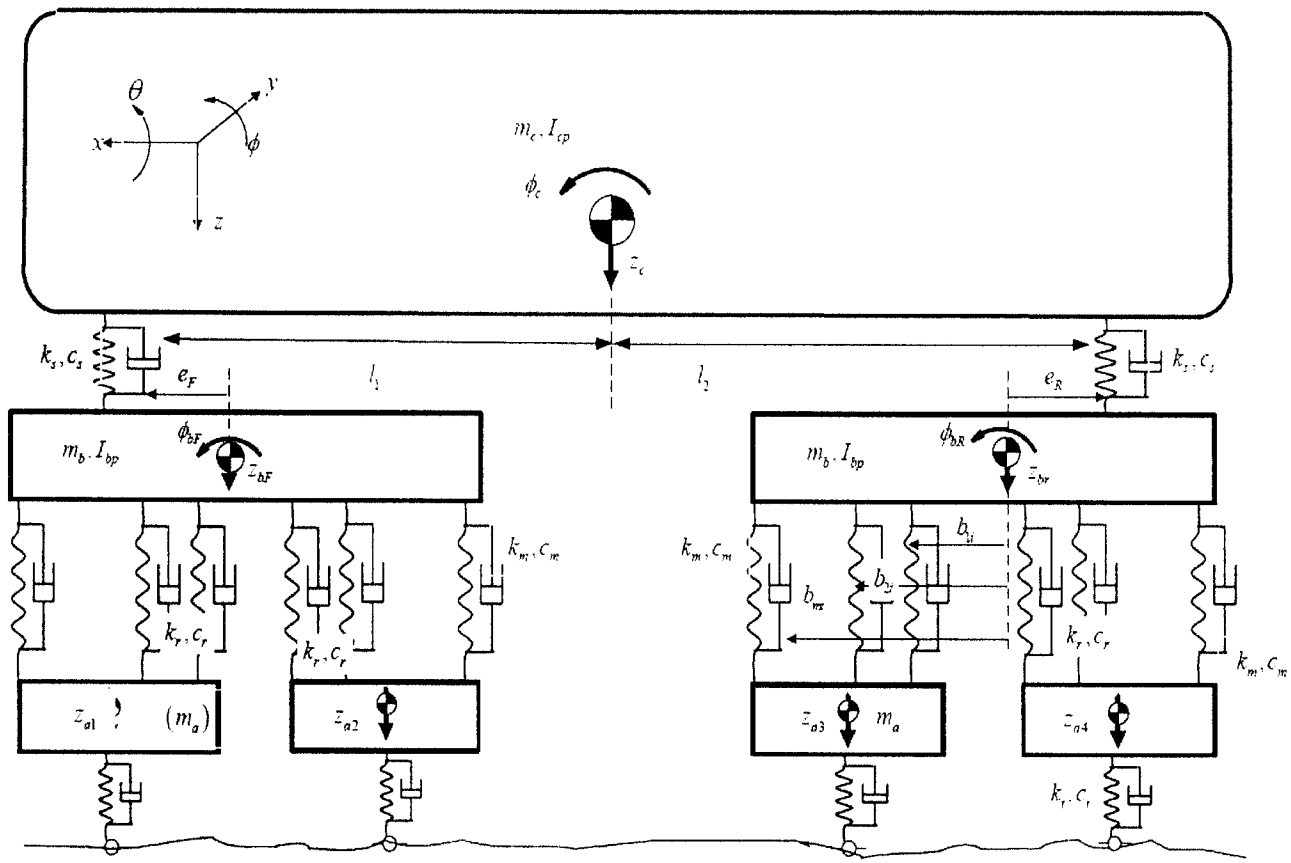

Figure 2.2: Pitch plane of the three dimensional ride dynamic model of the metro car.

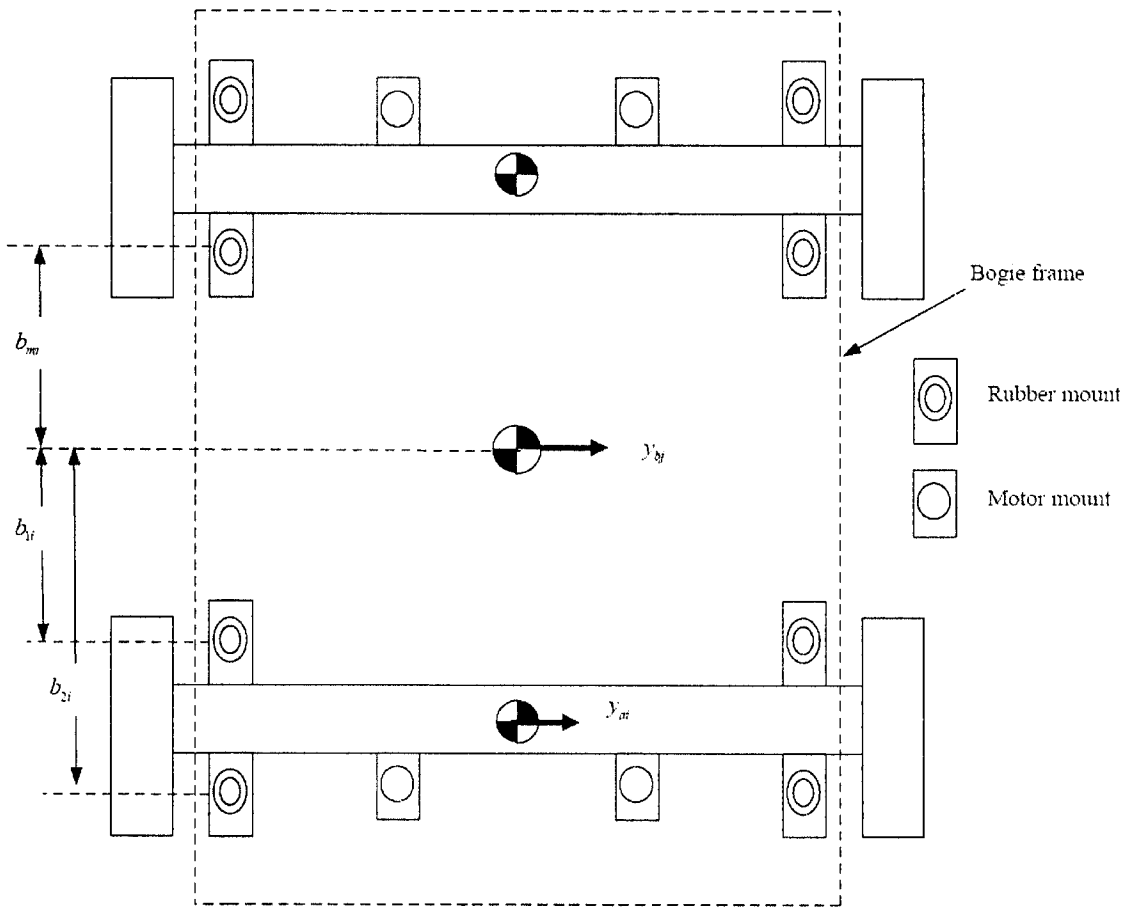

Figure 2.3: Plan view of a bogie-axle assembly.

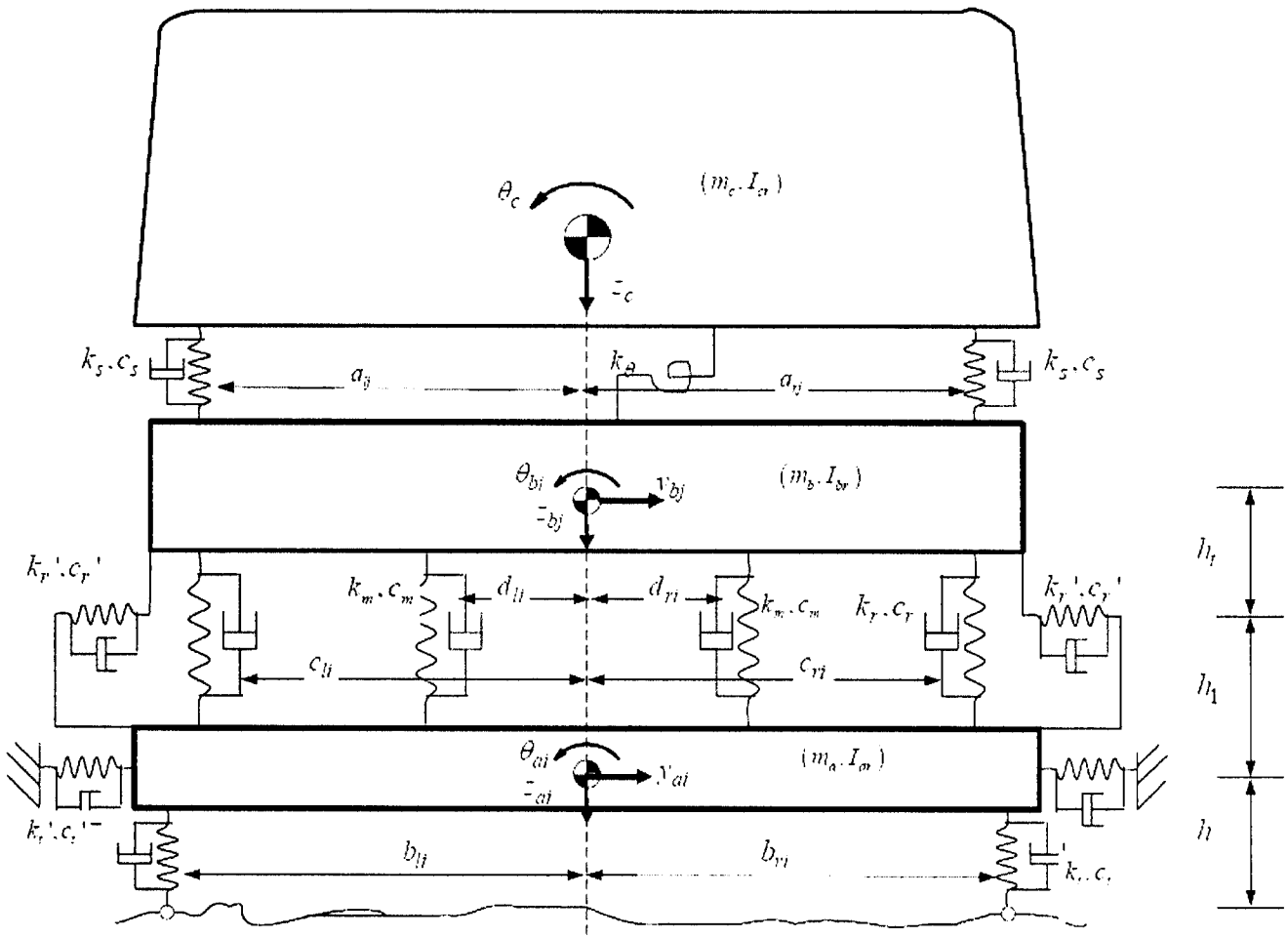

Figure 2.4: Roll plane of the three dimensional ride dynamic model of the metro car.

2.3.1 Equations of motion

Equations of motion are derived using the principle of force equilibrium. The system of coordinates, recommended by Society of Automotive Engineers, is used, as shown in Fig. 2.2. In the equation of motion, the axle 1 and axle 2 ($i=1,2$) are coupled to the leading bogie ($j=F$), while axle 3 and axle 4 ($i=3,4$) are coupled with the trailing bogie ($j=R$). The equations of motion of the 23-DOF three dimensional ride dynamic model of the metro car are summarized below:

Vertical motion of the axle $(z_{ai}; i=1,..,4)$

$$m_a\ddot{z}_{ai}+(F_{ir}^{l}+F_{il}^{l})+\sum_{k=1}^{4}F_{ik}^{r}+(F_{ir}^{m}+F_{il}^{m})=(F_{il}^{u}+F_{ir}^{u})+(F_{il}^{n}+F_{ir}^{n}) \tag{2.1}$$

Lateral motion of the axle $(y_{ai}; i=1,..,4)$

$$m_a\ddot{y}_{ai}+\sum_{k=1}^{4}N_{ik}+(F_{ir}^{t'}+F_{il}^{t'})=0 \tag{2.2}$$

Roll motion of the axle $(\theta_{ai}; i=1,..,4)$

$$\begin{aligned} &I_{ar}\ddot{\theta}_{ai}+(F_{il}^{t}b_{li}-F_{ir}^{t}b_{ri})+[(F_{i3}^{r}+F_{i4}^{r})c_{li}-(F_{i1}^{r}+F_{i2}^{r})c_{ri}]+(F_{il}^{t'}+F_{ir}^{t'})h \\ &(F_{il}^{m}d_{li}-F_{ir}^{m}d_{ri})-h_1\sum_{k=1}^{4}N_{ik}=\left(F_{il}^{u}+F_{il}^{n}\right)b_{li}-\left(F_{ir}^{u}+F_{ir}^{n}\right)b_{ri} \end{aligned} \tag{2.3}$$

Vertical motion of the bogie $(z_{bj}; j=F,R)$

$$m_b\ddot{z}_{bj}-\sum_{i=m1}^{m2}\sum_{k=1}^{4}F_{ik}^{r}+\sum_{p=l}^{r}F_{jp}^{s}-\sum_{i=m1}^{m2}\sum_{p=l}^{r}F_{ip}^{m}=0 \quad ; m1=1 \text{ and } m2=2 \text{ ; for } j=F$$

$$m1=3 \text{ and } m2=4 \text{ ; for } j=R \tag{2.4}$$

Lateral motion of the bogie ($y_{bj}; j = F, R$)

$$m_b \ddot{y}_{bj} - \sum_{i=m1}^{m2} \sum_{k=1}^{4} N_{ik} = 0 \tag{2.5}$$

Roll motion of the bogie ($\theta_{bj}; j = F, R$)

$$\begin{aligned} & I_{b_r} \ddot{\theta}_{bj} + \sum_{i=m1}^{m2} \left[\left(F_{i1}^r + F_{i2}^r \right) c_{ri} - \left(F_{i3}^r + F_{i4}^r \right) c_{li} \right] - h_t * \sum_{i=m1}^{m2} \sum_{k=1}^{4} N_{ik} \\ & + \sum_{i=m1}^{m2} \left[F_{ir}^m d_{ri} - F_{il}^m d_{li} \right] + F_{jl}^s a_{lj} - F_{jr}^s a_{rj} + M_j^t = 0 \end{aligned} \tag{2.6}$$

Pitch motion of the bogies (ϕ_{bF} *and* ϕ_{bR})

$$\begin{aligned} & I_{bp} \ddot{\phi}_{bF} + \left(F_{24}{}^r + F_{21}{}^r \right) * b_{12} - \left(F_{14}{}^r + F_{11}{}^r \right) * b_{11} + \left(F_{23}{}^r + F_{22}{}^r \right) * b_{22} - \left(F_{13}{}^r + F_{12}{}^r \right) * b_{21} \\ & + \left(F_{2r}^m + F_{2l}^m \right) b_{m2} + \left(F_{Fl}^s + F_{Fr}^s \right) * e_1 - \left(F_{1r}^m + F_{1l}^m \right) * b_{m1} = 0 \\ & I_{bp} \ddot{\phi}_{bR} + \left(F_{44}{}^r + F_{41}{}^r \right) * b_{14} - \left(F_{34}{}^r + F_{31}{}^r \right) * b_{13} + \left(F_{43}{}^r + F_{42}{}^r \right) * b_{24} - \left(F_{33}{}^r + F_{32}{}^r \right) * b_{23} \\ & + \left(F_{4r}^m + F_{4l}^m \right) b_{m4} + \left(F_{Rl}^s + F_{Rr}^s \right) * e_2 - \left(F_{3r}^m + F_{3l}^m \right) * b_{m3} = 0 \end{aligned} \tag{2.7}$$

Vertical motion of the car body (z_c)

$$m_c \ddot{z}_1 - \sum_{j=F}^{R} \sum_{p=l}^{r} F_{jp}^s = 0 \tag{2.8}$$

Roll motion of the car body (θ_c)

$$I_{cr} \ddot{\theta}_c + \sum_{j=F}^{R} [(F_{jr}^s * a_{rj} - F_{jl}^s * a_{lj}) - M_j^t] = 0 \tag{2.9}$$

Pitch motion of the car body (ϕ_c)

$$I_{c_p} \ddot{\phi}_c + \sum_{p=l}^{r} F_{Rp}^s * l_2 - \sum_{p=l}^{r} F_{Fp}^s * l_1 = 0 \tag{2.10}$$

In the above equations F_{ir}^t and F_{il}^t are the forces developed by the right and left tires, respectively, of an axle i, given by.

$$F_{ir}^{t} = k_t\left(z_{ai} - z_r - b_{ri}\theta_{ai}\right) + c_t\left(\dot{z}_{ai} - \dot{z}_r - b_{ri}\dot{\theta}_{ai}\right)$$
$$F_{il}^{t} = k_t\left(z_{ai} - z_l + b_{li}\theta_{ai}\right) + c_t\left(\dot{z}_{ai} - \dot{z}_l + b_{li}\dot{\theta}_{ai}\right) \qquad ;i = 1,..,4 \tag{2.11}$$

$F_{ir}^{t'}$ and $F_{il}^{t'}$ are the lateral tire forces developed by right and left tires, given by:

$$F_{ir}^{t'} = F_{il}^{t'} = k_t'\left(y_{ai} + h\theta_{ai}\right) + c_t'\left(\dot{y}_{ai} + h\dot{\theta}_{ai}\right) \tag{2.12}$$

Each rubber mount imposes a vertical force $F_{ik}^{r},\left(k = 1,..,4\right)$ on axle i and the corresponding bogie. The force attributed to compression/extension of each mount is evaluated as a function of its deformation δ_{ik}^{r} and rate of deformation $\dot{\delta}_{ik}^{r}$, such that:

$$F_{ik}^{r} = k_r\delta_{ik}^{r} + c_r\dot{\delta}_{ik}^{r} \tag{2.13}$$

where $\begin{Bmatrix}\delta_{i1}^{r}\\ \delta_{i2}^{r}\\ \delta_{i3}^{r}\\ \delta_{i4}^{r}\end{Bmatrix} = \begin{bmatrix}1 & -c_{ri} & -1 & c_{ri} & -b_{1i}\\ 1 & -c_{ri} & -1 & c_{ri} & -b_{2i}\\ 1 & c_{li} & -1 & -c_{li} & -b_{2i}\\ 1 & c_{li} & -1 & -c_{li} & -b_{1i}\end{bmatrix}\begin{Bmatrix}z_{ai}\\ \theta_{ai}\\ z_{bj}\\ \theta_{bj}\\ \phi_{bj}\end{Bmatrix}$

The vertical forces due to left and right motor mounts acting on axle i and the corresponding bogie, $F_{ip}^{m}\left(p = l,r\right)$ are derived from linear motor mount properties and their deformation in compression/extension :

$$F_{ip}^{m} = k_m\delta_{ip}^{m} + c_m\dot{\delta}_{ip}^{m} \tag{2.14}$$

where $\begin{Bmatrix}\delta_{il}^{m}\\ \delta_{ir}^{m}\end{Bmatrix} = \begin{bmatrix}1 & d_{li} & -1 & -d_{li} & -b_{mi}\\ 1 & -d_{ri} & -1 & d_{ri} & -b_{mi}\end{bmatrix}\begin{Bmatrix}z_{ai}\\ \theta_{ai}\\ z_{bj}\\ \theta_{bj}\\ \phi_{bj}\end{Bmatrix}$

The elastic mounts are also assumed to generate lateral forces N_{ik}, due to their flexibility in shear as a function of shear deformation $\delta_{ik}^{r'}$, such that:

$$N_{ik} = k_r'\delta_{ik}^{r'} + c_r'\dot{\delta}_{ik}^{r'} \quad :i = 1,..,4 \text{ and } k = 1,..,4 \tag{2.15}$$

where $\delta_{ik}^{r'} = y_{ai} - h_1\theta_{ai} - (y_{bj} + h_t\theta_{bj})$

The suspension forces F_{jp}^{s} developed by the secondary suspension (elastomeric springs) as a function of its deformation δ_{jp}^{s} and rate of deformation $\dot{\delta}_{jp}^{s}$:

$$F_{jp}^{s} = k_s\delta_{jp}^{s} + c_s\dot{\delta}_{jp}^{s}: \qquad j = F, R; \qquad p = l, r \tag{2.16}$$

where $\begin{Bmatrix} \delta_{jl}^{s} \\ \delta_{jr}^{s} \end{Bmatrix} = \begin{bmatrix} 1 & a_{lj} & e_j & -1 & -a_{lj} & -l_j \\ 1 & -a_{rj} & e_j & -1 & a_{rj} & -l_j \end{bmatrix} \begin{Bmatrix} z_{bj} \\ \theta_{bj} \\ \phi_{bj} \\ z_c \\ \theta_c \\ \phi_c \end{Bmatrix}$

The roll moments M_j^t developed due to torsional deflection δ_j^t of the torsion bars are derived assuming linear rotational stiffness (k_θ) and damping coefficient (c_θ):

$$M_j^t = k_\theta\delta_j^t + c_t\dot{\delta}_j^t \tag{2.17}$$

where $\delta_j^t = \left[\left(a_{lj} + a_{rj}\right)\left(\theta_{bj} - \theta_c\right)\right] / l_t$

Apart from the inertial and mount/suspension forces acting on an axle, the tires may impose additional forces due to tread non-uniformity and/or unbalance [39]. The metro car tires generally exhibit considerable non-uniformity and unbalance, as in case of other vehicle tires. The ride dynamic model of the metro car was formulated to incorporate forces due to tire-wheel assembly non-uniformity (F_{ip}^{n}) and unbalance (F_{ip}^{u}), as evident in Eqns. (2.1) and (2.3). These forces are derived in the following section.

2.4 EXCITATION

The ride dynamic response of a metro car strongly depends upon interactions of the tire with the surface of the undeformable track, non-uniformity and unbalance of tire-

wheel assembly. The wheel unbalance and non-uniformity would cause predominant ride response at a frequency corresponding to the angular speed of the wheel. The analyses are thus performed under excitations arising from track roughness, wheel unbalance and tire OOR.

2.4.1 Track roughness

From the ride quality analysis point of view, track unevenness represents the primary source of excitation. The track surface roughness models are usually expressed in terms of power spectral density (PSD) of track profile elevation. All of the track roughness models have been developed under substantial assumptions, which typically idealize the track profile as a stochastic process and exclude all the singular events [62]. The track irregularities are generally considered to cause displacement inputs at the wheel-track interfaces. For vehicles with multiple axles, the track irregularities disturb the vehicles in a correlated fashion i.e. the same input occurs at the adjacent axles with a time delay as a function of vehicle speed and wheelbase. Strong correlation may thus exist between forces applied by different axles within the same bogie, and the adjacent bogie. For faster vehicle speeds and for vibration propagation at low frequencies, the correlation may extend over a greater distance. These correlations cause significant deviations from cases in which both deterministic and random inputs are assumed to be uncorrelated [41,62].

In a recent study, measurements of elevations of the Montreal metro track surface were carried out [63]. The measurements were reported by elevation, Δz, of surface points with longitudinal spacing (Δx) of 0.3 m. Roughness values were recorded for both left and right track for a total distance of 160.2m. The study reported different roughness

properties for right and left tracks, as in the case of roads and rails, which would excite the vehicle in roll.

Let z_l^i and z_r^i denote the displacement inputs at left and right tires of axle i due to track surface roughness. The tires of an adjacent axle will also encounter identical displacement inputs with a time delay. The time delay between excitations at axles j and k, $t_{jk} = L_{jk}/v$, is related to distance L_{jk} between axles j and k, and forward speed v. This delay can also be expressed in the frequency domain by $e^{-i2\pi f t_{jk}}$ [62]. The differential vertical displacement excitation of an axle tire on the left and right track can also be modeled as a randomly distributed roll excitation. A roll excitation model is developed considering a randomly generated roll angle, such that:

$$\phi = 2\varphi(rand - 0.5). \tag{2.18}$$

where φ is a constant that relates to maximum value of expected roll angle, and *rand* is the Gaussian random number.

The measured elevation data were acquired and analyzed to derive the spatial displacement spectral density using Fast Fourier Transform (FFT). For this purpose, the measured data were interpolated for a longitudinal spacing (Δx) of 0.13 m. the number of FFT points ($NFFT$) used to determine the spatial PSD were 1024. Therefore, the sampling rate could be determined as:

$$f_s = 1/\Delta x = 1/0.13m = 7.683 \text{ (cyc/m)}. \tag{2.19}$$

The frequency resolution (Δf) could also be determined using the relation:

$$\Delta f = f_s / NFFT = 7.683/1024 = 0.0075 \text{ (cyc/m)} \tag{2.20}$$

Figure 2.4(a) illustrates the spatial PSD of surface profile of the left track. The PSD spectrum is also compared with those of a smooth highway and smooth runway reported in published data [64,65]. The comparisons suggest that displacement excitation due to the track roughness lies in between those of a smooth runway and a smooth highway. Furthermore, the low spectral components of the elevations of the track tend to be very low compared to the smooth road and runway.

The track surface roughness can also be expressed in terms of temporal spectral density. The spatial PSD ($S(n)$) and wavelength (n) are related to the temporal PSD ($S(f)$) and frequency (f), in the following manner.

$$S(f) = S(n)/v \text{; and } f = v \times n \tag{2.21}$$

Considering that the metro cars generally operate at or near a constant speed of 60 km/hr, the temporal PSD of the surface roughness is derived for this speed and shown in Fig. 2.4(b). The figure also compares the temporal PSD properties of the track with those of the smooth road and runway.

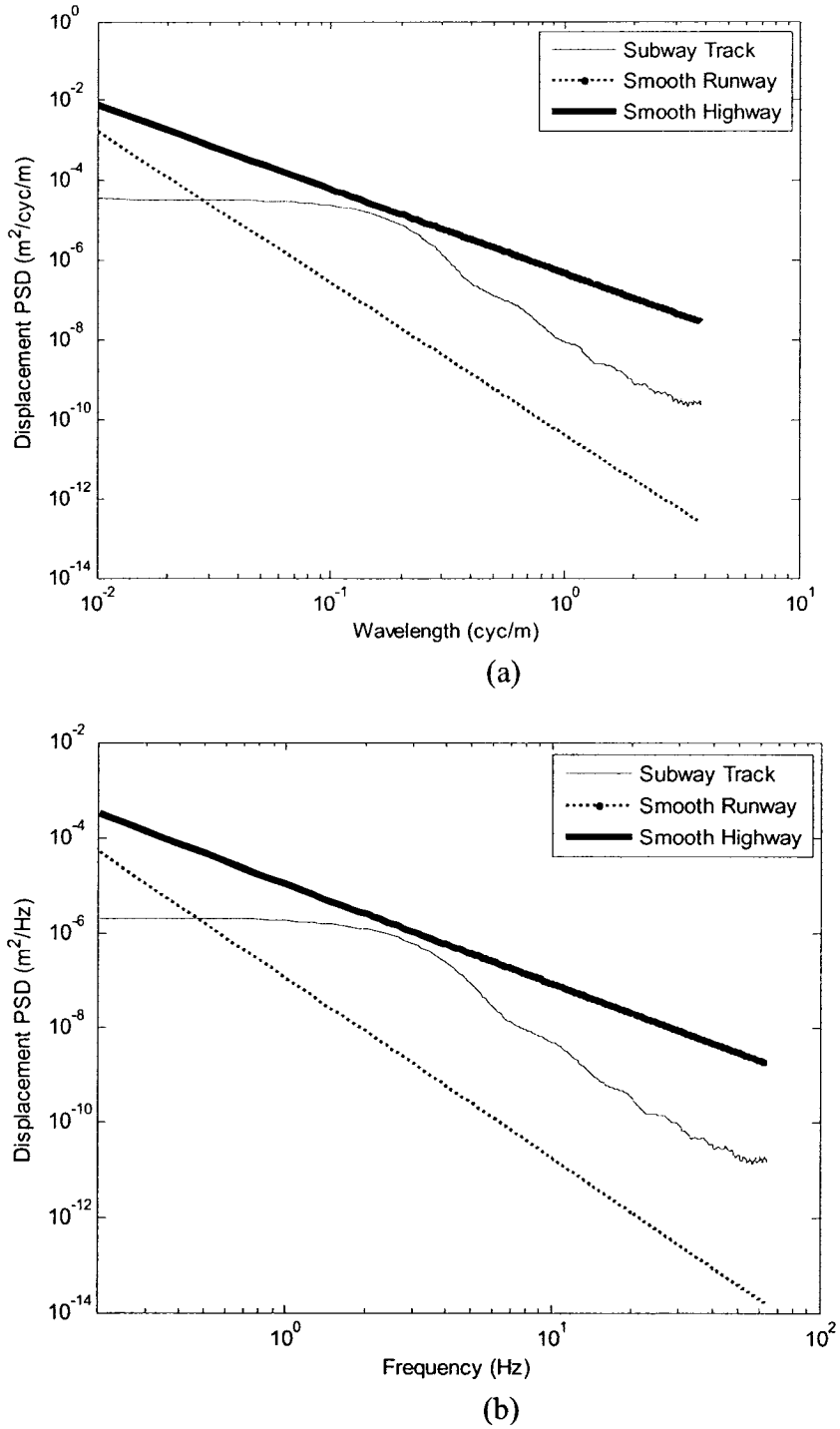

Figure 2.5: Comparison of spectral density of the track roughness with those of a smooth runway and smooth highway: (a) spatial PSD; and (b) temporal PSD at $v = 60$ km/hr.

2.4.2 Modeling of mass-unbalance

The vehicle wheel assemblies generally exhibit mass unbalance that may be caused by unequal mass distributions and/or wheel defects [28, 29]. The tires may also exhibit out-of-roundness (OOR) due to non-uniformity of the tread [39]. In this study, the wheel non-uniformity is expressed by an equivalent mass unbalance together with geometric non-uniformity of the tread profile. The magnitudes of wheel OOR were measured by Societe de transport de Montreal (STM) during an earlier study [1]. The measurements were performed in all the 8 tires of MR-63 and MR-73 cars using a dial gage. The measurements revealed OOR values in the 0-3.302 mm range, which describes the deviations in radius of the unloaded tire. The mass unbalance of the wheel yields a centrifugal force, F_{ip}^{u}, given by:

$$F_{ip}^{u} = me_i^p \omega^2 \sin(\omega t - \phi_i); \quad i = 1,..,4 \text{ and } p = l, r \tag{2.22}$$

where m is half the mass of an axle assembly, e_i^p is eccentricity, ϕ_i defines phase angle specifying position of peak OOR of a tire on the i^{th} axle with respect to that of the first axle, $\omega = \frac{v}{r}$ is the angular frequency and r is the effective wheel radius.

The equivalent mass eccentricity due to an OOR defect was determined using an approximate geometric representation of the OOR, as shown in Fig. 2.8, which is described in the subsequent sub-section. The mass center of the approximated geometry was then estimated from AUTOCAD, assuming uniform mass distribution. The equivalent eccentricity was computed as the deviation between the axle shaft center and the estimated mass center. Table 2.1 illustrates the equivalent eccentricity due to different magnitudes of OOR. Fig. 2.6 illustrates the relationship between the magnitudes of tire

OOR and the corresponding equivalent eccentricity. The nonlinear relationship between e_i^p and OOR magnitudes is determined by fitting a polynomial function to the experimental data, given by:

$$e_i^p = 0.0088(OOR)^2 + 0.0281(OOR) - 0.0064 \tag{2.23}$$

Table 2.1: Equivalent eccentricity due to different values of tire out-of-roundness (OOR).

Out of roundness (mm)	Eccentricity (mm)
6.25E-01	1.50E-02
8.75E-01	2.48E-02
1.00E+00	3.03E-02
1.25E+00	4.22E-02
1.50E+00	5.54E-02
1.75E+00	6.98E-02
2.00E+00	8.52E-02
2.25E+00	1.02E-01
2.50E+00	1.19E-01
2.75E+00	1.37E-01

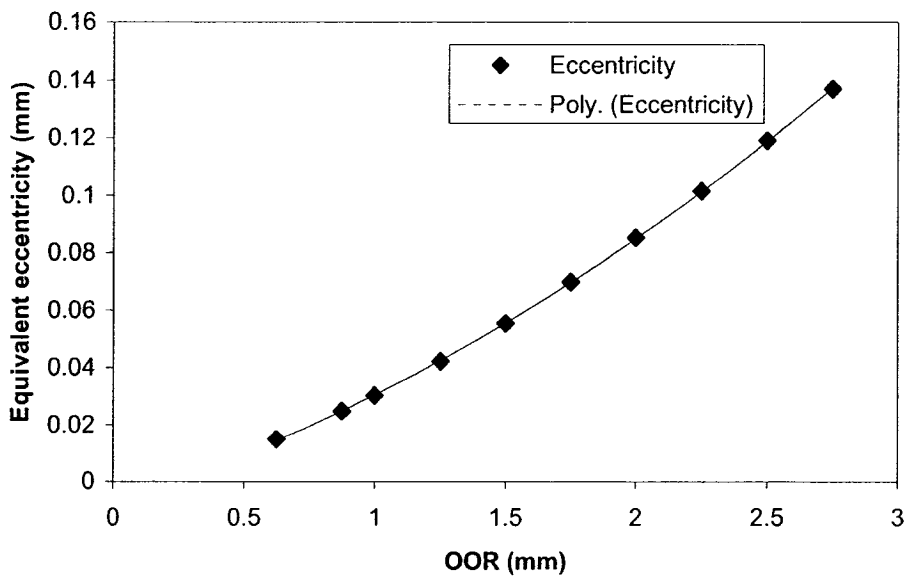

Figure 2.6: Relationship between equivalent eccentricity and OOR magnitude.

2.4.3 Modeling of tire out-of-roundness

Figure 2.7, as an example, illustrates the measured OOR values of different tires of a MR-73 metro car. The locations of OOR are indicated in the figure, while the magnitudes are shown in 1000^{th} of an inch. The figure shows presence of multiple irregularities in the tread profile. There are different models which could be employed for characterizing tire non-uniformity, as discussed in literature review [30, 37, 38]. In this study the OOR magnitude is characterized by the peak radial run out, where only largest OOR value is considered [39]. An asymmetric tread profile is subsequently generated through superposition of a semi-circle with a semi-ellipse, as shown in Fig. 2.8. The radius of the tire is taken as the semi-minor axis of the ellipse, while the semi-major axis is the sum of tire radius and peak OOR value. The radius of the circle b is same as semi-minor axis of the ellipse and $a = b + (\Delta r)_{max}$, where $(\Delta r)_{max}$ is the magnitude of OOR.

Defining r' as the radius of the elliptical portion of the tire profile, the coordinates of a point on the tire periphery can be expressed as a function of polar coordinate θ', as:

$$\begin{aligned} x &= r'\cos\theta' \\ z &= r'\sin\theta' \end{aligned} \tag{2.24}$$

The radius of the non-uniform tread profile can be related to semi-minor and semi-major axis values as:

$$r' = \sqrt{\frac{a^2 b^2}{b^2\cos^2\theta' + a^2\sin^2\theta'}} \tag{2.25}$$

An uniform wheel forms a circle of radius r ($r = b$), the OOR may be expressed by radial difference between the elliptical and a circular form, such that:

$$(\Delta r) = r' - r = \sqrt{\frac{a^2 b^2}{b^2\cos^2\theta' + a^2\sin^2\theta'}} - b \tag{2.26}$$

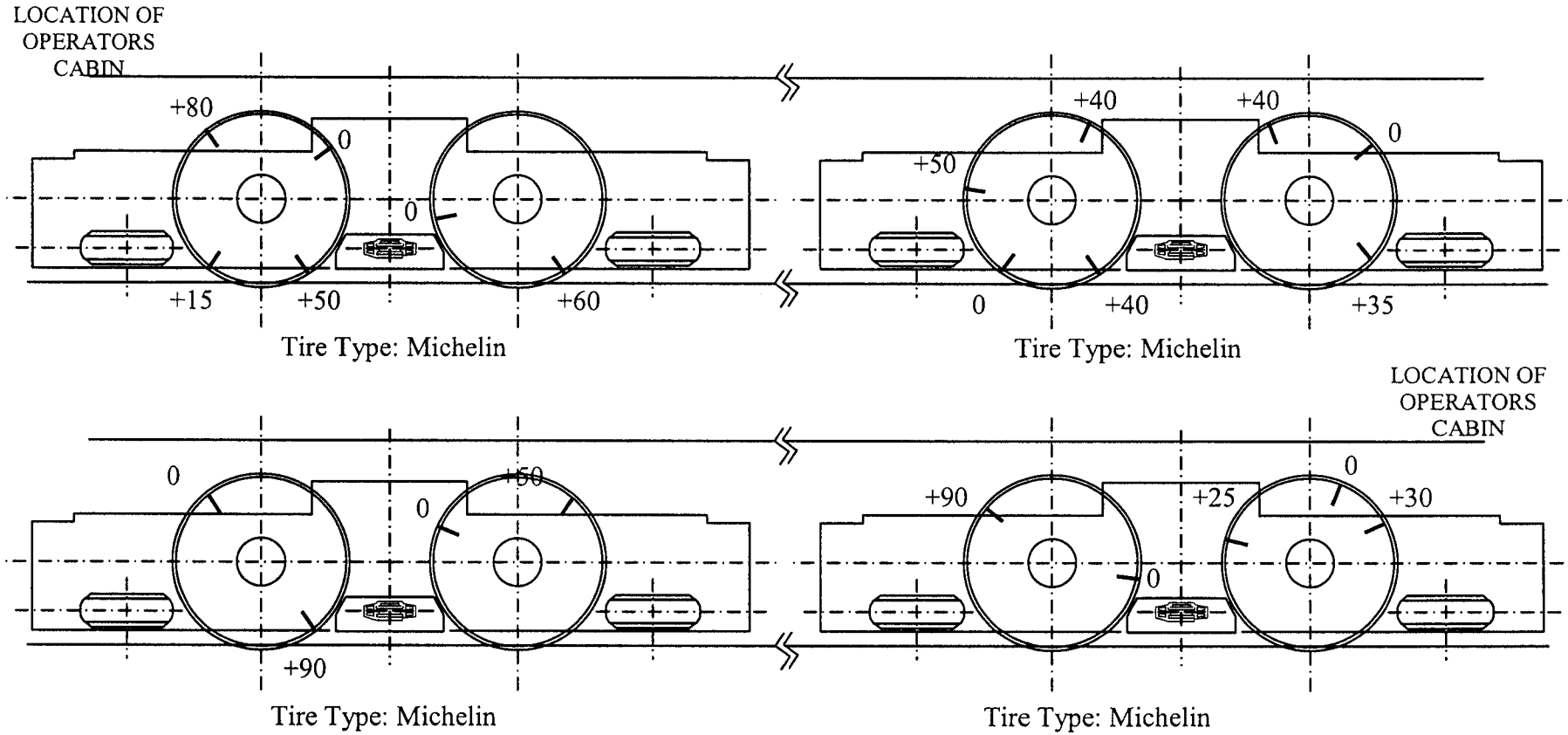

Figure 2.7: Measured OOR values of tires on a test car test car MR-73-1A (values in thousandths of an inch).

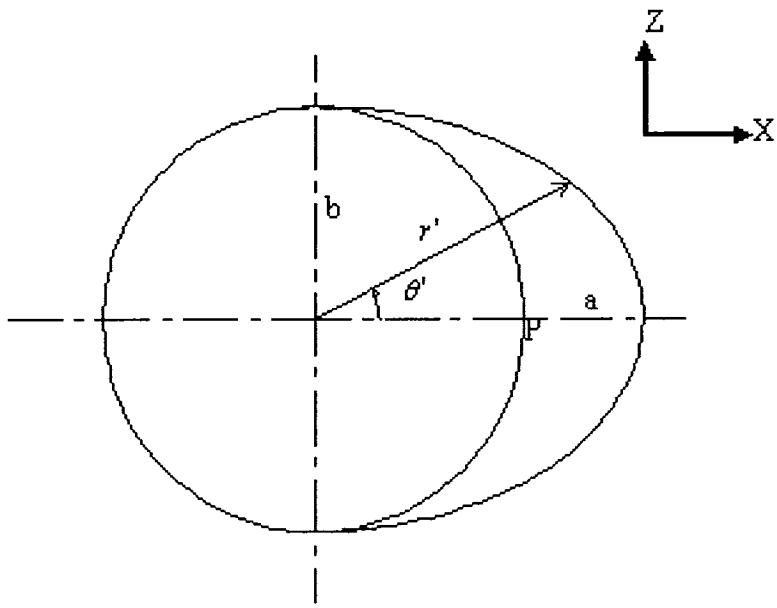

Figure 2.8: Representation of wheel out-of-roundness.

Figure 2.9 illustrates the variation in radial run out as a function of θ'. The results were derived by considering $b = r = 0.45m$, $a = 0.45275m$ and $\theta' = (0, 2\pi)$. From the variations it is apparent that the magnitude of OOR is simply the maximum radial deviation, $(\Delta r)_{\max} = a - b$. The variations in the radial run out cause an additional tire force, F_{ip}^{n}, transmitted to the axle assembly. This force is derived assuming linear stiffness and damping properties of tires as:

$$F_{ip}^{n} = k_t \Delta r_i^p + c_t \Delta \dot{r}_i^p; \quad i = 1,..,4 \text{ and } p = l, r \tag{2.27}$$

where Δr_i^p is the radius variation of the tire p in axle i.

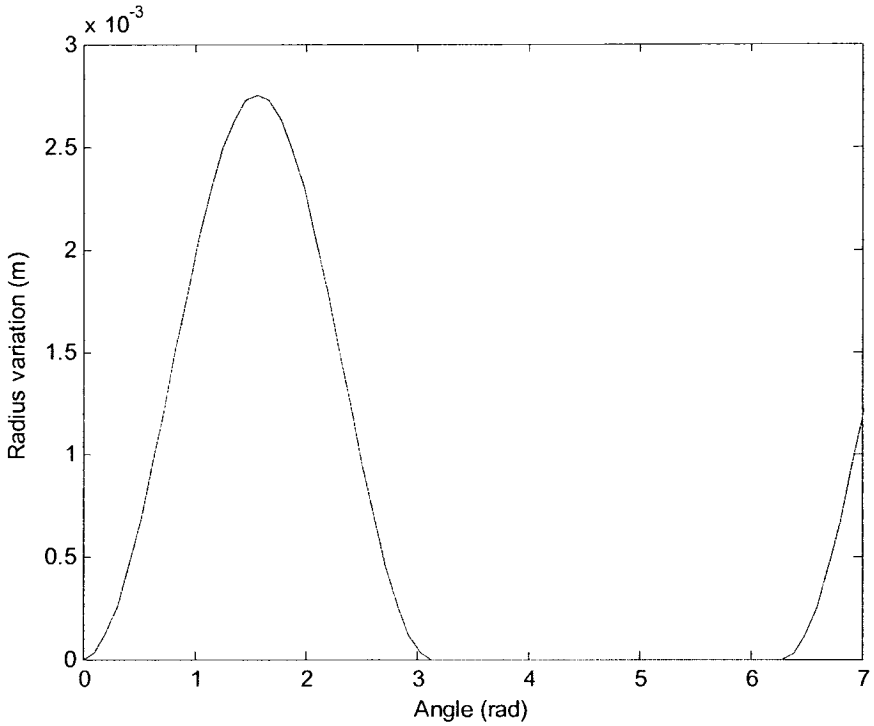

Figure 2.9: The locus of radial difference for one revolution about point 'P'

2.5 SUMMARY

In this chapter, a three dimensional ride dynamic mathematical model of the Montreal metro car is developed to study its ride dynamic performance. Characterization of excitation forces due to random track profile, mass unbalance and non-uniformity of tire-wheel assembly is performed. These excitation forces are then input into the mathematical model of the vehicle. After the formulation of the mathematical model of the metro car, attempts are to be made to validate the ride dynamic mathematical model with the experimental data. In the subsequent chapter, attempts are being made to recognize target responses which would be further utilized for validating the mathematical model.

3 FIELD MEASURED RESPONSES

3.1 INTRODUCTION

The ride dynamic response of a vehicle can be effectively assessed through measurement of vibration during field operation. A carefully designed experiment could provide considerable insight into the role of various design and operating conditions on the ride response. Furthermore, the measured data could be applied to verify the validity of physical system model, which could subsequently serve as a vital design tool. The ride vibration responses of different metro cars were measured in a recent study by CONCAVE and IRSST [1]. The primary objectives of the study were to assess the vibration exposure of metro operators and to evaluate the contributions due to various operating factors.

In this dissertation, the experimental data acquired by the above study are further evaluated to enhance an understanding of the role of various design and operating factors, and to examine the validity of the proposed model. The experimental conditions employed in the study are briefly summarized and a set of vehicle component responses are selected, termed as target responses, which would be utilized for the validation purpose of the mathematical model developed in chapter 2.

3.2 MEASUREMENT OF RIDE VIBRATION AND DATA ANALYSES

The experiments involved four different configurations of MR-63 and MR-73 metro cars, which represented variations in the state of tires, passenger load, speed, and the mechanical conditions of the components. These four configurations of test cars are summarized below:

- Configuration 1A: A recently maintained car with new tires.
- Configuration 1B: A recently maintained car with 1/3 reduced tread tires (80 000 km).
- Configuration 2A: A car due for maintenance with existing tires (tread condition-unknown).
- Configuration 2B: Maintenance due with 1/3 reduced tread tires (80 000 km).

The influence of variations in the passengers load on the transmitted vibration was also studied by performing measurements during the rush and off-rush hours. Furthermore measurements were performed along the two directions of a specific line in order to study the role of direction of travel. The cars used in both the models had identical passenger capacity of 160 passengers.

Each test car was instrumented to measure car body vibration along all the six axes, including three translational and rotational axes, using a Crossbow DMU™ (Dynamic Measurement Unit), capable of measuring accelerations along the three translational directions, and velocities along the three rotational directions. The DMU was installed on the car body floor in the passenger compartment along the central longitudinal axis, directly behind the metro operator, as illustrated in Figure 3.1. A DMU was installed on one of the bogies to measure its ride responses along the translational and rotational axes.

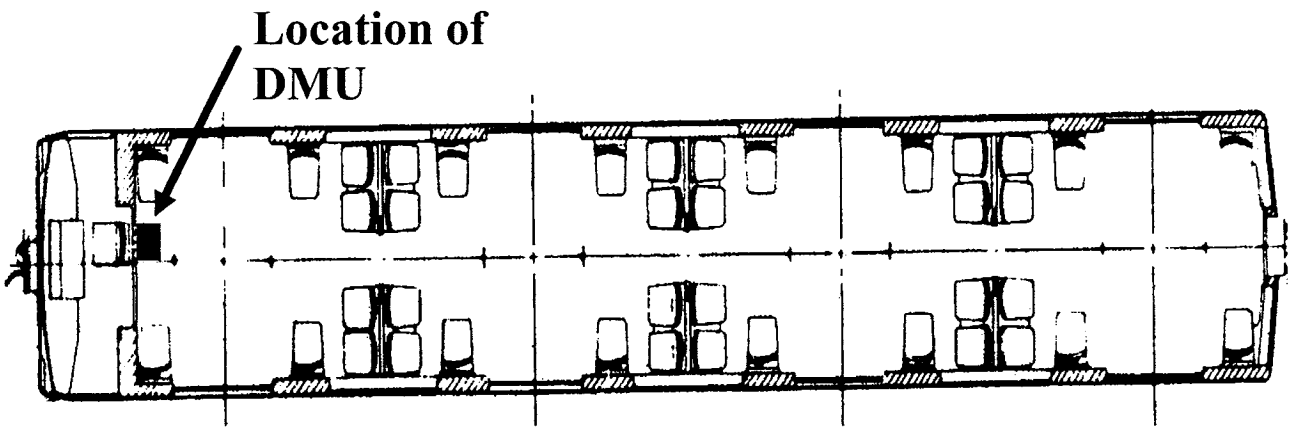

Figure 3.1: The location of the DMU on the metro car floor (Not to scale).

The vertical motion of one of the axle was also measured through installation of a single axis accelerometer on the axle. This accelerometer was installed on the left side of the first axle located close to the operator cabin. A two-axes accelerometer, oriented along the lateral and vertical axes, was installed on the right-side of the axle to measure vertical as well as lateral accelerations of the axle. The measured vertical accelerations at the left and right sides of the axles were manipulated to obtain the roll acceleration response of the axle.

The data acquired for the test cars operating on different lines during the rush and off-rush hour operations were analyzed to derive the spectra of vibration transmitted to the car, bogie and the axle. The resulting spectra were thoroughly examined to study the effects of speed, passenger load, direction of travel and state of tires and maintenance on the ride responses.

3.3 SUMMARY OF FINDINGS

The analyses of the measured data revealed the following for the MR-73 cars:

- The sprung mass acceleration spectra revealed peak magnitudes near 1, 2.4 and 2.9 Hz corresponding to roll, bounce and pitch modes of the sprung mass, respectively.
- Significant magnitudes of roll and vertical vibration of the car were observed near 6 Hz, particularly for the car with non-uniform tires. The peak increases considerably with speed, and was attributed to angular speed of the non-uniform tire.
- The vertical acceleration PSD response of the bogie revealed peak magnitudes near 2.4, 4.5, 6, 12 and 18 Hz. These peaks are believed to be associated with vertical mode of the car, pitch mode of the bogie, vertical mode of the bogie, and vertical and roll modes of the axle, respectively. The magnitudes of roll acceleration peaks of the bogie are relatively higher than those of car.
- The magnitudes of lateral acceleration are quite small; however, they occur at low frequencies, which could yield appreciable lateral displacement of the car body.
- The pitch acceleration response of the car body was observed to be relatively small. The bogies, however, revealed considerable pitch vibration, which may be partly attributed to the torsion bar suspension and partly to the distribution of load. The results show considerable magnitudes of pitch vibration in the 4-5 Hz range. These frequencies were believed to be associated with the pitch mode oscillations of the bogie and the torsion bar suspension.

- The spectra of vibration transmitted along the longitudinal and yaw axes were observed to be significantly small.
- The comparison between vertical and roll vibration responses of the carbody for different load conditions suggest insignificant effect of passenger load, which is most likely attributed to the progressive hardening property of the suspension.

3.4 TARGET RESPONSE

From the experimental results, it can be concluded that ride vibration responses of a metro car are most importantly influenced by wheel non-uniformity, speed and load. The measured data, however, could not provide information related to the properties of various components, such as primary and secondary suspensions, inertial properties and properties of the mounts and tires. The influences of these design parameters can be effectively investigated from analysis of the model described in chapter 2. The model, however, must be capable of predicting important contributions due to wheel non-uniformity. Moreover, the validity of the model should be demonstrated to gain confidence in the results and possible design tunings. For this purpose, the spectra of measured vibration were evaluated to identify mean target vibration spectra. The target spectra are subsequently used to examine the model validity. Owing to relatively low magnitudes of longitudinal, lateral and yaw accelerations, the target spectra are established for: car body bounce, pitch and roll; bogie bounce, pitch and roll; and axle bounce and roll accelerations.

The mean or target spectra were derived upon combining the spectra of vibration measured on different segments under varying conditions. The result attained for different segments of metro lines revealed that the vibration behavior of the cars, with a

few exceptions, could be generally considered independent of the segments, while the state of tires and maintenance could affect the magnitudes of vibration responses. The data attained under different operating conditions, were grouped together to identify the mean vibration responses. These mean spectra would be considered most representative as they are derived from grouping of the data attained for cars with different tires (new, existing, and 1/3 tread reduced), different maintenance condition (recently maintained and due for maintenance), and operating at different speeds on different segments of the line. The vast majority of the data, however, was acquired at a relatively higher speed, since the cars accelerate very rapidly.

Figure 3.2 illustrates the mean values of vertical acceleration PSD responses of the car, bogie and axle of the MR-73 test cars. The results suggest that the bogie undergoes largest magnitudes of vertical vibration. The magnitudes of vibration transmitted to the car are considerably smaller, specifically at frequencies above 3 Hz, suggesting the effectiveness of the bogie suspension in the vertical mode. The spectra of vertical vibration show peaks for all three components in the 2-2.5 Hz range, suggesting that this would correspond with the vertical resonance of the system. The results also show peak response of the car in the vicinity of 6 Hz, which was attributed to the vertical mode of the bogie. The bogie and axle acceleration spectra also revealed peaks near 4.5 Hz (bogie pitch mode), and 10-12 Hz range and near 18 Hz (axle vertical and roll modes).

The mean values of roll acceleration spectra of the car, bogie and axle are presented in Figure 3.3. The results show extremely small magnitudes of roll vibration of the car, when compared to those of the bogie and the axle. The bogie and the axle tend to

be rigidly coupled in the 10-12 Hz range, associated with the vertical mode of the axle. The response spectra of the axle shows significant peak near its roll mode of 18 Hz.

The mean values of the corresponding pitch acceleration spectra are illustrated in Figure 3.4. Pitch spectra were noted for car and bogie only. As evident from the figure, pitch magnitudes are quite high for the bogie, when compared with those of the car. Spectral components at 4-5 Hz, 6 Hz and in the range of 18-20 Hz are predominant. These components can be associated with bogie pitch, bogie vertical axle roll modes.

The mean values of the corresponding lateral acceleration spectra are also illustrated in Figure 3.5. It should be noted that the magnitudes of lateral vibration of the car body are quite small. The car body lateral acceleration response reveals spectral components of lateral vibration near 1.2 Hz, 2.4 Hz, 6 Hz, 10-12 Hz and 18 Hz, likely associated with car roll, car vertical, bogie vertical, axle vertical and axle roll modes, respectively.

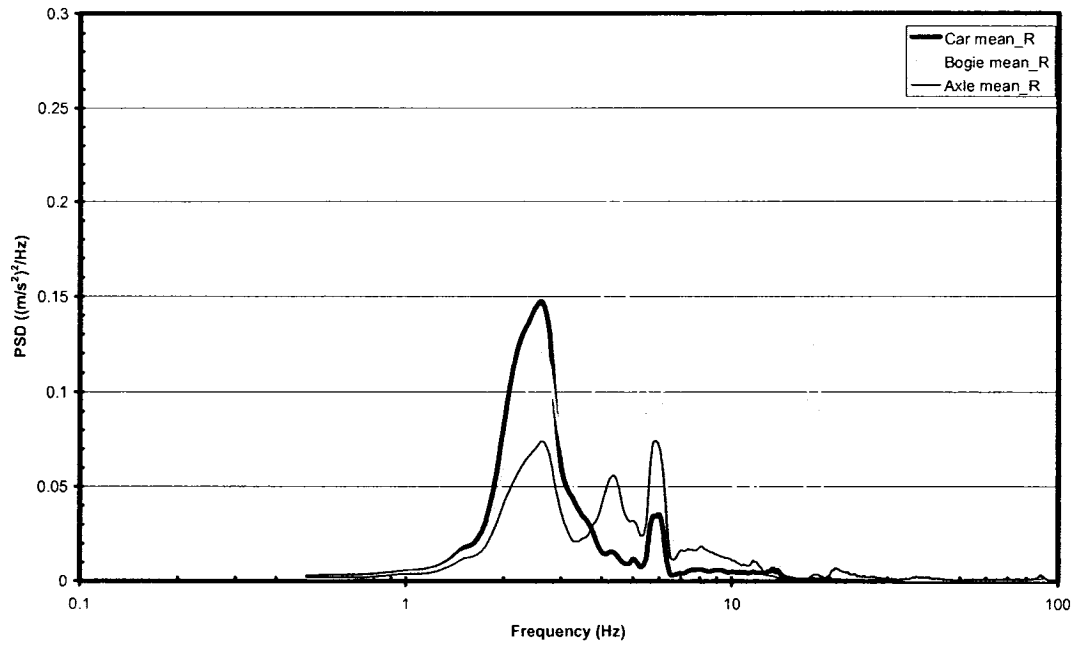

Figure 3.2: Mean vertical acceleration PSD spectra of the car, bogie and axle.

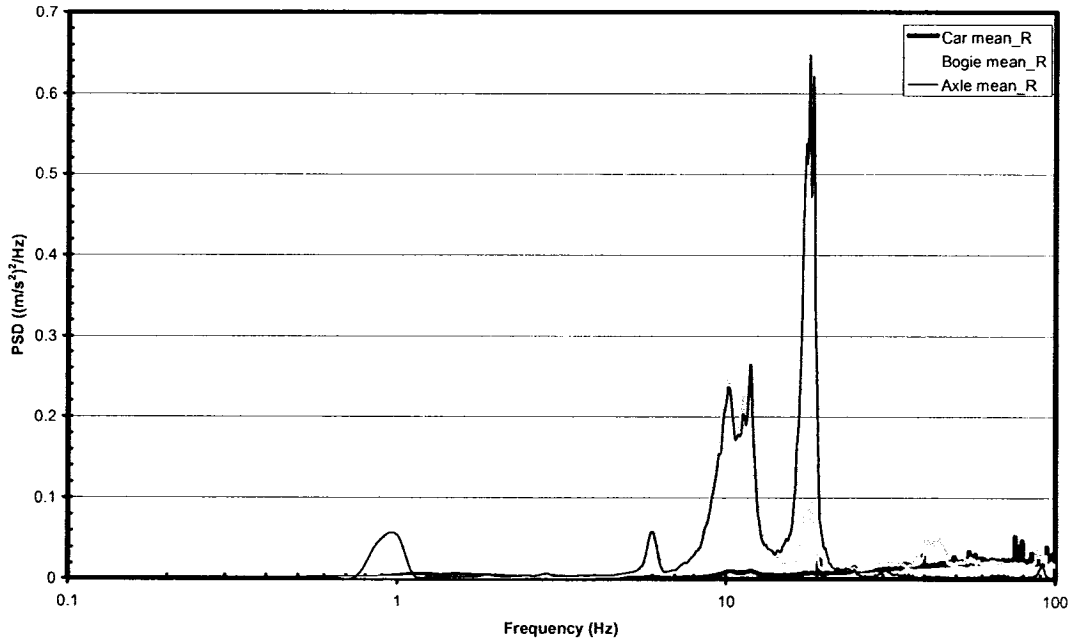

Figure 3.3: Mean roll acceleration PSD spectra of the car, bogie and axle.

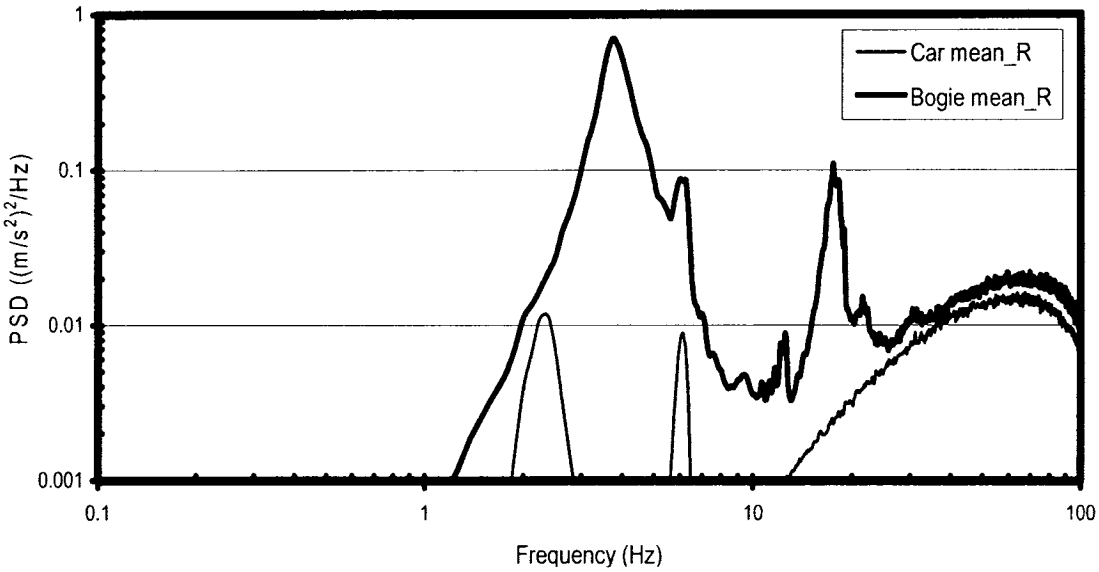

Figure 3.4: Mean pitch acceleration PSD spectra of the car and bogie.

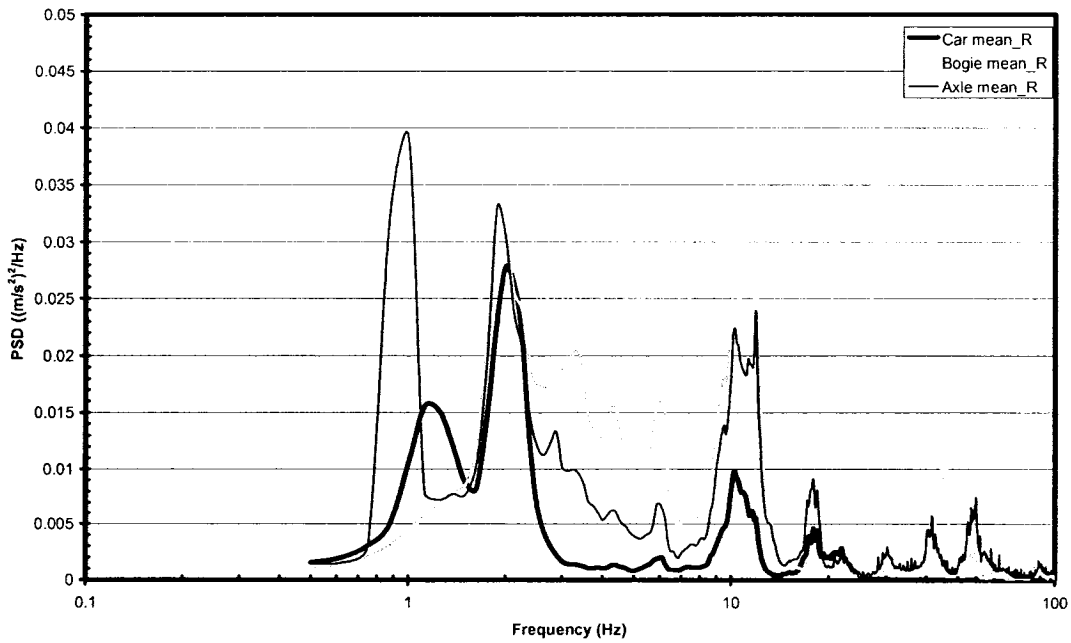

Figure 3.5: Mean lateral acceleration PSD spectra of the car, bogie and axle.

3.5 SUMMARY

In this chapter, attempts were made to summarize the findings, which resulted from the experiments conducted on Montreal metro by CONCAVE and IRSST. A brief description of experiment methodology is presented to have a better understanding of the data acquisition and analysis. The primary purpose was to identify target responses which could further be utilized for the validation of the ride dynamic mathematical model developed in chapter 2. In chapter 4, free and forced vibration analysis of the ride dynamic mathematical model of the metro car is performed for obtaining the acceleration responses of the vehicle components. Furthermore, attempts are made to validate the model with the experimental responses identified in this chapter.

4 VALIDATION OF THREE DIMENSIONAL VEHICLE MODEL

4.1 INTRODUCTION

The ride performance of a vehicle, whether on road or tracks, directly relates to frequency contents and intensity of transmitted vibration. Human body exhibits relatively larger perception of whole body vibration in the 4-10 Hz frequency range along the vertical axis and in the 1-2 Hz range along the horizontal axis [53]. Various studies on measurements and analyses of human responses to vibration have also shown greater sensitivity of the body to vibration in these frequency ranges. These include the studies on apparent mass and vibration power absorption of the vibration-exposed body and on the nature of vibration transmitted to various body segments [66, 67].

The assessment of vehicle ride comfort thus necessitates appropriate consideration of predominant frequencies of transmitted vibration, which are generally the resonant frequencies of the vehicle system or the excitation frequencies, together with the magnitudes of transmitted vibration. An effective ride dynamic model of a vehicle is thus expected to yield good estimates of vehicle resonant frequencies and magnitudes of transmitted vibration. Both these measures strongly rely upon characterization of vehicle components, and external excitations. An analytical model, however, may involve numerous simplifying assumptions that may compromise the prediction abilities of the model. The validity of the model, therefore, needs to be established using either field or laboratory measured response. In this chapter, proposed ride dynamic model of the metro car is analyzed to examine its validity on the basis of the measured responses presented in chapter 3. The inertial and geometric properties of the subway vehicle are identified from the data supplied by STM. The measured data on wheel non-uniformity are further used

to define equivalent excitations in terms of mass unbalance and geometric non-uniformity.

The model validation is carried out in two stages. In the first stage, free vibration analysis of the model is initially performed and the natural frequencies and deflection modes are compared with predominant frequencies of measured vibration. In the second stage, the ride responses to random track roughness and deterministic wheel non-uniformity excitations are derived along the selected axis of vibration and compared with the measured responses presented in chapter 3. The model validity and limitations are subsequently discussed.

4.2 FREE VIBRATION ANALYSIS

The human sensation of vibration-induced discomfort is strongly related to predominant frequencies of transmitted vibration and the mode of vibration. A preliminary assessment of ride performance of a vehicle may thus be obtained from the free vibration behavior of the vehicle system. The natural frequencies and deflection modes yield further essential information on the dynamic behavior of the vehicle-track system components and structure. The linear differential equations of motion of the 23-DOF vehicle model are expressed in the matrix form as:

$$[M]\{\ddot{q}\}+[C]\{\dot{q}\}+[K]\{q\}=[K_F]\{q_o\}+[C_F]\{\dot{q}_o\} \tag{4.1}$$

Where $[M],[C]$ and $[K]$ are (23×23) mass, damping and stiffness matrices, respectively. $[K_F]$ and $[C_F]$ are (23×8) stiffness and damping matrices, that transmit the track excitations to the car through 8 tires, $\{q\}$ is a (23×1) vector of generalized

coordinates and $\{q_o\}$ is the displacement excitation vector due to track roughness at the interface of 8 vehicle tires. These vectors are given by:

$$\{q\}' = \{z_{a1}, z_{a2}, z_{a3}, z_{a4}, \theta_{a1}, \theta_{a2}, \theta_{a3}, \theta_{a4}, y_{a1}, y_{a2}, y_{a3}, y_{a4}, z_{bF}, z_{bR}, y_{bF}, y_{bR}, \theta_{bF}, \theta_{bR}, \phi_{bF}, \phi_{bR}, z_c, \theta_c, \phi_c\}$$

$$\{q_o\}' = \{z_{ri}, z_{li}\}; i = 1,..,4$$

where ' ' designates transpose.

The above equations describe the ride dynamic behavior of the car under excitations due to track surface irregularities, while the excitations due to wheel non-uniformity are not present. An eigenvalue problem is formulated to derive the natural frequencies, damping ratios and deflection modes of the vehicle model. The eigenvalue problem was solved using the model parameters summarized in Tables 4.1 and 4.2, which were identified from the design drawings and other information supplied by STM. The inertial and stiffness properties of the various components are taken from [1].

Table 4.1: Vehicle model parameters (Inertial and mount properties).

Parameter	Value
Car body mass, m_c (kg)	16960.0
Car body roll mass moment of inertia, I_{cr} (kg m^2)	54897.0
Car body pitch mass moment of inertia, I_{cp} (kg m^2)	289909.0
Bogie mass, m_b (kg)	3545.0
Bogie roll mass moment of inertia, I_{br} (kg m^2)	590.0
Bogie pitch mass moment of inertia, I_{bp} (kg m^2)	11590.0
Axle mass, m_a (kg)	1685.0
Axle roll mass moment of inertia, I_{ar} (kg m^2)	690.0
Elastomeric spring stiffness, k_s (kN/m)	1900.0
Elastomeric spring damping coefficient, c_s (kN-s/m)	9.0
Rubber mount stiffness, k_r (kN/m)	4000.0
Radial rubber mount stiffness, k_r' (kN/m)	12000.0
Rubber mount damping coefficient c_r (kN-s/m)	1.9
Radial rubber mount damping coefficient, c_r'(kN-s/m)	0.59
Motor mount stiffness, k_m (kN/m)	3500.0
Radial motor mount stiffness, k_m' (kN/m)	10500.0
Motor mount damping coefficient, c_m (kN-s/m)	1.95
Tire stiffness, k_t (kN/m)	1350.0
Radial tire stiffness, k_t'(kN/m)	366.0
Tire damping coefficient, c_t (kN-s/m)	1.0
Radial tire damping coefficient, c_t' (kN-s/m)	0.89
Torsion bar rotational stiffness, k_θ (kNm/rad)	198.74
Torsion bar rotational damping coefficient, c_θ (kNms/rad)	9.0

Table 4.2: Vehicle model parameters (geometry).

Parameter	Value
Longitudinal distance of the front elastomeric springs, l_1 (m)	5.38
Longitudinal distance of the rear elastomeric springs, l_2 (m)	5.73
Longitudinal distance of the springs with respect to c.g. of the front bogie, e_F (m)	0.055

Longitudinal distance of the springs with respect to c.g. of the rear bogie, e_R (m)	0.034
Lateral spacings between the left elastomeric springs and the carbody c.g., a_{lj} $(j = F, R)$ (m)	0.4863
Lateral spacings between the right elastomeric springs and the carbody c.g., a_{rf} $(j = F, R)$ (m)	0.4887
Lateral spacing of the left motor mounts of axle i, d_{li} (m)	0.3313
Lateral spacing of the right motor mounts of axle i, d_{ri} (m)	0.3287
Lateral spacing of the left rubber mounts of axle i, c_{li} (m)	0.4863
Lateral spacing of the right motor mounts of axle i, c_{ri} (m)	0.4887
Lateral spacing of the left tires of axle i, b_{li} (m)	0.9983
Lateral spacing of the right tires of axle i, b_{ri} (m)	0.9957
Vertical distance between the rubber mount and bogie c.g., h_t (m)	0.075
Vertical distance between the rubber mounts and axle c.g., h_1 (m)	0.07
Vertical distance between the axle c.g. and the track datum, h (m)	0.375
Longitudinal distance of inner rubber mounts with respect to c.g. of the bogie of axle i, b_{1i} (m)	0.639
Longitudinal distance of outer rubber mounts with respect to c.g. of the bogie of axle i, b_{2i} (m)	0.999
Longitudinal distance of motor mounts with respect to c.g. of the bogie of axle i, b_{mi} (m)	1.597

Table 4.3 summarizes the natural frequencies (f_{ni}) and corresponding deflection modes of the vehicle model together with damping ratios (ξ_i) and the frequencies of damped oscillations (f_{ndi}). The frequencies of predominant vibration observed from the measured data were also identified and compared with the computed natural frequencies in Table 4.3. The comparisons show reasonably good agreements between the measured and computed frequencies of some of the modes, while considerable differences are evident for other modes.

Car body bounce, roll and pitch modes occur at 2.32 Hz, 1.04 Hz and 2.91 Hz, respectively, which correspond reasonably well with those identified from the

experimental data (2.4, 1.2 and 3 Hz). It should be noted that the lateral vibration responses of vehicle were not reported due to their very low magnitudes. The frequencies of lateral vibration of the car, bogie and axles thus could not be identified from the measured data. The vertical vibration modes of the front and rear bogie were observed to occur at 6.25 Hz and 6.68 Hz, respectively. The differences in their natural frequencies are attributed to relatively higher load on the front bogie. These frequencies also agree reasonably well with those observed from the measured data (≈ 6 Hz). The two bogies exhibit very similar roll and pitch mode frequencies, computed as 9.75 and 4.53 Hz, respectively. The computed bogie pitch frequency is very close to the observed frequency of dominant pitch vibration (≈ 4.5 Hz), while the dominant roll mode vibration frequency could not be clearly identified from the measured data. The mean PSD of measured roll vibration responses revealed peaks in 10-12 Hz and near 18 Hz. Both the axle and bogie appear to be strongly coupled in the 10-12 Hz frequency range, which is mostly attributed to very high stiffness of rubber mounts coupling the bogie and the axles. The measured data suggests the presence of bogie roll mode in 10-12 Hz range, which is higher than the predicted roll mode frequency. This difference is most likely caused by consideration of linear properties of rubber mounts.

On the basis of measured data, it has been reported that axle bounce and roll modes occur near 10 and 18 Hz, respectively [1]. An examination of the measured data together with the eigenvalues and corresponding eigenvectors, revealed that bounce modes of axles attached to front and rear bogies occur at 21.9 Hz and 26.5 Hz, respectively, while the axle roll modes occur at 16.4 Hz and 25.1 Hz, as seen in Table 4.3. Analytical results also suggest that front and rear bogie axles lateral modes occur at frequencies of 37.28 Hz

and 32.52 Hz, respectively, while the experimental results do not give any information about these frequencies. Relatively higher frequencies for the axle lateral modes could be attributed to highly stiff rubber mounts. It needs to be added that the measured responses were reported only for the front bogie axles. The results suggest that the measured roll mode vibration occur near 18 Hz, which is somewhat distant from computed frequency of 21.9 Hz.

Table 4.3: Natural frequencies, corresponding deflection modes and damping ratios.

Natural Frequency (Hz)	Damped Natural Frequency (Hz)	Damping ratio	Dominant modes	Frequencies from measured data (Hz)
1.05	1.04	0.06	Car roll	1.03
1.55	1.55	0.01	Car and Bogie lateral	†
1.55	1.55	0.01	Car and Bogie lateral	†
2.33	2.32	0.05	Car vertical	2.4
2.93	2.92	0.08	Car pitch	2.9
4.54	4.53	0.07	Bogie pitch (Front)	4.5
4.55	4.54	0.07	Bogie pitch (Rear)	4.5
6.27	6.26	0.06	Bogie vertical (Front)	6.0
6.71	6.68	0.08	Bogie vertical (Rear)	6.0
9.77	9.74	0.07	Bogie roll (Front)	10
9.79	9.77	0.07	Bogie roll (Rear)	10
16.41	16.39	0.03	Axle roll ($i = 1,2$)	18
16.41	16.39	0.03	Axle roll ($i = 1,2$)	18
21.93	21.91	0.05	Axle vertical ($i = 1,2$)	10
21.94	21.91	0.05	Axle vertical ($i = 1,2$)	10
25.17	25.11	0.07	Axle roll ($i = 3,4$)	18
25.17	25.11	0.07	Axle roll ($i = 3,4$)	18
26.63	26.59	0.05	Axle vertical ($i = 3,4$)	10
26.62	26.59	0.05	Axle vertical ($i = 3,4$)	10
32.52	32.52	0.01	Axle lateral ($i = 1,2$)	†
32.52	32.52	0.01	Axle lateral ($i = 1,2$)	†
37.29	37.29	0.01	Axle lateral ($i = 3,4$)	†
37.29	37.29	0.01	Axle lateral ($i = 3,4$)	†

† not available

4.2.1 Transfer functions

The vibration modes corresponding to identified natural frequencies are further verified through analyses of magnitudes of transfer functions of the vehicle model. The equation of motion, Eq. (4.1), is analyzed to derive the frequency response function matrix, assuming the excitation and response functions of the form:

$$\{q_o\} = \{Q_o\} e^{i\omega t} \quad \text{and} \quad \{q\} = \{Q\} e^{i\omega t} \tag{4.2}$$

where $\{Q_o\}$ and $\{Q\}$ represent the magnitudes of harmonic excitation and responses. The transfer functions are derived assuming identical vertical inputs $(z_{ri} = z_{li} = z_o)$ at all the car wheels. The roll and pitch modes of the vehicle components, however, are also excited due to geometric asymmetry. The mass centers of the axle, bogie and car body do not coincide with their respective geometric centers, as evident from nominal model parameters presented in Table 4.2. The responses and excitation vectors, $\{Q\}$ and $\{Q_o\}$, are related to the frequency response function as:

$$\{Q(i\omega)\} = [H(i\omega)]\{Q_o(i\omega)\} \tag{4.3}$$

$$\text{where} [H(i\omega)] = [-\omega^2[M] + i\omega[C] + [K]]^{-1} * [[K_F] + i\omega[C_F]] \tag{4.4}$$

The magnitudes of transfer function are subsequently derived from the frequency response function matrix. Figure 4.1 presents the magnitude transfer function of car body $(|z_c / z_o|)$, front bogie $(|z_{bF} / z_o|)$ and front axle $(|z_{a1} / z_o|)$ in the vertical mode, which reveals peak magnitudes near the car bounce and bogie bounce frequencies of 2.3 and 6 Hz, respectively. The figure also suggests strong coupling between the car body, bogie and axle in the bounce mode. The peak magnitude of car body response at the

frequency of 2.3 Hz is higher than those of the bogie and the axle. The bogie and axle responses show near identical magnitudes at a frequency of 6 Hz (vertical mode resonance of the bogie), which suggests strong coupling between the bogie and axle in the vertical mode. The axle bounce response also reveals a small magnitude peak near 21 Hz, which corresponds to the front axle roll mode.

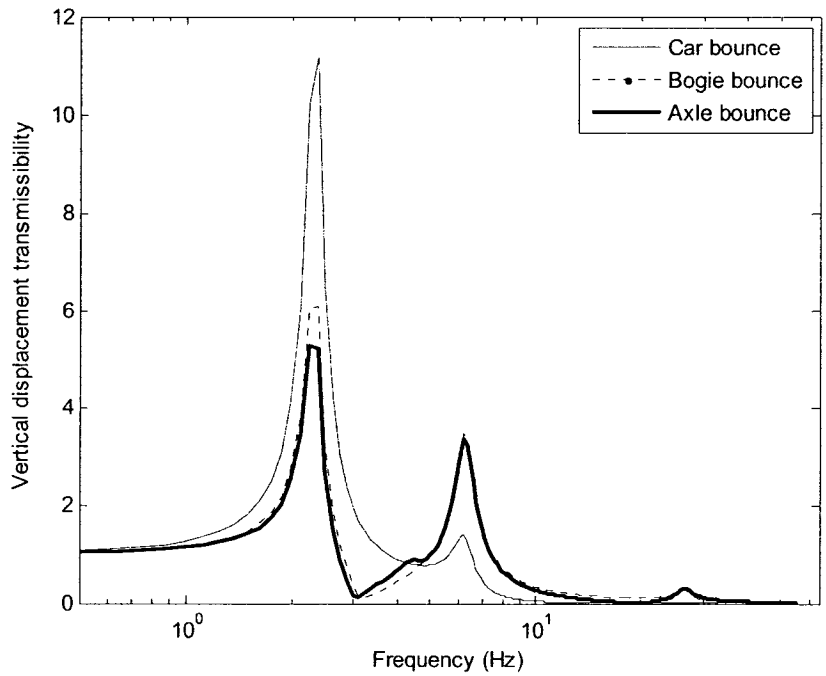

Figure 4.1: Vertical displacement transmissibility magnitude response of the car body, front bogie and front axle.

The roll vibration transmissibility response of the car body $(|\theta_c / z_o|)$, front bogie $(|\theta_{bF} / z_o|)$ and front axle $(|\theta_{a1} / z_o|)$ are illustrated in Fig. 4.2. The responses exhibit peaks near 1, 2.3, 9.7, and 21 Hz, which correspond to resonant frequencies associated with car body roll, car body vertical, bogie roll and axle roll modes, respectively. The magnitude of car body roll transfer function near the roll mode frequency (1 Hz) is significantly larger than those of bogie and axle, as it was observed for the vertical transfer function. The car body roll response near its vertical mode frequency (2.3 Hz) is also considerably

large, suggesting strong coupling between the vertical and roll modes. Strong couplings are also evident in bogie and axle roll response as it is evident from their comparable peak magnitudes at frequencies of 9 Hz and 16 Hz, corresponding to bogie and axle roll modes, respectively. This strong coupling is attributed to high stiffness of the rubber mounts coupling the bogie and axles.

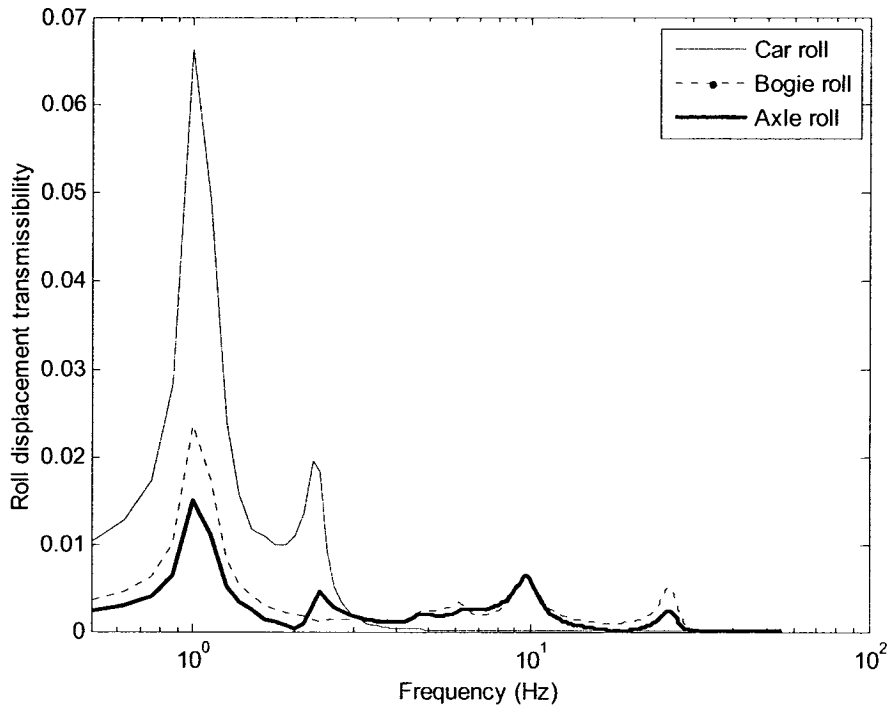

Figure 4.2: Roll displacement transmissibility magnitude response of the car body, front bogie and front axle.

Figure 4.3 illustrates the pitch vibration transmissibility response of the car body $(|\phi_c / z_o|)$ and front bogie $(|\phi_{bF} / z_o|)$. The responses exhibit peaks at 2.3, 2.9, 4.5, 6 and 26.6 Hz, which correspond to resonant frequencies associated with car body vertical, car body pitch, bogie pitch, bogie vertical and axle vertical modes. The overall magnitude of car body pitch transfer function is smaller when compared to the bogie response. The experimental data also revealed significantly smaller magnitude of car body pitch, when

compared to bogie pitch response. Car pitch transfer function shows small magnitude peaks around 2.3 and 2.9 Hz, corresponding to car bounce and car pitch modes respectively. Peak response at 6 Hz is also visible in car pitch transfer function suggesting coupling between car pitch and bogie bounce modes. Bogie pitch transfer function demonstrates strong coupling between car bounce and bogie pitch modes, which is evident from high magnitude peaks appearing at 2.3 and 4.5 Hz, corresponding to car bounce and bogie pitch, respectively. Bogie response also reveals peaks at 6 Hz and 26.6 Hz, corresponding to bogie and axle bounce modes, respectively. The axle bounce peak, however, is very small in magnitude.

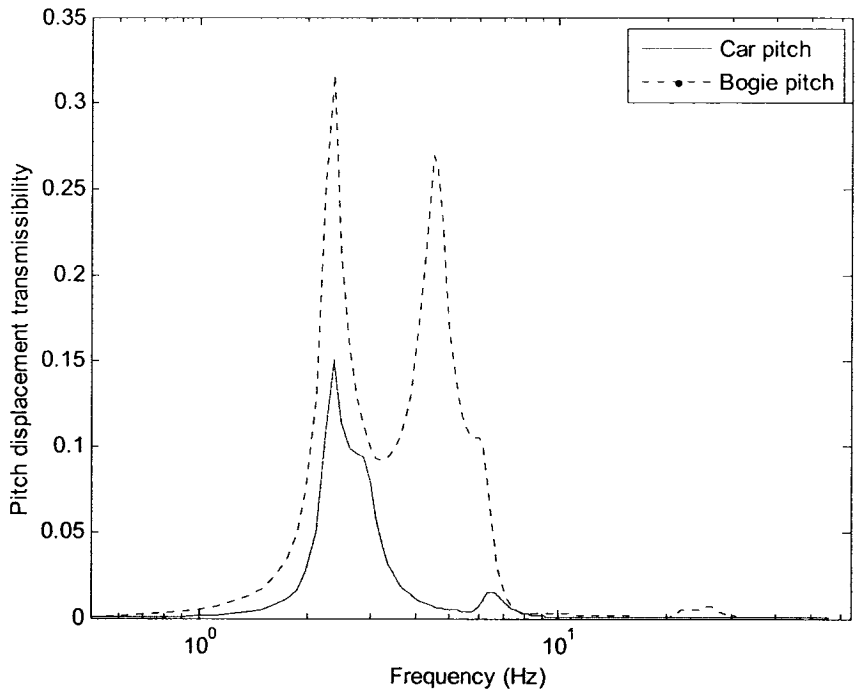

Figure 4.3: Pitch displacement transmissibility magnitude response of the car body, front bogie and front axle.

4.3 RIDE RESPONSE TO RANDOM TRACK ROUGHNESS

In the linearized analysis of a multi-degrees-of-freedom system, the use of frequency response function along with power spectral density representation of the input has been the basis of frequency domain analysis, such that :

$$\left[S_r(i\omega)\right]=\left[H_r^*(i\omega)\right].\left[S_F(i\omega)\right].\left[H_r(i\omega)\right]' \tag{4.5}$$

where $\left[S_r(i\omega)\right]$ represents the (23×8) spectral density matrix of the displacement response variables due to track excitation alone, $\left[S_F(i\omega)\right]$ represents the (8×8) matrix consisting of track roughness excitation displacement PSD, and $\left[H_r(i\omega)\right]$ denotes the (23×23) transfer function matrix defined in Eq. (4.4). The matrix $\left[H_r^*(i\omega)\right]$ is the complex conjugate of $\left[H_r(i\omega)\right]$. The excitation at different wheels is considered to be correlated. The tires of adjacent axles encounter identical track surface displacement with a time delay, as described in section 2.4.1. The differential vertical inputs encountered at the left and right tires of an axle were also related through random roll distribution in Eq. (2.18). The PSD of displacement excitation $\left[S_F(i\omega)\right]$ due to track roughness is formulated as:

$$\begin{bmatrix}
S_l & S_r e^{-i2\phi} & S_l e^{-i\omega t12} & S_r e^{-i2\phi-i\omega t12} & \cdot & \cdot & \cdot & S_r e^{-i2\phi-i\omega t14} \\
S_l e^{j2\phi} & S_r & S_l e^{j2\phi-i\omega t12} & S_r e^{-i\omega t12} & \cdot & \cdot & \cdot & S_r e^{-i\omega t14} \\
S_l e^{j\omega t12} & S_r e^{-i2\phi+i\omega t12} & S_l & S_r e^{-i2\phi} & \cdot & \cdot & \cdot & S_r e^{-i2\phi-i\omega t13} \\
S_l e^{j2\phi+i\omega t12} & S_r e^{j\omega t12} & S_l e^{j2\phi} & S_r & \cdot & \cdot & \cdot & S_r e^{-i\omega t13} \\
\cdot & \cdot & \cdot & \cdot & \cdot & \cdot & \cdot & S_r e^{-i2\phi-i\omega t12} \\
\cdot & \cdot & \cdot & \cdot & \cdot & \cdot & \cdot & S_r e^{-i\omega t12} \\
\cdot & \cdot & \cdot & \cdot & \cdot & \cdot & \cdot & S_r e^{-i2\phi} \\
S_l e^{j2\phi+i\omega t14} & S_r e^{j\omega t14} & S_l e^{j2\phi+i\omega t13} & S_r e^{j\omega t13} & S_l e^{j2\phi+i\omega t12} & S_r e^{j\omega t12} & S_l e^{j2\phi} & S_r
\end{bmatrix} \tag{4.6}$$

Where S_l and S_r are the auto PSD's of left and right track roughness, respectively, $\omega = 2\pi f$ and ϕ is random roll angle, as described in section 2.4.1 and t_{jk} defines the time delay between excitations at wheel j and wheel k, which is related to forward speed and longitudinal distance between wheels j and k.

The diagonal elements of the response PSD matrix $\left[S_r(i\omega)\right]$ represent the spectral densities of the displacement response of the generalized coordinates. The off-diagonal elements are the cross spectral densities of the generalized coordinate. Ride responses, however, are widely assessed in terms of acceleration. The PSD of acceleration responses can be derived from:

$$\left[S_{\ddot{r}}(i\omega)\right] = (i\omega)^4 \left[S_r(i\omega)\right] \tag{4.7}$$

Equation (4.5) is solved together with equations of motion to compute the PSD of ride acceleration responses of the car components due to roughness of the left and right tracks. Figure 4.4 illustrates a comparison of auto PSD of acceleration due to roughness properties of the left (S_l) and right tracks (S_r) at a forward speed of 60 km/h. the results clearly show some differences in the magnitudes and frequency components of acceleration PSD's of the two tracks, which give rise to roll excitation of the vehicle system.

Figure 4.5 illustrates PSD of vertical acceleration responses of the car body mass, front bogie mass and front axle mass, for a constant forward speed of 60 km/h. The results show considerably higher magnitudes of vertical acceleration PSD's at low frequencies in the 2-10 Hz frequency range. The high magnitude peaks are attributed to various resonances of the car body and bogie in this frequency range. Relatively lower

magnitude peaks are also evident at relatively higher frequencies (16 to 26 Hz) associated with natural frequencies of the axle. The vertical acceleration response of the car body, bogie and axle clearly show large peaks corresponding to vertical mode resonances of the car (2.3 Hz) and the bogie (6.25 Hz). The responses also exhibit peaks corresponding to car and bogie pitch modes (2.9 and 4.5 Hz). These peaks are particularly evident in the bogie and axle acceleration responses, suggesting stronger coupling between the axle and bogie. The magnitudes of car body vertical acceleration responses corresponding to the pitch mode frequencies, however, are significantly small, suggesting effective attenuation of vibration near these frequencies by the car suspension. Both the bogie and axle vertical responses also exhibit secondary peaks in the 16-26 Hz range. A relatively larger magnitude peak is observed near the axle vertical mode frequency of 21 Hz. The axle acceleration response also exhibit peaks near its roll mode frequency (16 Hz) and vertical mode frequency of rear bogie axles (26 Hz). The results further confirm that the front axle vertical modes occur near 21 Hz rather then the reported frequency of 10 Hz [1], as given in Table 4.3.

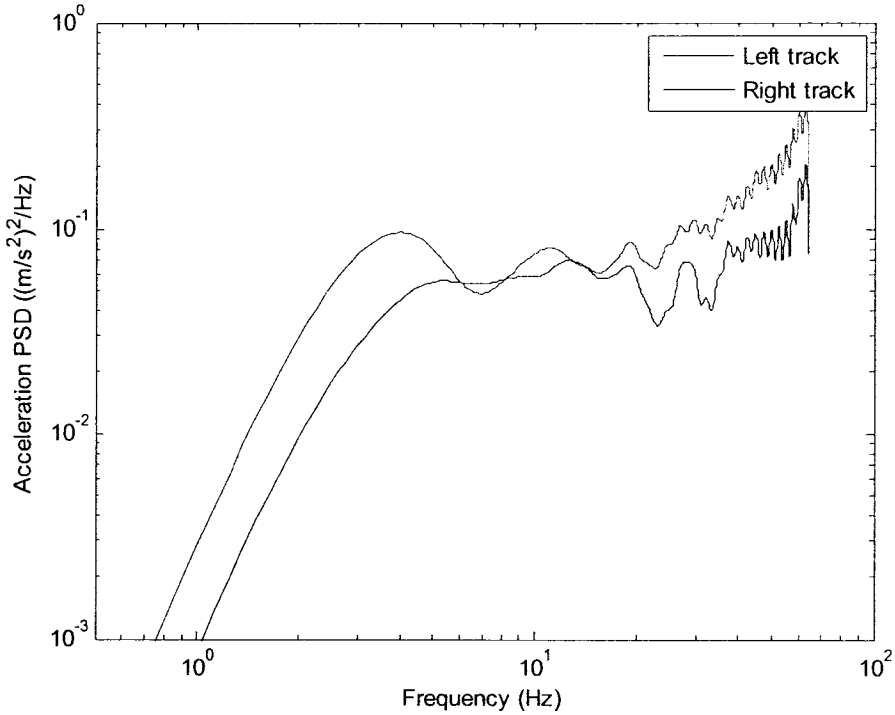

Figure 4.4: Comparison of acceleration PSD's due to roughness of left and right tracks ($v = 60$ km/h).

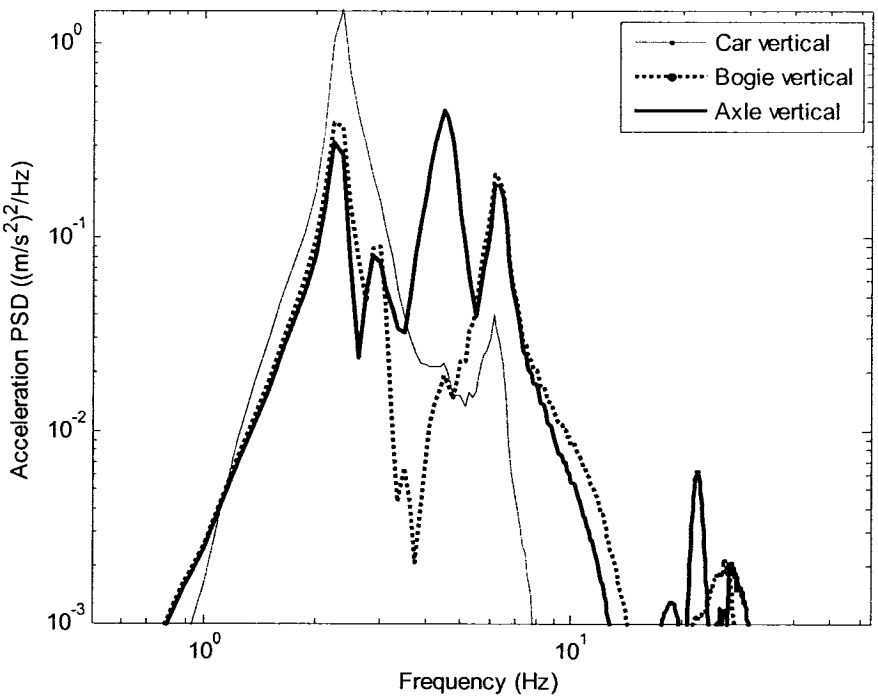

Figure 4.5: PSD of vertical acceleration responses of the car, front bogie and front axle ($v = 60$ km/h).

Figure 4.6 illustrates PSD's of roll acceleration responses of the car body, front bogie and front axle. The results show considerably higher magnitudes of roll acceleration at relatively higher frequencies of 9.7 and 16.4 Hz, corresponding to bogie and axle roll resonant frequencies, respectively. Car body roll response reveals high magnitude near 1 Hz with other peaks visible at 2.3 Hz and 9.7 Hz with decreasing order of magnitudes, respectively. These frequencies correspond to car body roll, car body bounce and bogie roll modes, respectively. Experimental data suggested that the peak at 10 Hz is related to axle bounce mode, while the mathematical model results reveal that this frequency largely corresponds to bogie roll mode. The bogie acceleration response shows high roll response at 1, 9.7 and 25.2 Hz, corresponding to car body roll, bogie roll and axle roll resonant frequencies, respectively. Bogie roll acceleration response is relatively higher when compared to the car body and axle roll responses. The axle roll response reveal major peaks at 1, 9.7, 16.4 and 25.2 Hz, which correspond to car body roll, bogie roll, front axle roll and rear bogie's axle roll modes. Experimental data also revealed front axle roll mode in the 16-18 Hz frequency range.

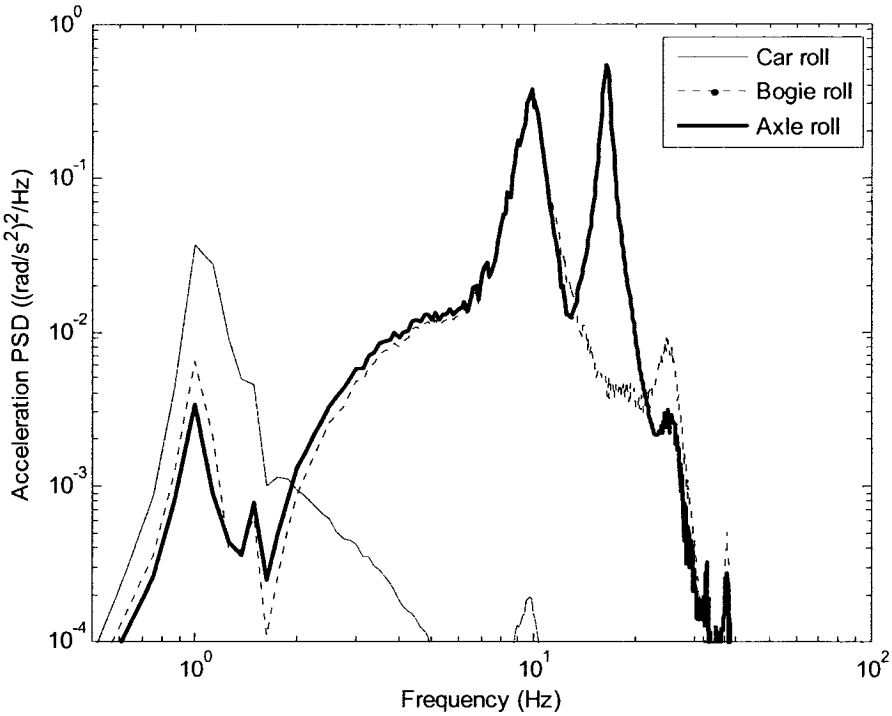

Figure 4.6: PSD of roll acceleration responses of the car, front bogie and front axle ($v = 60$ km/h).

Figure 4.7 illustrates PSD's of pitch acceleration responses of the car body and front bogie, respectively. The magnitude of car pitch acceleration response is considerably smaller in comparison with the bogie pitch acceleration, which was also evident from the pitch transfer functions of the car body and bogie (Fig. 4.3). The car body pitch acceleration response exhibit peaks near 2.3, 2.9, 4.5 and 6.3 Hz, corresponding to car body vertical, car body pitch, bogie pitch and bogie vertical modes, respectively. Bogie pitch acceleration response reveals single large peak at 4.5 Hz, which corresponds to bogie pitch mode. The response peaks of considerably smaller magnitudes are also observed at 9.6, 16.4 and 21.9 Hz, corresponding to bogie roll, axle roll and axle vertical modes, respectively.

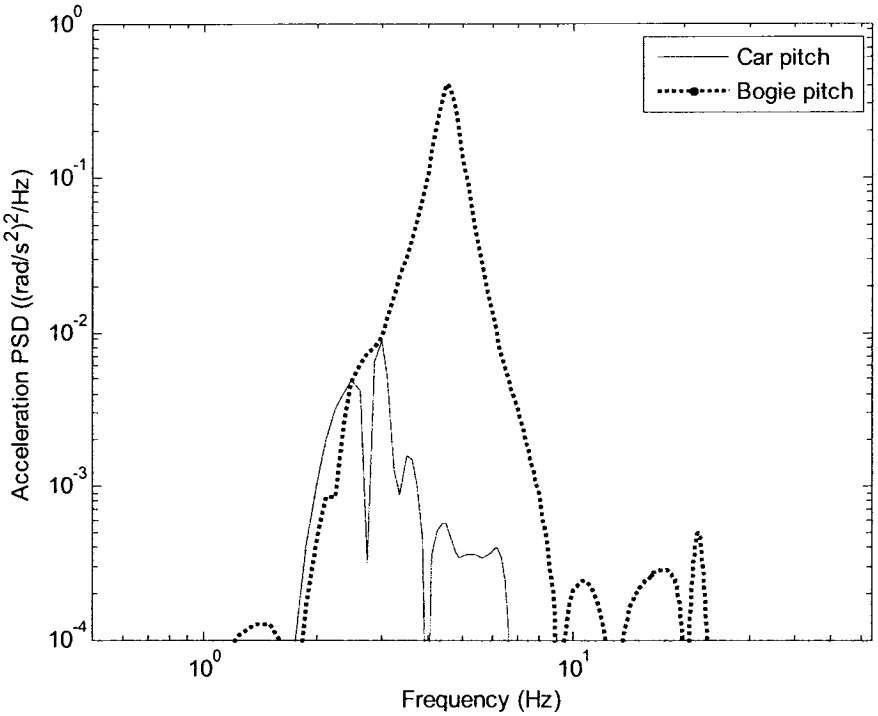

Figure 4.7: PSD of pitch acceleration responses of the car and front bogie ($v = 60$ km/h).

4.4 RESPONSE ANALYSIS DUE TO WHEEL UNBALANCE

Apart from the tire interactions with the randomly rough track, the wheel non-uniformity and mass unbalance can affect the vehicle ride response in a significant manner [39]. The mass unbalance is known to impose an excitation at a frequency corresponding to angular speed of the tires. A mass unbalance is mostly caused by uneven mass distribution of the wheel and axle assembly. A non-uniform tire tread also yields a mass unbalance apart from the excitation due to its OOR geometry. In this study, the measured OOR data for tires of the MR-73-2A car are analyzed to determine its equivalent mass unbalance. Location and magnitude of tire OOR and the corresponding eccentricity value is provided in Table 4.4. The forward speed is chosen as the nominal operating speed of 60 km/h.

Table 4.4: Tire non-uniformity (OOR) and eccentricity parameters.

Tire location	OOR value (mm)	Eccentricity (mm)
Axle 1, left tire	1.75	0.255
Axle 1, right tire	2.25	0.493
Axle 2, left tire	2.0	0.373
Axle 2, right tire	1.25	0.166
Axle 3, left tire	2.0	0.373
Axle 3, right tire	1.25	0.166
Axle 4, left tire	1.5	0.193
Axle 4, right tire	1.5	0.193

The equations of motion of the vehicle model subject to wheel unbalance alone can be rewritten as:

$$[M]\{\ddot{q}\}+[C]\{\dot{q}\}+[K]\{q\}=\{f^{u}(t)\} \tag{4.8}$$

where $f^{u}(t)$ is the forcing vector of tire forces due to mass unbalance.

The above formulation considers perfectly flat track surface$(z_{ri}=z_{li}=0)$. The presence of a wheel mass unbalance directly influences the dynamic response of axles, particularly in the vertical and roll modes, as evident in Eq. (2.1) and (2.3). The mass unbalance also contributes to the car body and bogie responses due to coupling between the components. The wheel mass unbalance force vector can be related to the mass unbalance and eccentricity as:

$$f^{u}(t)=[m_{u}]\{E\} \tag{4.9}$$

where $\{E\}$ is (8×1) vector of mass eccentricities, as described in section 2.4.2, and $[m_{u}]$ is (23×8) matrix of excitation coefficients due to mass unbalance, given by:

$$\begin{Bmatrix} m\omega^2 & m\omega^2 & 0 & 0 & 0 & 0 & 0 & 0 \\ 0 & 0 & m\omega^2 & m\omega^2 & 0 & 0 & 0 & 0 \\ 0 & 0 & 0 & 0 & m\omega^2 & m\omega^2 & 0 & 0 \\ 0 & 0 & 0 & 0 & 0 & 0 & m\omega^2 & m\omega^2 \\ b_{l1}m\omega^2 & -b_{r1}m\omega^2 & 0 & 0 & 0 & 0 & 0 & 0 \\ 0 & 0 & b_{l2}m\omega^2 & -b_{r2}m\omega^2 & 0 & 0 & 0 & 0 \\ 0 & 0 & 0 & 0 & b_{l3}m\omega^2 & -b_{r3}m\omega^2 & 0 & 0 \\ 0 & 0 & 0 & 0 & 0 & 0 & b_{l4}m\omega^2 & -b_{r4}m\omega^2 \\ 0 & 0 & 0 & 0 & 0 & 0 & 0 & 0 \\ | & & & & & & & | \\ | & | & | & | & | & | & | & | \\ | & & & & & & & | \\ | & | & | & | & | & | & | & | \\ 0 & - & - & - & - & - & - & 0 \end{Bmatrix}_{23\times 8}$$

where b_{li} and b_{ri} are the lateral distances of the left and right tires on axle i. Frequency response matrix, $\left[H_u(i\omega)\right]$ due to mass unbalance alone can be derived assuming $\{E\}$ as the excitation vector:

$$\left[H_u(i\omega)\right] = \left[-\omega^2[M] + i\omega[C] + [K]\right]^{-1} * [m_u] \tag{4.10}$$

The PSD of displacement responses of the vehicle model can be derived from:

$$\left[S_u(i\omega)\right] = \left[H_u^*(i\omega)\right].\left[S_e(i\omega)\right].\left[H_u(i\omega)\right]' \tag{4.11}$$

where $\left[S_u(i\omega)\right]$ is displacement PSD response matrix and $\left[S_e(i\omega)\right]$ is a displacement PSD matrix due to eccentricities e_i^p ($i = 1,..,4$ and $p = l, r$).

The vehicle response due to mass unbalance is also evaluated in the frequency domain, where the wheel eccentricity is expressed by its auto spectral density similar to the track roughness excitation. Considering the harmonic nature of the eccentricity, $e_i^p \sin(\omega t - \phi_i)$, and thus the unbalanced force, the auto PSD of mass unbalance due to left wheel of the front axle (considered as the reference) is estimated as $(e_1^l)^2/2$ in m^2/Hz. An equivalent PSD excitation matrix is formulated in similar manner

by considering the phase difference of a particular wheel with respect to the reference wheel, ϕ_{i1}^{p}, such that:

$$\left[S_e(i\omega)\right] = \begin{bmatrix} S_1^l & 0 & 0 & 0 & 0 & 0 & 0 & 0 \\ 0 & S_1^r e^{-i\phi_{11}^r} & 0 & 0 & 0 & 0 & 0 & 0 \\ 0 & 0 & S_2^l e^{-i\phi_{21}^l} & 0 & 0 & 0 & 0 & 0 \\ 0 & 0 & 0 & S_2^r e^{-i\phi_{21}^r} & 0 & 0 & 0 & 0 \\ 0 & 0 & 0 & 0 & S_3^l e^{-i\phi_{31}^l} & 0 & 0 & 0 \\ 0 & 0 & 0 & 0 & 0 & S_3^r e^{-i\phi_{31}^r} & 0 & 0 \\ 0 & 0 & 0 & 0 & 0 & 0 & S_4^l e^{-i\phi_{41}^l} & 0 \\ 0 & 0 & 0 & 0 & 0 & 0 & 0 & S_4^r e^{-i\phi_{41}^r} \end{bmatrix}$$

where $S_i^p = (e_i^p)^2/2$ is the PSD due to eccentricity of wheel p $(p = l, r)$ of axle i and $e^{-i\phi_{i1}^p}$ accounts for the phase difference between tire p on axle i and the reference tire. The PSD of ride acceleration responses due to wheel unbalance alone is subsequently computed from:

$$\left[S_{\ddot{u}}(i\omega)\right] = (i\omega)^4 \left[S_u(i\omega)\right] \tag{4.12}$$

Figures 4.8 and 4.9 illustrate PSD's of car and axle vertical acceleration responses due to mass-unbalance alone. Force due to mass-unbalance is modeled by a deterministic function with a single frequency component occurring at tire angular frequency of 6 Hz. The response PSD thus exhibits a single peak at 6 Hz. The unbalance force directly affects the axle response which is clear from the high magnitude peak appearing in axle vertical response, when compared to car vertical response.

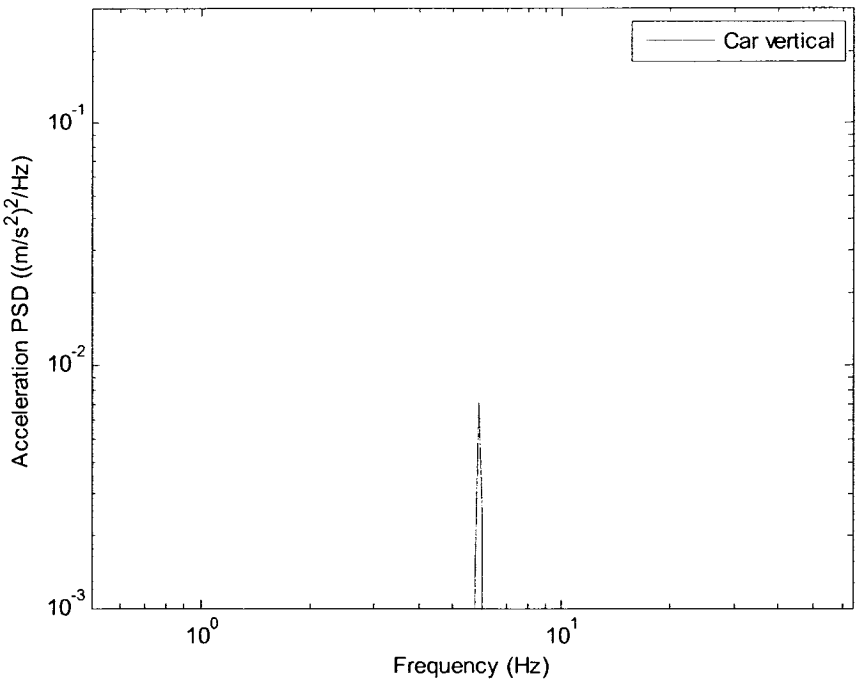

Figure 4.8: PSD of vertical acceleration response of the car body due to mass unbalance ($v = 60$ km/h).

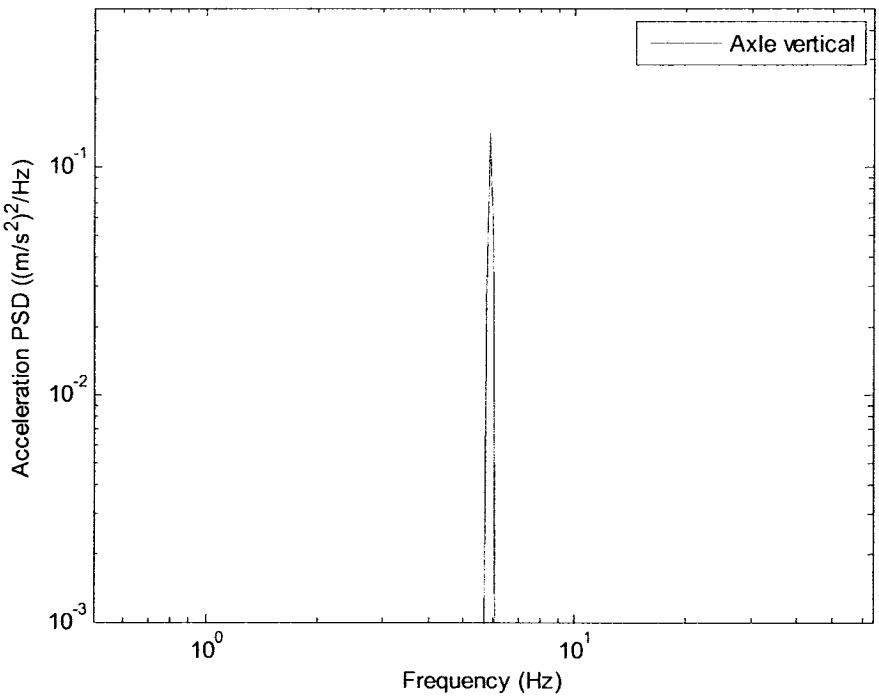

Figure 4.9: PSD of vertical acceleration response of the axle due to mass unbalance ($v = 60$ km/h).

4.5 RESPONSE ANALYSIS DUE TO TIRE NON-UNIFORMITY

A non-uniform tire tread is assumed to provide displacement excitation to the vehicle system. The resulting excitation force developed due to non-uniformity of the tire tread appears in the axle bounce and roll equations of motion, Eqs. (2.1) and (2.3), respectively. Tire non-uniformity may be modeled in different ways, as described in chapter 1. The measured data revealed that cars with older tires had larger magnitude of acceleration response when compared to ride acceleration responses of cars with new tires. High magnitudes of vertical vibration were observed at 4.5 Hz over some of the track segments, when vehicle speed was near 50 km/h (tire rolling frequency near 4.5 Hz) and at 6 Hz over other segments when vehicle speed was near 62 km/h (tire rolling frequency near 6 Hz). This implies that responses due to non-uniformity dominate at the angular speed of the wheels. The vehicle model was analyzed considering a fixed value of non-uniformity taken as the highest measured value. In the following analysis non-uniformity of MR-73-2A tires is considered, as given in Table 4.4 and vehicle speed is taken as 60 km/h.

Modeling of tire non-uniformity is described in section 2.4.3 and variation in the wheel radius with the angular coordinate was illustrated in Fig 2.9. Fig. 4.10 illustrates the variations in wheel radius as a function of the forward distance traveled by the wheel. This radius variation is considered as a displacement input to the wheel, similar to the track roughness excitation, in order to determine the vehicle response to tire non-uniformity. The variations in the radial run out cause an additional tire force, F_{ip}^{n}, transmitted to the axle assembly, as it is evident from Eqs. (2.1) and (2.3). The equations

of motion of the vehicle model subject to displacement input due to radius variations of the tire tread alone can be rewritten as:

$$[M]\{\ddot{q}\}+[C]\{\dot{q}\}+[K]\{q\}=\{f^n(t)\} \tag{4.13}$$

where $f^n(t)$ is the forcing vector of tire forces due to tire OOR.

The above formulation considers perfectly flat track surface $(z_{ri}=z_{li}=0)$. The tire non-uniformity force vector can be related to the tire stiffness properties and radial run-out of the tire tread as:

$$f^n(t)=[K_F]\{\triangle r_i^p\}+[C_F]\{\triangle \dot{r}_i^p\} \tag{4.14}$$

where $\{\triangle r_i^p\}$ and $\{\triangle \dot{r}_i^p\}$ are (8×1) vectors of radius variation and its time rate of change, as described in section 2.4.3. $[K_F]$ and $[C_F]$ are (23×8) matrices of excitation coefficients due to tire stiffness and damping properties, respectively. The excitation matrix due to tire stiffness $[K_F]$ is given by:

$$\begin{bmatrix}
k_t & k_t & 0 & 0 & 0 & 0 & 0 & 0 \\
0 & 0 & k_t & k_t & 0 & 0 & 0 & 0 \\
0 & 0 & 0 & 0 & k_t & k_t & 0 & 0 \\
0 & 0 & 0 & 0 & 0 & 0 & k_t & k_t \\
b_{l1}k_t & -b_{r1}k_t & 0 & 0 & 0 & 0 & 0 & 0 \\
0 & 0 & b_{l2}k_t & -b_{r2}k_t & 0 & 0 & 0 & 0 \\
0 & 0 & 0 & 0 & b_{l3}k_t & -b_{r3}k_t & 0 & 0 \\
0 & 0 & 0 & 0 & 0 & 0 & b_{l4}k_t & -b_{r4}k_t \\
| & | & | & | & | & | & | & | \\
| & | & | & | & | & | & | & | \\
0 & - & - & - & - & - & - & 0
\end{bmatrix}$$

Frequency response matrix, $\left[H_n(i\omega)\right]$, due to tire OOR alone can be derived assuming $\left\{\Delta r_i^p\right\}$ as the excitation vector:

$$\left[H_n(i\omega)\right]=\left[-\omega^2[M]+i\omega[C]+[K]\right]^{-1}*\left[[K_F]+i\omega[C_F]\right] \tag{4.15}$$

The PSD of displacement responses of the vehicle model can be derived from:

$$\left[S_n(i\omega)\right]=\left[H_n^*(i\omega)\right].\left[S_{\Delta r}(i\omega)\right].\left[H_n(i\omega)\right]' \tag{4.16}$$

where $\left[S_n(i\omega)\right]$ is displacement PSD response matrix and $\left[S_{\Delta r}(i\omega)\right]$ is a displacement PSD matrix due to wheel radius variations Δr_i^p ($i=1,..,4$ and $p=l,r$).

The vehicle response due to tire OOR is also evaluated in the frequency domain, where the radius variation of the non-uniform tire treads is expressed by its auto spectral density similar to the track roughness excitation. An equivalent PSD excitation matrix is formulated in a similar manner by considering the phase difference of a particular wheel non-uniformity with respect to the reference wheel, ϕ_{i1}^p, such that:

$$\left[S_{\Delta r}(i\omega)\right]=\begin{bmatrix} P_1^l & 0 & 0 & 0 & 0 & 0 & 0 & 0 \\ 0 & P_1^r e^{-i\phi_{11}^r} & 0 & 0 & 0 & 0 & 0 & 0 \\ 0 & 0 & P_2^l e^{-i\phi_{21}^l} & 0 & 0 & 0 & 0 & 0 \\ 0 & 0 & 0 & P_2^r e^{-i\phi_{21}^r} & 0 & 0 & 0 & 0 \\ 0 & 0 & 0 & 0 & P_3^l e^{-i\phi_{31}^l} & 0 & 0 & 0 \\ 0 & 0 & 0 & 0 & 0 & P_3^r e^{-i\phi_{31}^r} & 0 & 0 \\ 0 & 0 & 0 & 0 & 0 & 0 & P_4^l e^{-i\phi_{41}^l} & 0 \\ 0 & 0 & 0 & 0 & 0 & 0 & 0 & P_4^r e^{-i\phi_{41}^r} \end{bmatrix}$$

where P_i^p is the PSD due to OOR of wheel p $(p = l, r)$ of axle i. The PSD of ride acceleration responses due to wheel unbalance non-uniformity is subsequently computed from:

$$\left[S_{\ddot{n}}(i\omega)\right] = (i\omega)^4 \left[S_n(i\omega)\right] \tag{4.17}$$

Figure 4.11 illustrates the effective roughness properties of a track equivalent of the tire non-uniformity. The acceleration PSD, derived at a forward speed of 60km/h, reveals peaks at 6 Hz and at frequency multiples of tire angular frequency of 6 Hz. Fig. 4.12 illustrates the PSD's of vertical acceleration responses of the car body, front bogie and front axle, respectively, due to wheel non-uniformity alone. The vertical acceleration responses of the car body, bogie and axle reveal high magnitude peaks at 6 Hz, which corresponds to the primary component of the excitation force. Bogie and axle responses exhibit similar magnitude peaks at 6 Hz. Magnitude of the 6 Hz component in bogie and axle response is higher when compared to car body response, which could be due to the fact that the resonant frequency corresponding to bogie vertical mode is 6 Hz. Moreover, the car body suspension would effectively suppress the magnitude of vibration transmitted near 6 Hz. Both bogie and axle responses reveal peaks near car body vertical (2.3 Hz) and car body pitch (2.9 Hz) mode frequencies, while the axle response shows an additional peak at bogie pitch resonant frequency (4.5 Hz).

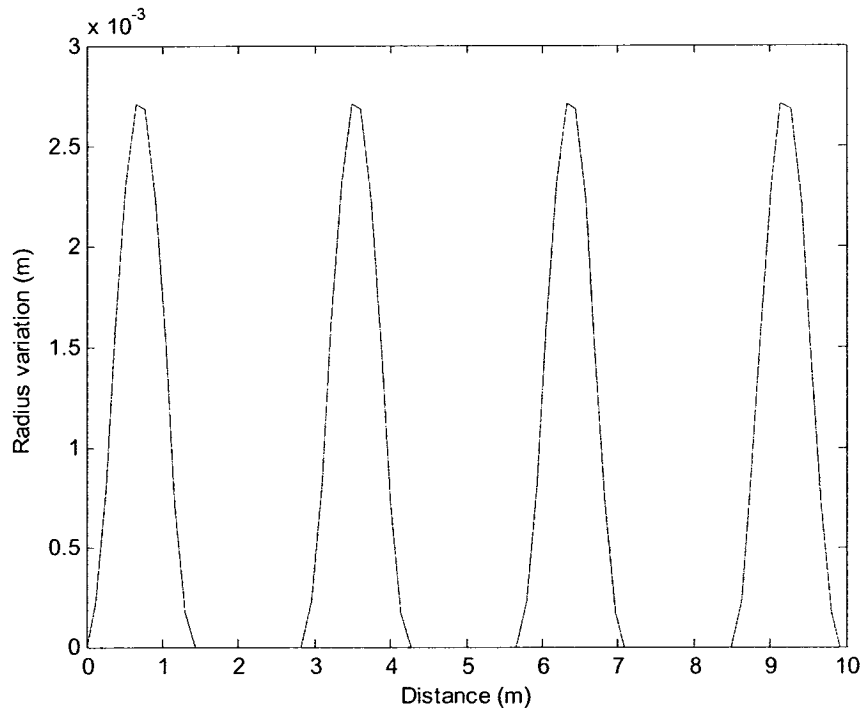

Figure 4.10: Radius variation with respect to forward distance.

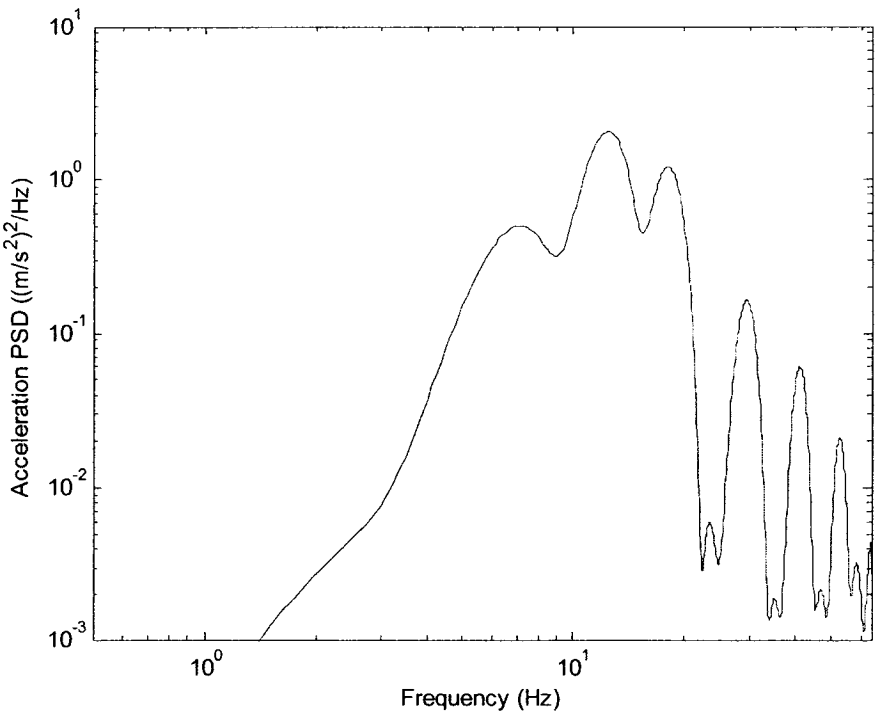

Figure 4.11: Effective acceleration PSD due to tire non-uniformity.

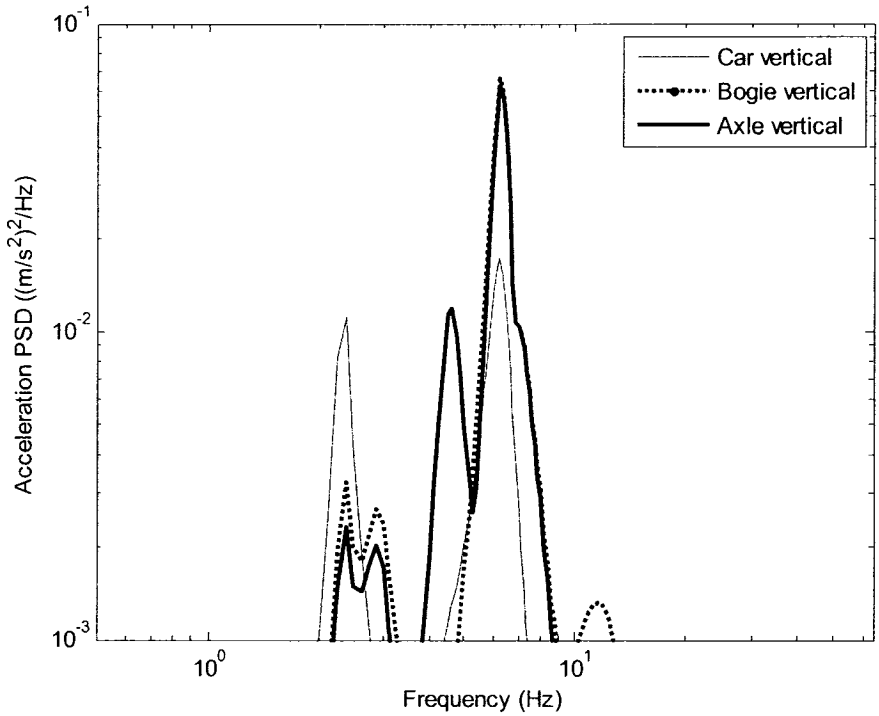

Figure 4.12: PSD of vertical acceleration responses of the car, front bogie and front axle due to non-uniformity of tire tread ($v = 60$ km/h).

4.6 RESPONSE DUE TO COMBINED TRACK ROUGHNESS AND WHEEL DEFECTS

In previous sections, the vehicle responses were determined due to individual excitations. Furthermore, also the responses were computed at the mass centers of the car body, bogie and the axle. The total ride dynamic responses of the model, due to combined affects of track roughness and wheel defects are evaluated in order to examine the model validity on the basis of available measured data. Principle of superposition is applied to compute the responses due to combined excitations, such that:

$$[M]\{\ddot{q}\}+[C]\{\dot{q}\}+[K]\{q\}=\{f(t)\}+\{f^{u}(t)\}+\{f^{n}(t)\} \tag{4.18}$$

where $\{f(t)\}$, $\{f^{u}(t)\}$ and $\{f^{n}(t)\}$ are the excitation force vectors due to track roughness, mass unbalance and tire non-uniformity, respectively.

In order to examine the model validity, the responses are evaluated at or near the measurement locations. These measurement locations have been described in chapter 3. The vertical responses of the car body, front bogie and front axle, alone, at the identified measurement locations, however, were evaluated from the generalized response coordinates, such that:

$$\begin{bmatrix} \ddot{z}_c^m \\ \ddot{z}_b^m \\ \ddot{z}_a^m \end{bmatrix} = [T]\{\ddot{q}_T\} \tag{4.19}$$

where $\ddot{z}_c^m$, $\ddot{z}_b^m$ and $\ddot{z}_a^m$ are vertical acceleration responses at selected locations of measurements, where $\{\ddot{q}_T\}$ is the vector of acceleration responses at generalized coordinates, given by:

$$\{\ddot{q}_T\} = \{\ddot{z}_c \quad \ddot{\phi}_c \quad \ddot{\theta}_c \quad \ddot{z}_{bF} \quad \ddot{\phi}_{bF} \quad \ddot{\theta}_{bF} \quad \ddot{z}_{a1} \quad \ddot{\theta}_{a1}\} \tag{4.20}$$

In the above equation, $[T]$ is the transformation matrix, given by:

$$[T] = \begin{bmatrix} 1 & l_1 & a_1 & 0 & 0 & 0 & 0 & 0 \\ 0 & 0 & 0 & 1 & l_2 & a_2 & 0 & 0 \\ 0 & 0 & 0 & 0 & 0 & 0 & 1 & a_3 \end{bmatrix} \tag{4.21}$$

Where l_1 and l_2 are the longitudinal distances of measurement locations from the carbody and bogie mass centers, respectively, while a_1, a_2 and a_3 are the transverse distances of the measurement locations from the carbody, bogie and axle mass centers, respectively.

Comparisons between the model and experimental results for vertical acceleration responses of the car body, front bogie and front axle are illustrated in Figs. 4.13 to 4.15, respectively. The model results generally show trends that are comparable with the measured data. The comparison suggests that model responses in the 1-20 Hz frequency

range agree reasonably well with those the measured responses. Some of the peaks evident in the experimental results could not be observed in the model responses; these may be attributed to flexural modes of the car body. It has been reported that certain flexible body modes are also excited in the 1-20 Hz frequency range [19, 20]. During experiments conducted on the metro vehicle it was determined that the vertical bending mode of the car body occurs near 10 Hz. Although the model vertical responses do not show peaks around 10 Hz, the experimental results show a number of peaks in the 10-15 Hz range. These peaks are particularly appreciable in the car vertical response, suggesting presence of flexible car body modes. While the frequencies of dominant peaks in model responses correspond well with those of measured results, the magnitudes of model and measured response peaks differ. These differences are most likely attributed to inaccuracies in characterization of the suspension and mounts properties. The measured as well as experimental car body responses show high magnitude peaks near 2.3 and 6 Hz, which are the vertical mode natural frequencies of car body and bogie. Furthermore, the 6 Hz peak is associated with angular speeds of the wheels with non-uniformities.

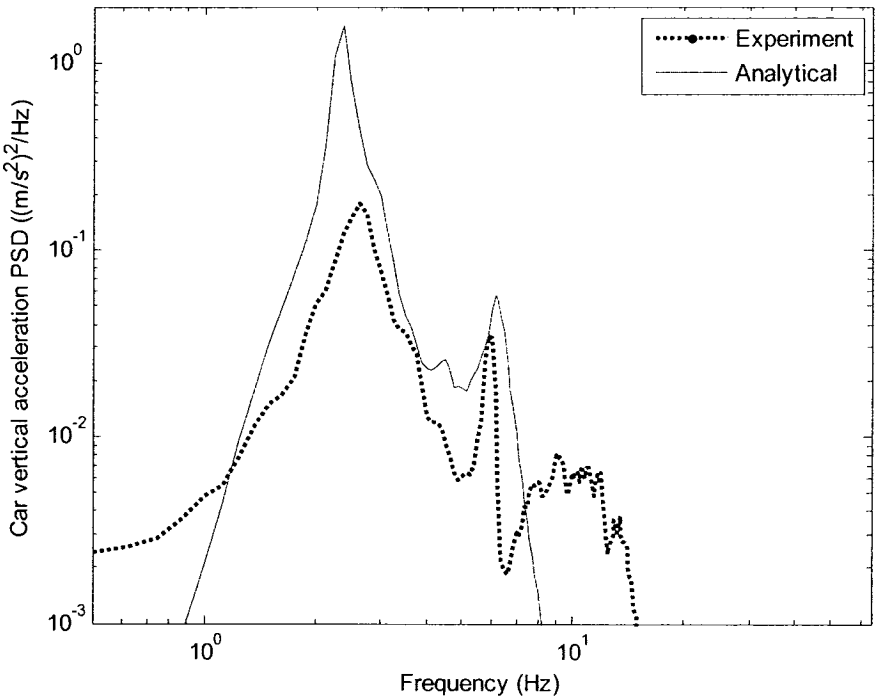

Figure 4.13: Comparison of car body vertical acceleration PSD response with that of measured response.

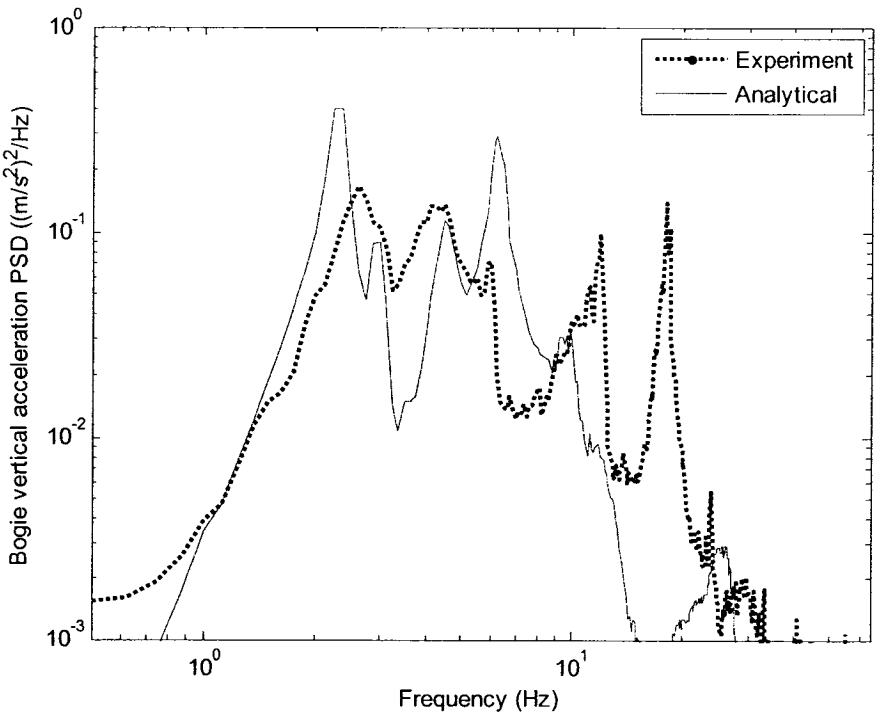

Figure 4.14: Comparison of bogie vertical acceleration PSD response with that of measured response.

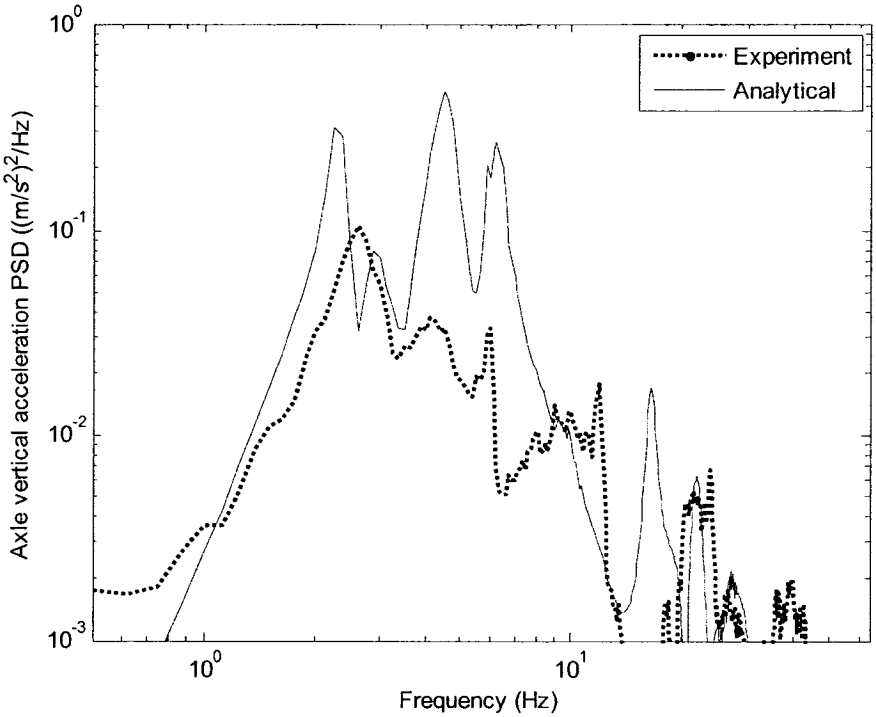

Figure 4.15: Comparison of axle vertical acceleration PSD response with that of measured response.

Figures 4.16 to 4.18 illustrate comparisons between the model and experimental roll acceleration PSD responses of the car body, bogie and axle, respectively. Experimental car and bogie response show increasing magnitude at higher frequencies due to torsional flexibility of the car body frame. The same trend could also be seen in the car pitch response (Fig. 4.19), attributed to frame bending. The model results for car body roll response (Fig. 4.16) reveals peak at 1.04 Hz, corresponding to the resonant frequency of car body roll mode. Peaks near 1, 4.5, 6, 9.6, 16.4 and 26.6 Hz could be observed in both the model and experimental acceleration response PSD of bogie (Fig.4.17) and axle roll (Fig. 4.18), these peaks correspond to car body roll, bogie pitch, bogie vertical, bogie roll, axle roll and axle vertical modes, respectively. Peak magnitude at 6 Hz is larger in

the total acceleration response of the bogie and axle roll when compared to response due to track roughness alone (Fig. 4.6), suggesting the presence of response due to tire non-uniformity and mass unbalance.

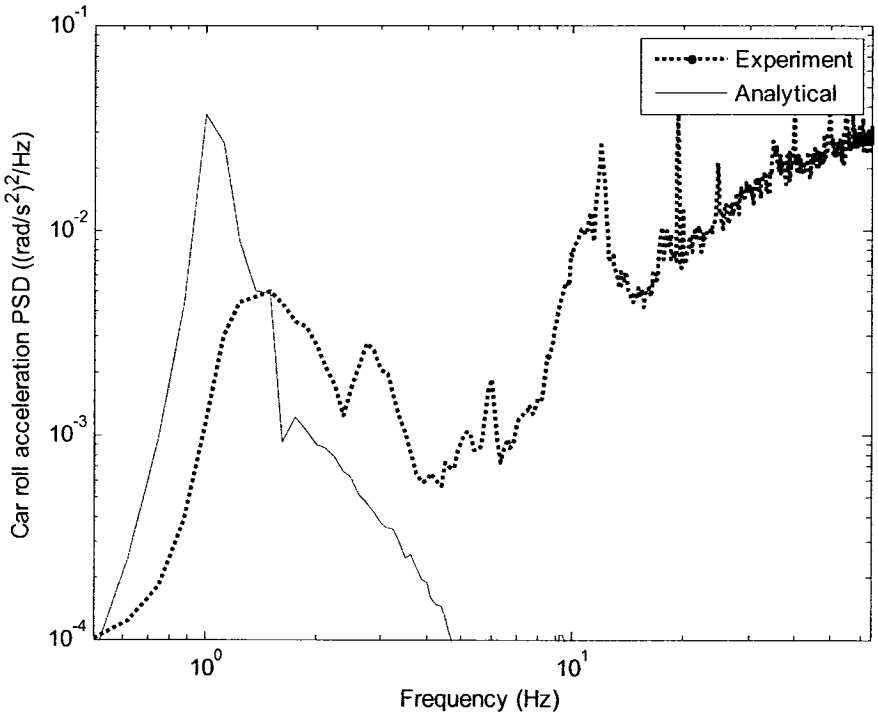

Figure 4.16: Comparison of car body roll acceleration PSD response with that of measured response.

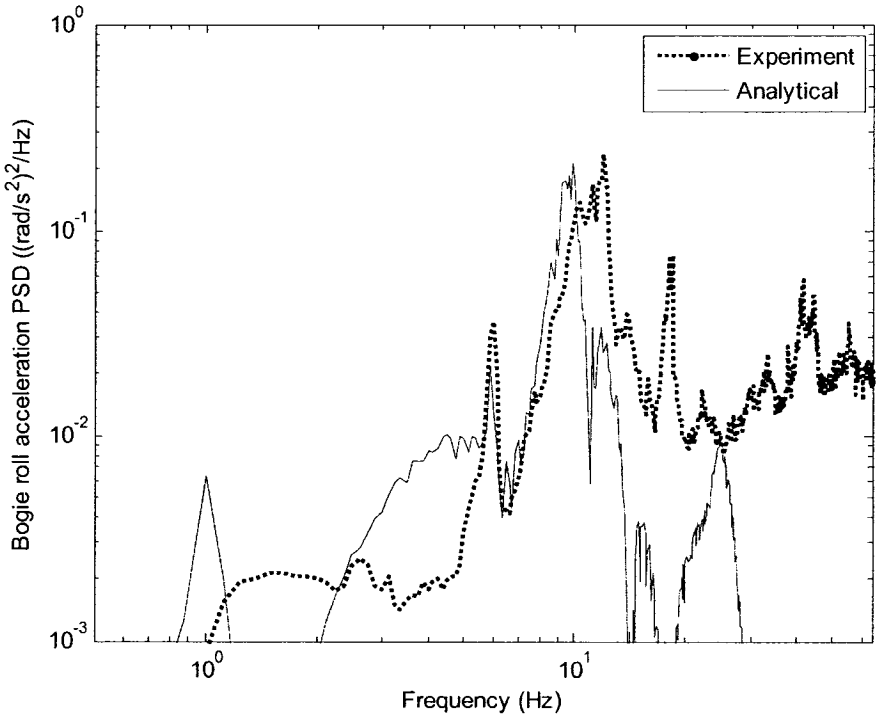

Figure 4.17: Comparison of bogie roll acceleration PSD response with that of measured response.

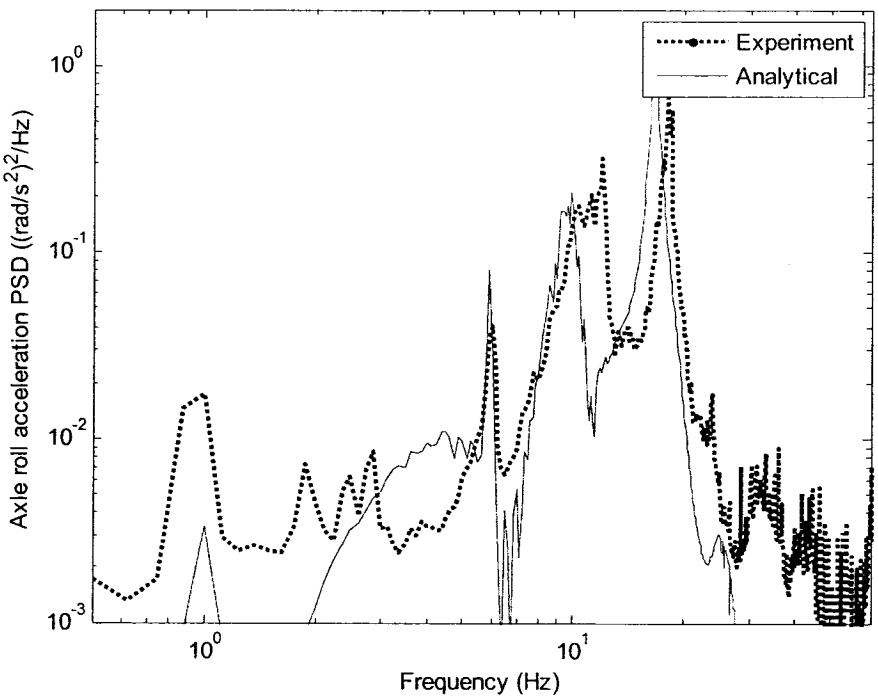

Figure 4.18: Comparison of axle roll acceleration PSD response with that of measured response.

Figures 4.19 and 4.20 illustrate comparison of model and experimental pitch response of the car body and bogie. Car body pitch model response peaks near 2.3, 3, 4.5 and 6.7 Hz, corresponding to car vertical, car pitch, bogie pitch and bogie vertical modes, respectively, while the experimental response reveals higher magnitude peaks at 4.5, 6 and 10 Hz. Comparison between model and analytical pitch response of the bogie is illustrated in Fig. 4.20. The analytical response shows major response peaks at 4.5 and 6.2 Hz, corresponding to bogie pitch and bogie bounce modes respectively. Peaks of relatively smaller magnitude when compared with experimental results could also be observed near 16 and 21 Hz, corresponding to axle roll and bounce modes, respectively.

Finally, it could be concluded that the acceleration responses evaluated while employing the ride dynamic mathematical model of the metro car developed in chapter 2, represents the experimental responses in the 1-20 Hz frequency range. This model could be effectively employed in studying the effect of various operating and design parameters on the response characteristics of the metro vehicle in the 1-20 Hz frequency range, this frequency range is of considerable importance in the ride vibration analysis.

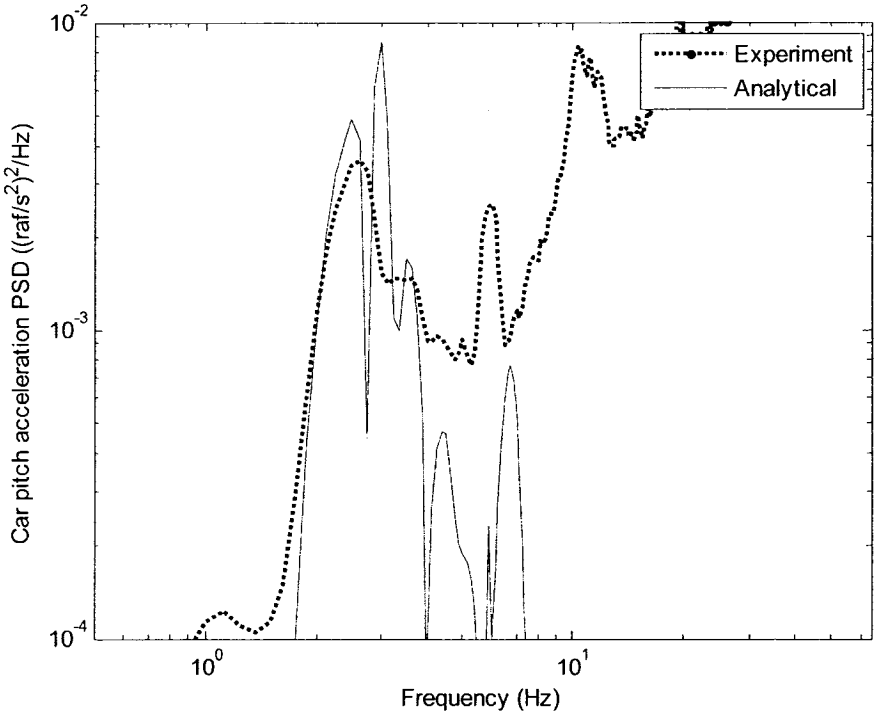

Figure 4.19: Car pitch response at location of measurement.

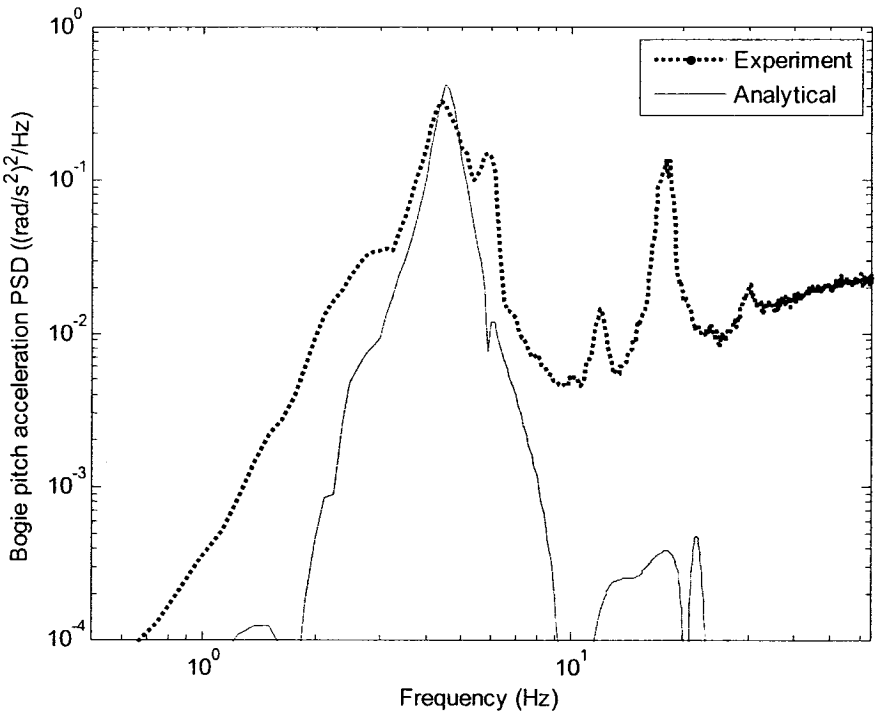

Figure 4.20: Bogie pitch response at location of measurement.

4.7 SUMMARY

In this chapter, attempts were made to validate the three dimensional ride dynamic mathematical model. Eigenvalue analysis was performed to obtain natural frequencies and their corresponding deflection modes. Furthermore, acceleration responses of the vehicle sub-systems were determined due to each excitation force acting individually. Finally, the total response of the metro car is evaluated due to combined effect of track roughness and tire defects and validation with experimental response is performed. Once the ride dynamic mathematical model is validated with the experimental results, effect of various design parameters on the ride quality of the metro car could be studied. In the following chapter, effect of various design and operational parameters on the ride quality of the metro car, as experienced by the operator is studied.

5 PARAMETRIC SENSITIVITY ANALYSIS

5.1 INTRODUCTION

The studies on ride vibration of metro or subway cars have been mostly limited to analyses of the field-measured acceleration data. Such data permit for exposure assessment and the influence of operating factors, such as speed and passenger load. Only minimal information, however, could be gained on the influences of various design factors. In this chapter, effect of various operational and design parameters on the ride quality of the metro car, as experienced by the operator, is studied. For performing the parametric sensitivity analysis, a mathematical model of the metro car was developed in chapter 2 and the validation of this mathematical model with the experimental data (as identified in chapter 3) was performed in chapter 4.

The ride acceleration responses of the metro car are strongly related to various design and operating parameters. The vehicle design parameters selected for the parametric study include: inertial properties of the vehicle constituents namely car body, bogie and axle and the stiffness and damping properties of the suspension system and tires. The selected operating parameters include: passenger load and operating speed. The self exciting sources of vibration, arising from wheel unbalance and wheel non-uniformity would fall within the operating parameters. The effects of these parameters are expected to be coupled with other operating factors, such as loads, speed and track roughness. The validated three dimensional metro vehicle model is utilized to investigate the sensitivity of performance measures to variations in considered parameters. The performance measures employed in the study are selected by keeping focus on the ride

quality of the vehicle experienced by the vehicle operator. The frequency weighting filters proposed in ISO 2631-1 (1997) are applied to determine the overall weighted rms bounce, roll and pitch accelerations to assess the ride quality of the vehicle.

5.2 PERFORMANCE MEASURES

Performance measures are employed in parametric sensitivity analysis to assess the effect of different operational and design parameters. Selection of performance measures depends on the focus of the study. In the present dissertation, focus is on ride vibration analysis of the metro vehicle at the operator location. The performance measures employed in the study is the ride quality of the vehicle, as experienced by the operator. Three performance measures employed are: overall rms acceleration, weighted rms acceleration and band rms acceleration.

5.2.1 Overall rms acceleration

The operator comfort is governed by ride quality, which in turn depends on the track condition and suspension performance. The seat is also a very important element in a ride analysis since the flexibility of the seat isolates the driver from high-frequency vertical vibrations. The seats used in metro vehicle are unsuspended and therefore, for simplicity this study uses the car body floor at operator seat rather than the driver/seat interface for the evaluation of ride performance. The response of the vehicle is obtained based on car body vertical, roll and pitch motions. The overall rms accelerations due to vertical $\left(\ddot{z}_{rms}\right)$ roll $\left(\ddot{\theta}_{rms}\right)$ and pitch $\left(\ddot{\phi}_{rms}\right)$ vibration of the metro car can be computed from equations 5.1, 5.2 and 5.3, respectively.

$$\ddot{z}_{rms} = \sqrt{\int_{0.5}^{20} S_z(f)\,df} \qquad (5.1)$$

$$\ddot{\theta}_{rms} = \sqrt{\int_{0.5}^{20} S_\theta(f)\,df} \qquad (5.2)$$

$$\ddot{\phi}_{rms} = \sqrt{\int_{0.5}^{20} S_\phi(f)\,df} \qquad (5.3)$$

where $S_z(f), S_\theta(f)$ and $S_\phi(f)$ are power spectral densities of acceleration in vertical, roll and pitch directions at operator level.

5.2.2 Weighted rms acceleration

The ride performance of a vehicle is assessed in terms of magnitude and frequency contents of vibration transmitted to the driver or passenger seat. The frequency, to which a human driver is most fatigue sensitive for the horizontal and vertical vibrations, lies in the range from 1 to 2 Hz and 4 to 8 Hz, respectively. The human sensitivity to rotational vibration is mostly in 0.5 to 1.5 Hz frequency range [53]. The international standard (ISO 2631-1) has outlined a procedure to assess the human exposure to whole-body ride vibrations in terms of overall frequency-weighted rms acceleration at the driver/passenger seat interface [53]. The standard defines frequency-weighting W_k for vertical vibration in the 0.5-80 Hz frequency range, and W_e for the roll/pitch vibration in the 0.1-80 Hz frequency range. The frequency-weighted rms accelerations can be found using equations 5.4, 5.5 and 5.6, respectively.

$$\ddot{z}_{w,rms} = \sqrt{\int_{0.5}^{20} \{S_z(f) \times W_k(f)\}\,df} \qquad (5.4)$$

$$\ddot{\theta}_{w,rms} = \sqrt{\int_{0.5}^{20} \{S_\theta(f) \times W_e(f)\} df} \tag{5.5}$$

$$\ddot{\phi}_{w,rms} = \sqrt{\int_{0.5}^{20} \{S_\phi(f) \times W_e(f)\} df} \tag{5.6}$$

Ride quality is affected by low frequency vibrations and therefore, rms accelerations are found in the frequency band of 0.5-20 Hz.

The frequency weighting function is defined from the combination of a band limiting transfer function, $H_h(p).H_l(p)$ (i.e. high-pass and low-pass filters), and the weighting transfer function, $H_t(p).H_s(p)$. The total frequency weighting function is obtained by [53]:

$$H(p) = H_h(p).H_l(p).H_t(p).H_s(p) \tag{5.7}$$

where $H_h(p)$ is high pass filter function and expressed as:

$$|H_h(p)| = \left| \frac{1}{1 + \sqrt{2}\omega_1 / p + (\omega_1 / p)^2} \right| \tag{5.8}$$

in which, $\omega_1 = 2\pi f_1$, $p = j2\pi f$ and f_1 is the corner frequency (intersection of asymptotes).

$H_l(p)$ is low pass transfer filter function and expressed as:

$$|H_l(p)| = \left| \frac{1}{1 + \sqrt{2}p / \omega_2 + (p / \omega_2)^2} \right| \tag{5.9}$$

in which, $\omega_2 = 2\pi f_2$, and f_2= corner frequency.

$H_t(p)$ is acceleration-velocity transfer function and expressed as:

$$H_t(p) = \left| \frac{1 + p / \omega_3}{1 + p/(Q_4\omega_4) + (p / \omega_4)^2} \right| \tag{5.10}$$

in which, $\omega_3 = 2\pi f_3$, and $\omega_4 = 2\pi f_4$.

$H_s(p)$ is upward step transfer function (steepness approximately 6 dB per octave, proportional to jerk), given by:

$$H_s(p) = \left| \frac{1 + p/(Q_5\omega_5) + (p/\omega_5)^2}{1 + p/(Q_5\omega_6) + (p/\omega_6)^2} \left(\frac{\omega_5}{\omega_6} \right)^2 \right| \tag{5.11}$$

in which, $\omega_5 = 2\pi f_5$, and $\omega_6 = 2\pi f_6$.

The various coefficients used in the transfer functions are listed in the Table 5.1. The shapes of the individual transfer functions are plotted in appendix A, along with the composite transfer function in Eq. (5.7)

Table 5.1: Coefficients of transfer functions of the frequency weightings [53]

Weighting	**Band-limiting**		**Acceleration-velocity transition**			**Upward step**			
	f_1 (*Hz*)	f_2 (*Hz*)	f_3 (*Hz*)	f_4 (*Hz*)	Q_4	f_5 (*Hz*)	Q_5	f_6 (*Hz*)	Q_6
W_k	0.4	100	12.5	12.5	0.63	2.37	0.91	3.35	0.91
W_e	0.4	100	1.0	1.0	0.63	∞	-	∞	-

5.2.3 Band rms acceleration

In view of ride comfort due to vertical vibration, frequency band of 4-8 Hz is of importance. Also, in the experimental study [1], importance of vibration at 6 Hz is stated; therefore, a third performance measure employed in this study is frequency spectrum which is actually rms acceleration in the frequency band of 4-8 Hz. It is particularly useful in assessing operator-friendliness of the metro vehicle due to vertical vibration. It

is evaluated using equations 5.1-5.3 with the upper and lower limits of integration being 8 and 4 Hz, respectively.

5.3 PARAMETERS

In most of the literature available on ride quality analysis of metro vehicles only effect of operational parameters are studied [61]. In the following study two types of parameters are used namely, operational parameters and design parameters. While studying the effect of a particular parameter all other parameters are kept constant. The operational parameters studied are vehicle forward speed and passenger load. During the study of operational parameters all design parameters are kept constant (nominal value as given in Table. 4.1). The design parameters studied in the study are inertial properties of car, bogie and axle along with stiffness and damping properties of suspension elements. Throughout the study of affects of design parameters, operational parameters are kept constant ($v = 60$ km/h, which is the normal speed at which metro train operates and 100% load). Natural frequencies of the vehicle are directly related to the design parameters and therefore, change in design parameters is likely to bring changes in natural frequencies of the vehicle. Three configurations of each design parameter are used. One of the configurations is with nominal values of design parameters used for validation of the model in chapter 4, other two configurations used are 80% of nominal value and 120% of nominal value.

5.3.1 Speed

Effect of vehicle speed on the performance measures is illustrated in Fig. 5.1 (a, b and c). The speeds considered are 45 km/h, 60km/h and 75km/h, which fall in the

nominal operating speed range of the metro car. Vehicle speed directly affects mass-unbalance force due to tire non-uniformity. Figure 5.1 (a) illustrates effect of vehicle speed on the overall rms acceleration at operator level in vertical, roll and pitch directions. With increasing speed overall rms acceleration must also increase due to increase in unbalance force. Vertical rms acceleration at 45 km/h is more than that at 60 km/h due to the fact that at 45 km/hr, tire angular speed is near 4.5 Hz which corresponds to the resonant frequency of bogie pitch mode. Car vertical mode is strongly coupled with bogie pitch mode therefore we see higher rms value at 45 km/h. Roll rms acceleration decreases with increasing speed while pitch rms acceleration increases. Figure 5.1 (b) illustrates effect of speed on weighted rms acceleration; here magnitude of acceleration at 75 km/h is more due to weightings used which enhance the magnitude in 4-8 Hz frequency range. Figure 5.1 (c) shows band limited rms acceleration. Vertical response shows same trend as in overall rms acceleration while roll response shows opposite trend of what is shown in Fig. 5.1(a). This is due to the fact that although responses in 4.5-7 Hz frequency range increases with speed, the overall response decreases due to decrease in response at other frequency components.

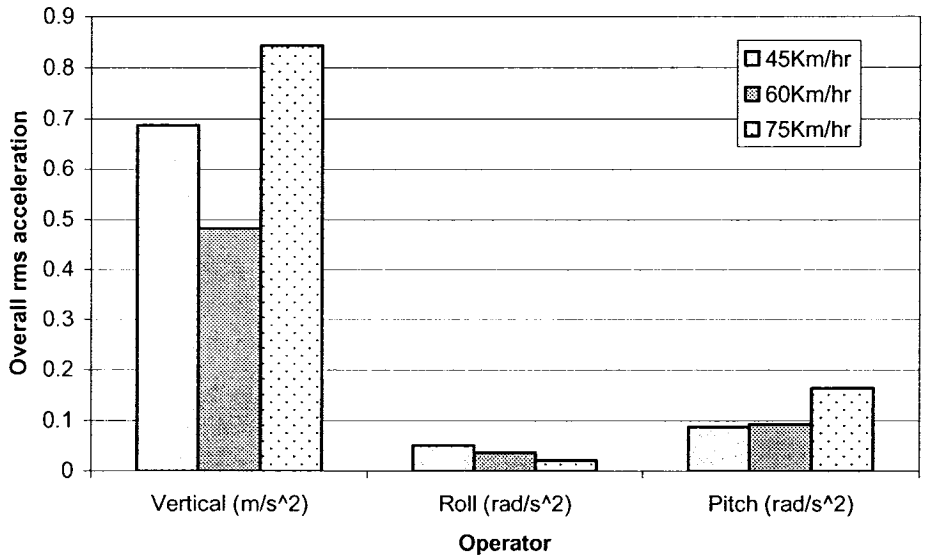
0.9
0.8
0.7
0.6
0.5
0.4
0.3
0.2
0.1
0
Overall rms acceleration
45Km/hr
60Km/hr
75Km/hr
Vertical (m/s^2)
Roll (rad/s^2)
Pitch (rad/s^2)
Operator

(a)

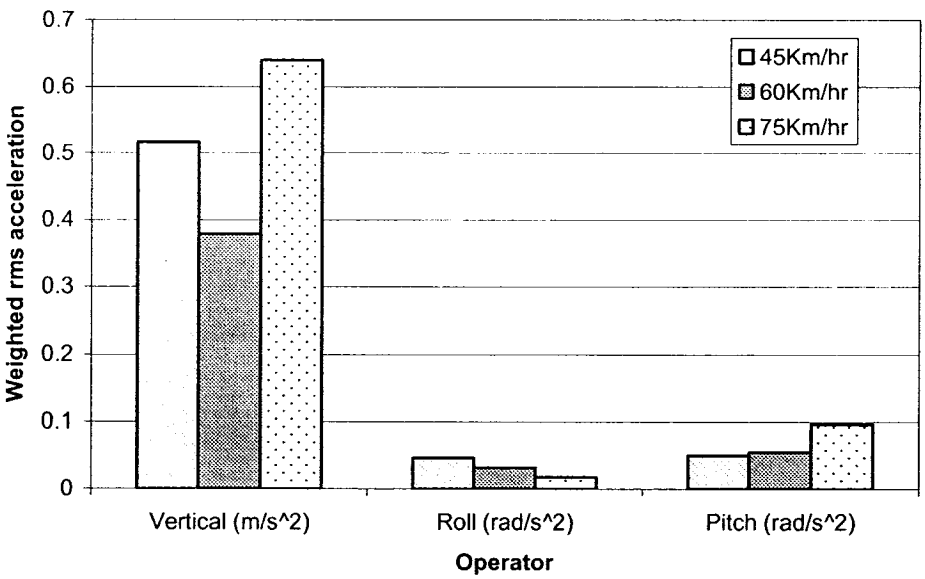
0.7
0.6
0.5
0.4
0.3
0.2
0.1
0
Weighted rms acceleration
45Km/hr
60Km/hr
75Km/hr
Vertical (m/s^2)
Roll (rad/s^2)
Pitch (rad/s^2)
Operator

(b)

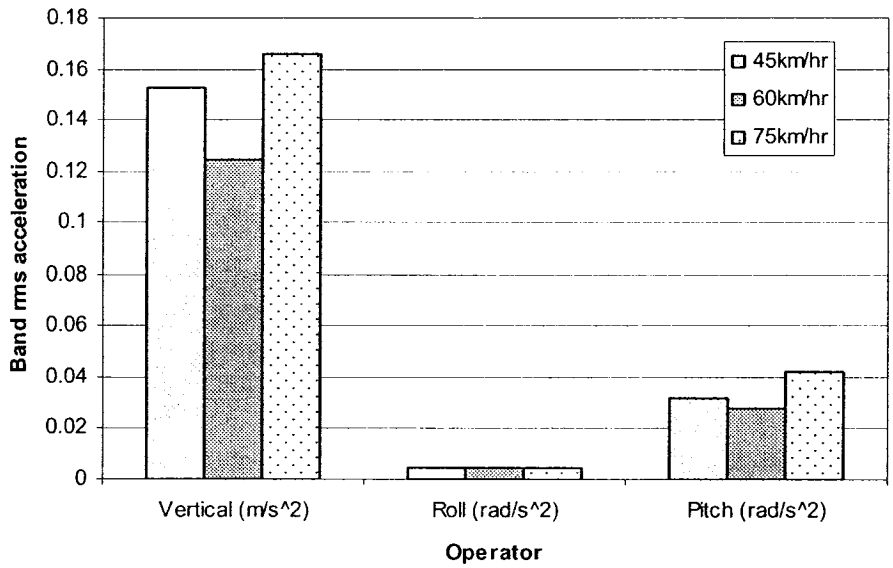

(c)

Figure 5.1: Influence of speed: (a) Overall rms acceleration, (b) weighted rms acceleration and (c) band rms acceleration (100% load).

5.3.2 Passenger load

Effect of passenger load on the performance measures is illustrated in Fig. 5.2(a, b and c). For analyzing the affect of passenger load, vehicle forward speed is kept constant at the operational speed of 60 km/h. The loading conditions are varied from the operational condition of full load (100%) to empty (0%) and half load (50%). Due to change in passenger load, natural frequencies of the car modes are affected. As we increase passenger load, natural frequency of car in vertical mode decreases, although due to progressive hardening of spring, increase in load is compensated by increased spring constant; but for this study linear properties of suspension are considered. As stated, with increasing load natural frequency of car vertical mode decreases and due to decreasing acceleration magnitude of the track roughness PSD below 3Hz, response also

starts decreasing. Same trend is evident in weighted and band rms acceleration. Roll and pitch responses of the car body have little effect due to change in loading conditions, as evident from similar magnitude of overall, weighted and band rms accelerations.

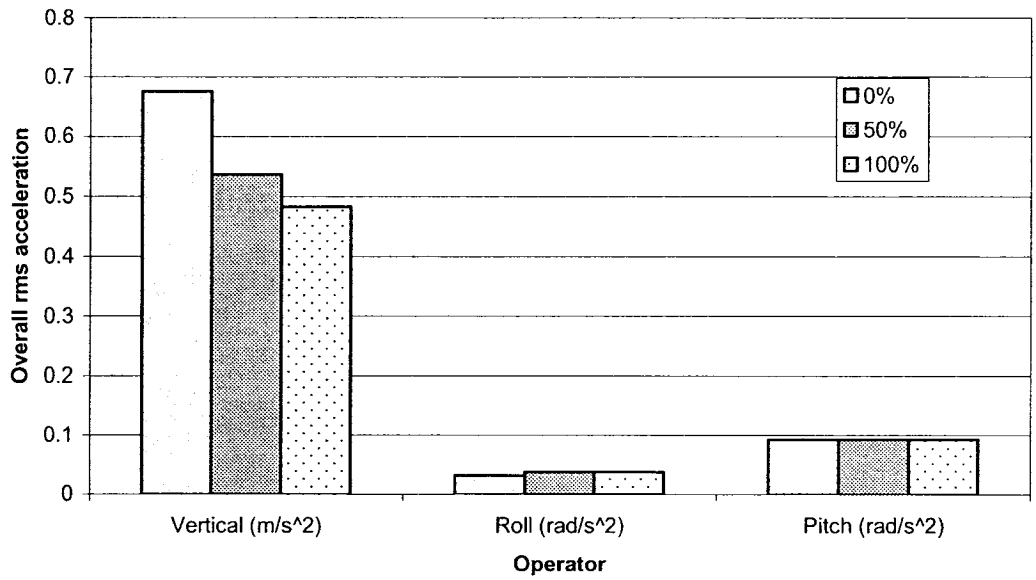

(a)

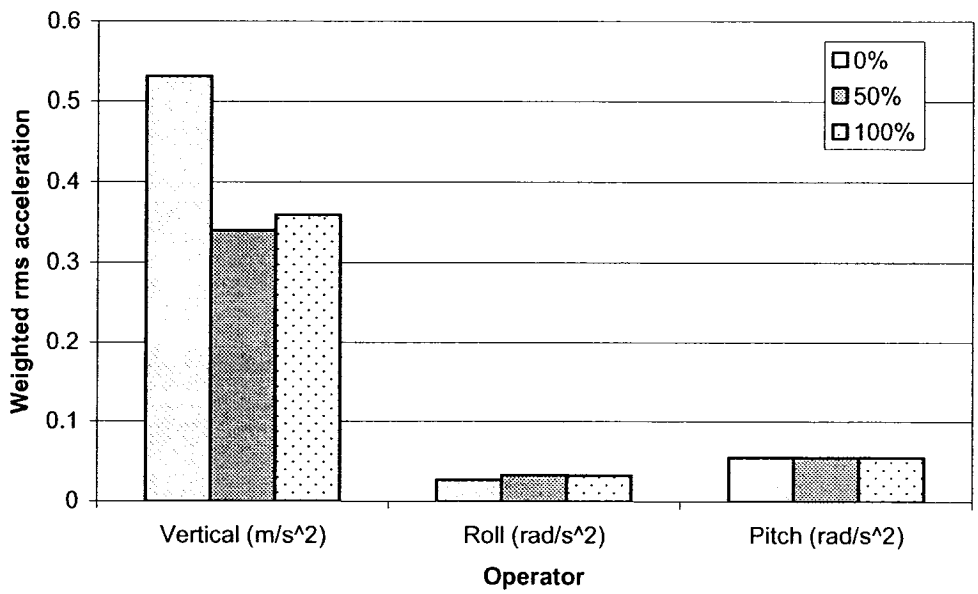

(b)

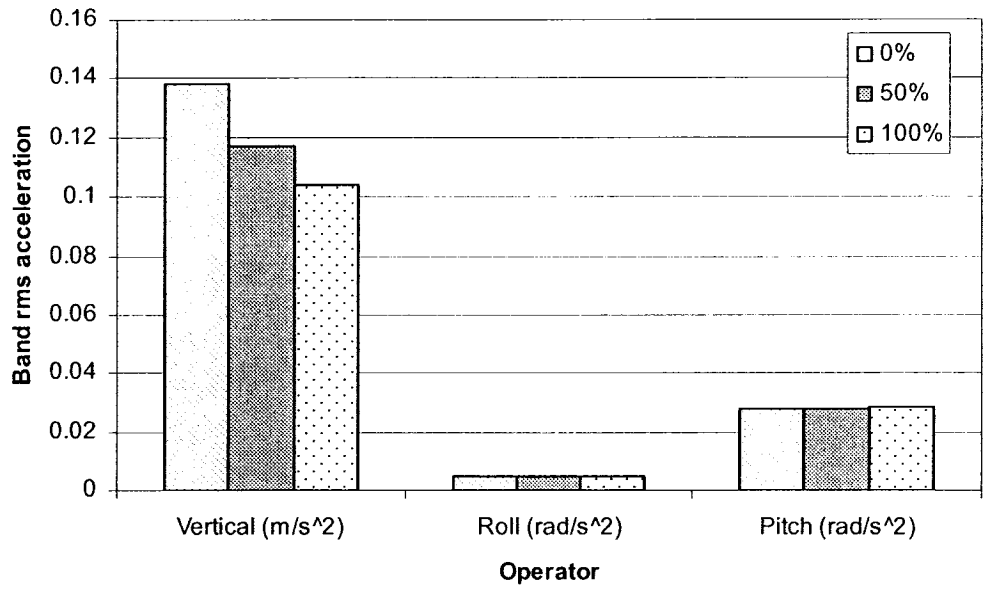

(c)

Figure 5.2: Influence of passenger load: (a) Overall rms acceleration, (b) weighted rms acceleration and (c) band rms acceleration. ($v = 60$ km/h, 100% load)

5.3.3 Car mass

Effect of car mass on the ride quality of the metro vehicle is illustrated in Fig. 5.3(a, b and c). Effect of car mass is similar to that of passenger load. Overall effect of increasing car mass is to reduce natural frequency of car vertical mode. The overall rms acceleration illustrated in Fig. 5.3(a) suggests 37% increase in vertical unweighted rms acceleration due to 20% decrease in car mass, while 11% decrease due to 20% increase in car mass. Roll rms acceleration (unweighted) decreases to 26% and 6%, respectively, due to both 20% increase and 20% decrease of car mass from reference value, while pitch rms acceleration seems largely unaffected by changes in car mass. The weighted rms acceleration (Fig. 5.3(b)) reveals similar trends and magnitudes of vertical, roll and pitch

rms accelerations as demonstrated by overall rms acceleration (Fig. 5.3(a)). The band rms acceleration (Fig. 5.3(c)) illustrates affect of car mass on the car body acceleration response in the 4-8 Hz frequency range. Vertical and pitch accelerations reveal similar trend, while roll acceleration shows no change which could be attributed to the fact that car roll response occurs at frequencies below 3 Hz.

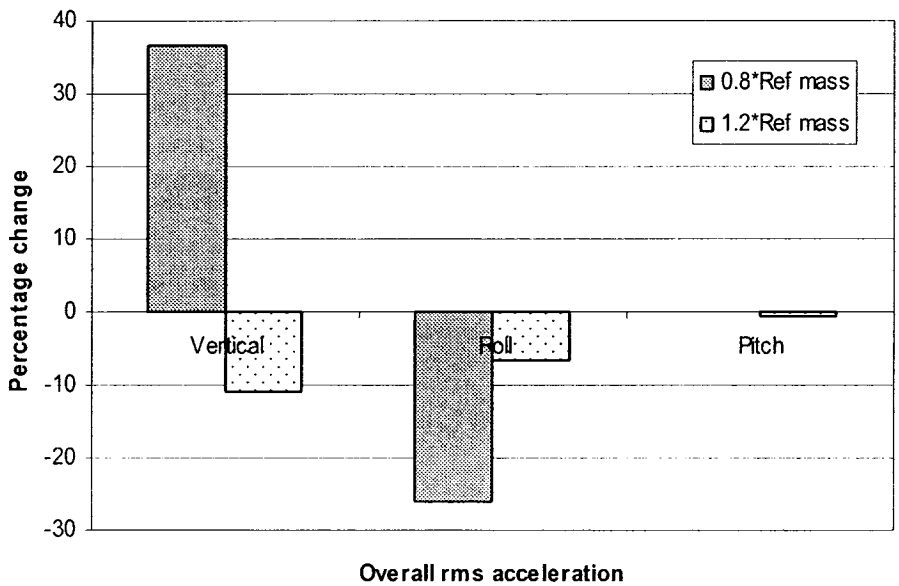

(a)

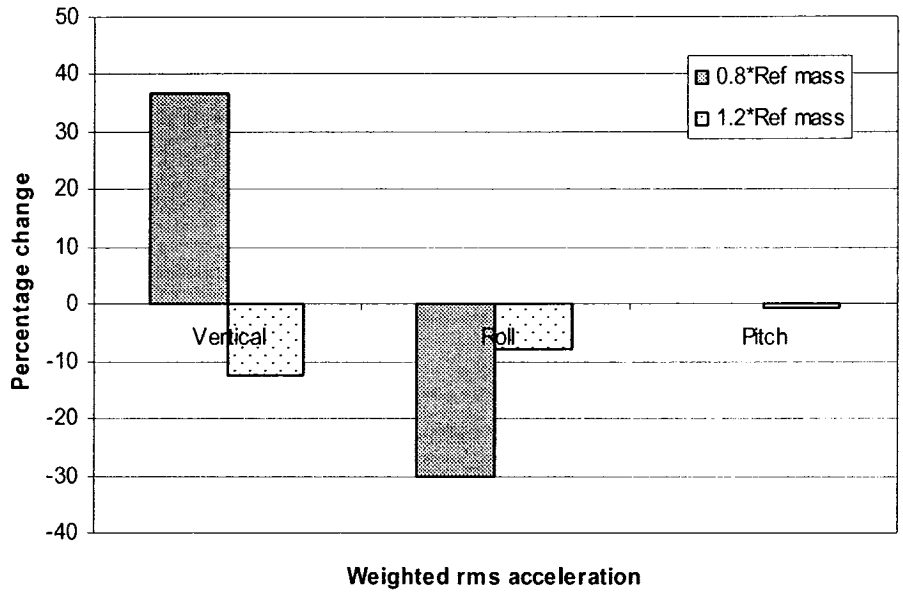

(b)

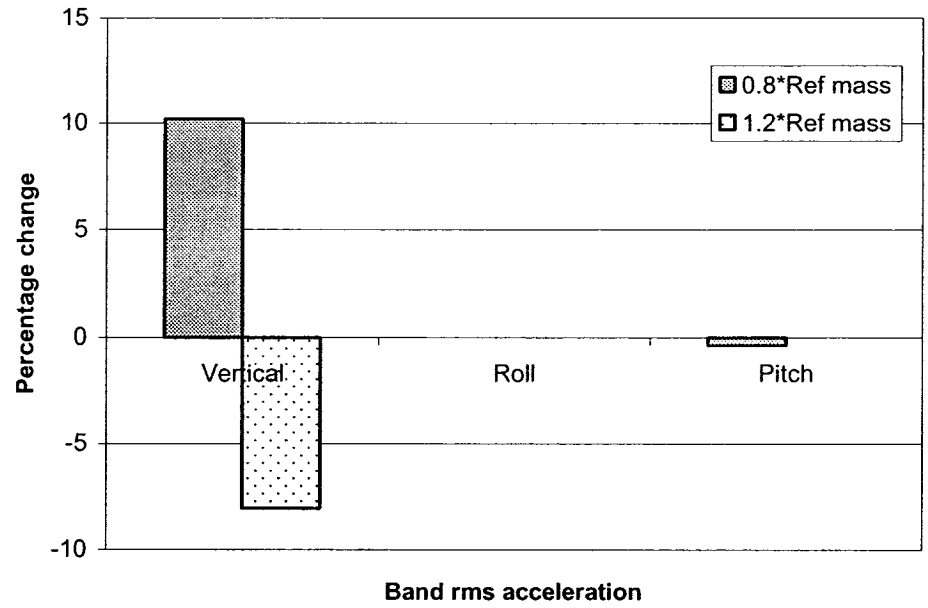

(c)

Figure 5.3: Influence of car mass: (a) Overall rms acceleration, (b) weighted rms acceleration and (c) band rms acceleration ($v = 60$ km/h, 100% load).

5.3.4 Car roll mass moment of inertia

Figure 5.4(a, b and c) illustrate effect of car roll mass moment of moment of inertia. Car roll moment of inertia affects the car roll frequency (1.04 Hz). With increasing inertia, natural frequency reduces to 0.95 Hz at 120% of reference car roll inertia. Although the vertical and pitch response mostly remain unaffected, the roll response decreases with either increase or decrease in car roll inertia. Overall roll rms acceleration (Fig. 5.4(a)) decreases to 33% and 35% due to 20% decrease and 20% increase in car roll inertia, respectively. Weighted rms acceleration (Fig. 5.4(b)) reveals increase of up to 5% in magnitude of vertical rms acceleration due to either decrease or increase of 20% in car roll moment of inertia. Roll rms acceleration decreases to 36% due to 20% change in car roll moment of inertia. Figures 5.4(c) shows very small change in vertical and pitch response, which suggests that car roll mass moment of inertia changes do not affect vertical and pitch responses in the frequency range of 4-8 Hz, but due to 20% increase there is a decrease of 16% in roll rms acceleration in frequency range of 4-7 Hz.

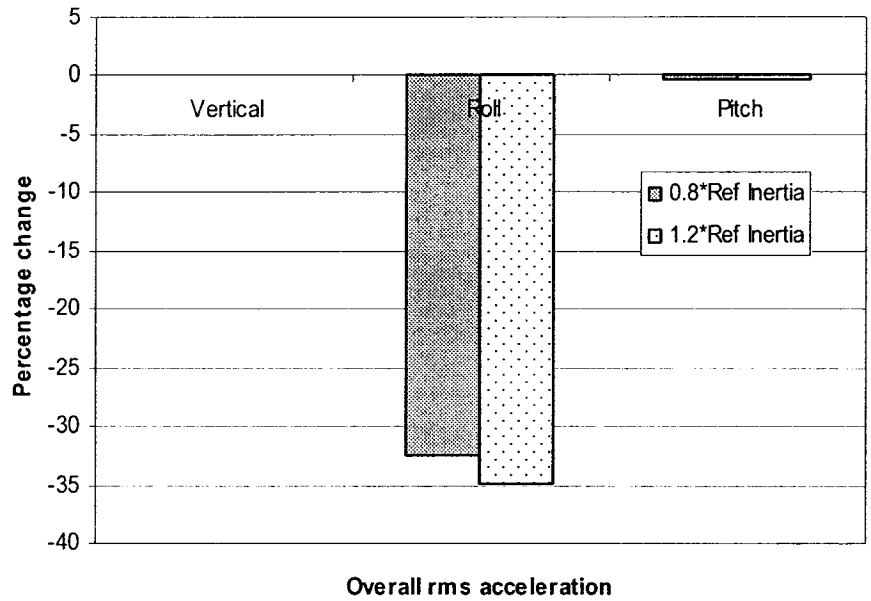
5
0
-5
-10
-15
-20
-25
-30
-35
-40
Vertical
Roll
Pitch
0.8*Ref Inertia
1.2*Ref Inertia
Percentage change
Overall rms acceleration

(a)

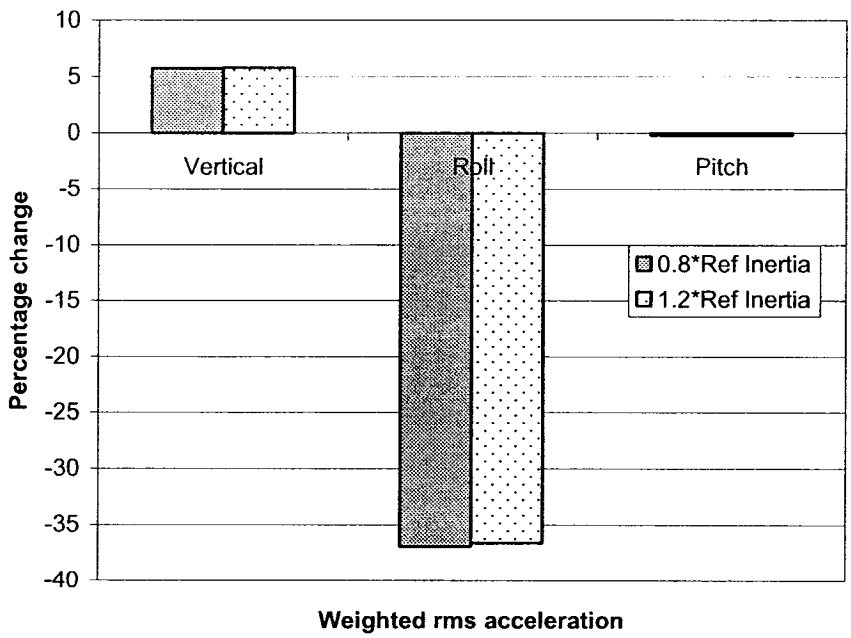
10
5
0
-5
-10
-15
-20
-25
-30
-35
-40
Vertical
Roll
Pitch
0.8*Ref Inertia
1.2*Ref Inertia
Percentage change
Weighted rms acceleration

(b)

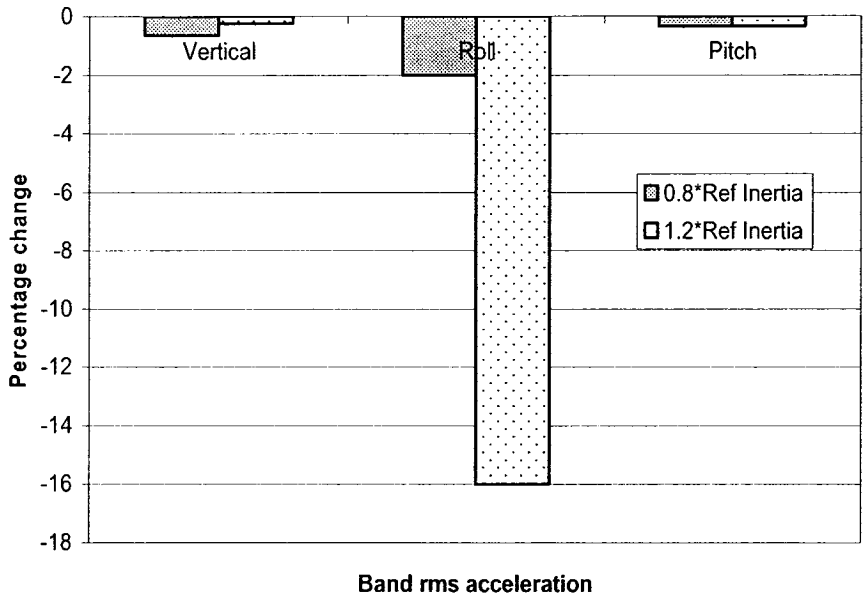

(c)

Figure 5.4: Influence of car roll mass moment of inertia: (a) Overall rms acceleration, (b) weighted rms acceleration and (c) band rms acceleration ($v = 60$ km/h, 100% load).

5.3.5 Car pitch mass moment of inertia

Effect of car pitch mass moment of inertia on the performance measures is shown graphically in Fig. 5.5(a, b and c). Car pitch inertia affects natural frequency of car pitch and bogie bounce modes. Figure 5.5(a, b) illustrates overall and weighted rms acceleration at operator's level. Vertical and pitch rms acceleration shows increase due to both increase and decrease in pitch inertia. Roll acceleration shows a decrease due to pitch inertia change and this decrease is more due to 80% of reference inertia. In the frequency range of 4-8 Hz as shown in Fig. 5.5(c) decrease of up to 3% in vertical and 11.6% in pitch acceleration due to 20% increase in car pitch inertia.

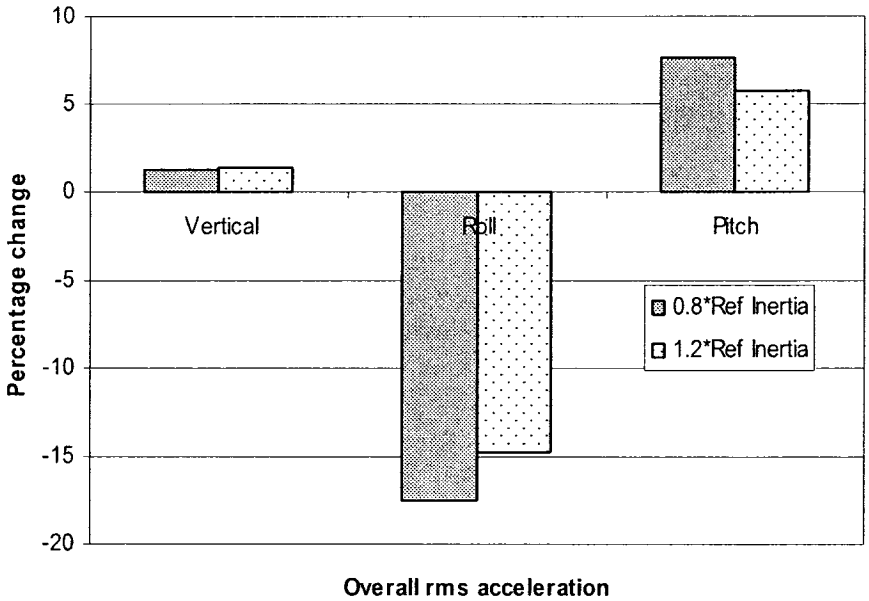
10
5
0
-5
-10
-15
-20
Percentage change
Vertical
Roll
Pitch
0.8*Ref Inertia
1.2*Ref Inertia
Overall rms acceleration

(a)

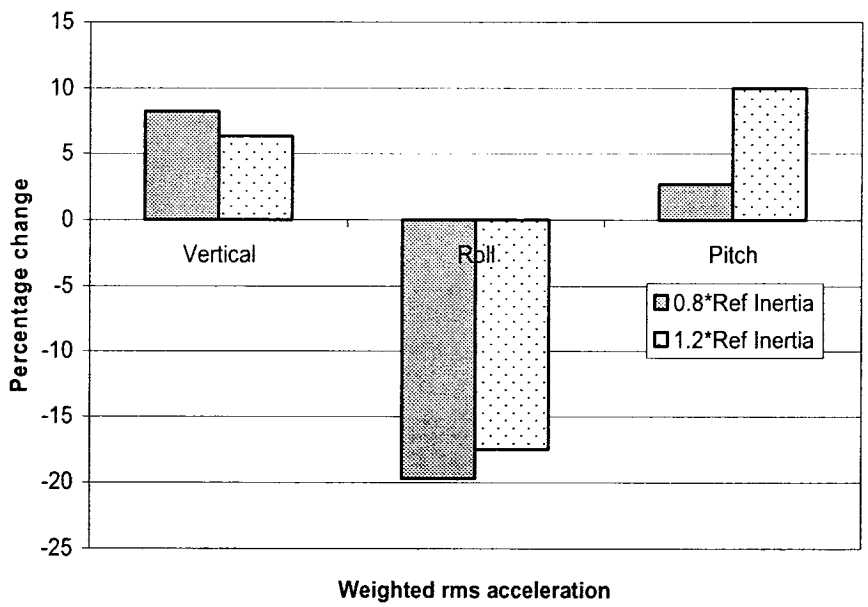
15
10
5
0
-5
-10
-15
-20
-25
Percentage change
Vertical
Roll
Pitch
0.8*Ref Inertia
1.2*Ref Inertia
Weighted rms acceleration

(b)

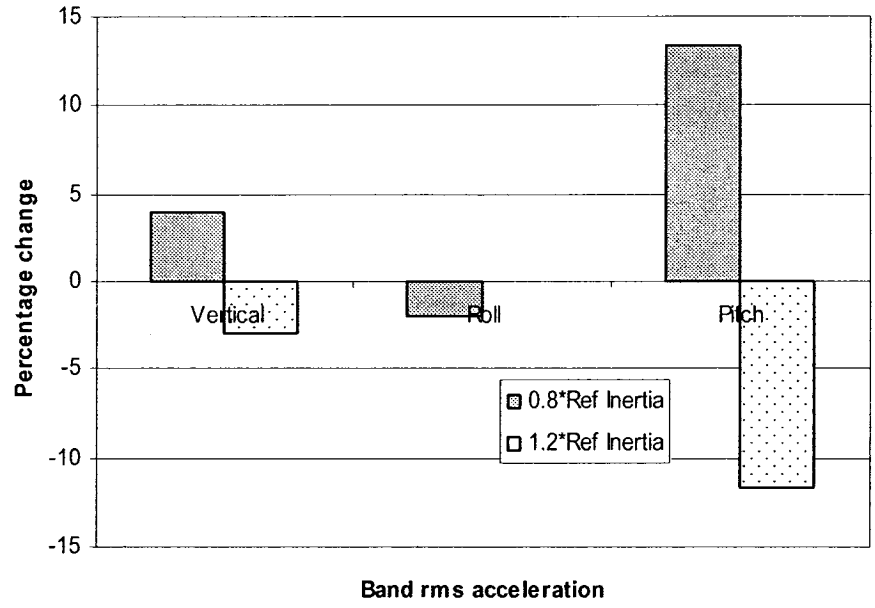

(c)

Figure 5.5: Influence of car mass moment of pitch inertia: (a) Overall rms acceleration, (b) weighted rms acceleration and (c) band rms acceleration ($v = 60$ km/h, 100% load).

5.3.6 Elastomeric spring stiffness

Secondary suspension of the metro vehicle consists of four elastomeric springs between car and bogie as described in chapter 2. Due to increase in spring stiffness, natural frequencies of car and bogie modes increase, with prominent increase in bogie and car vertical mode frequencies. Effect of elastomeric spring stiffness is illustrated in Fig. 5.6(a, b and c). Figs. 5.6(a) and 5.6(b) show a similar percentage increase of 16.7% due to 20% increase in spring stiffness and decrease of 11.6% and 12% due to decrease of 20% in stiffness in vertical acceleration. Roll acceleration decreases due to change in stiffness from reference value. Fig. 5.6(c) illustrates band rms acceleration, and here vertical acceleration decreases even due to increase in stiffness which implies that

although overall effect of 20% stiffness increase is an increase in vertical response but in frequency band of 4-8 Hz there is a decrease in vertical acceleration and increase in roll acceleration. Also pitch rms acceleration shows more change in the range 4-7 Hz as compared to overall change as shown in Fig 5.6(a, b).

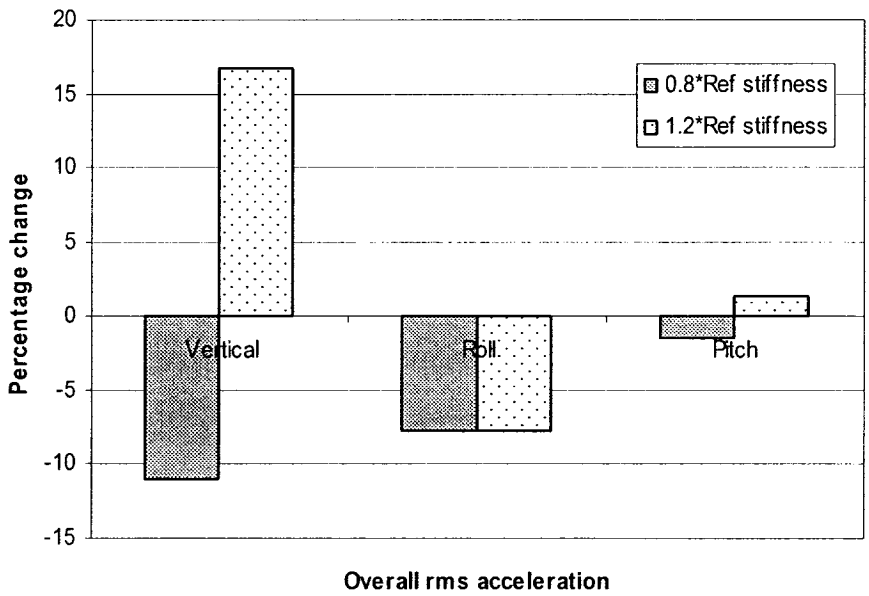

(a).

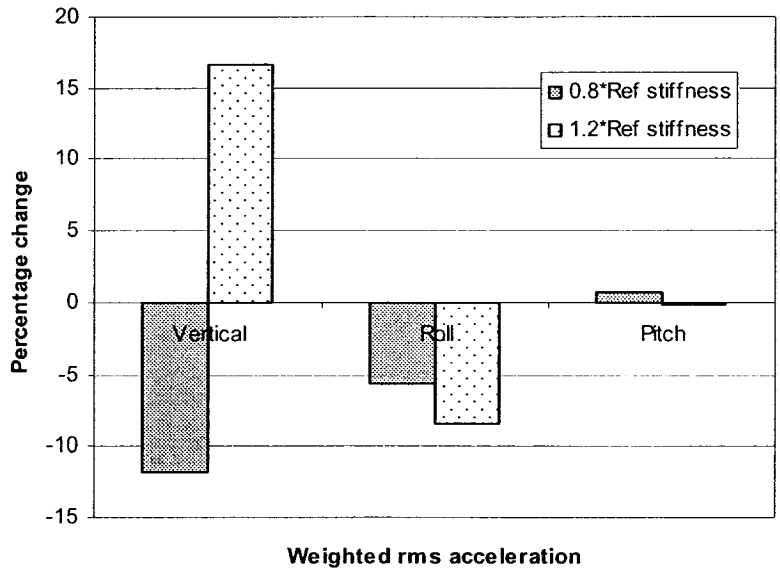

(b)

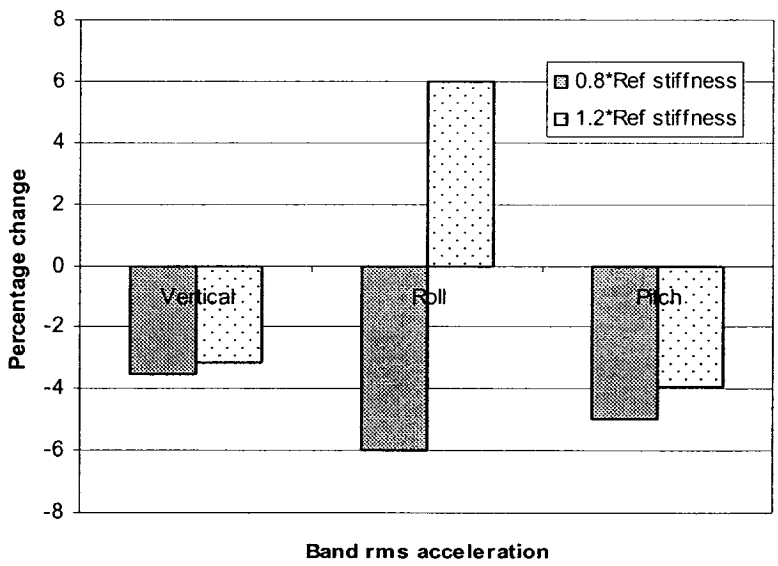

(c)

Figure 5.6: Influence of elastomeric spring stiffness: (a) Overall rms acceleration, (b) weighted rms acceleration and (c) band rms acceleration ($v = 60$ km/h, 100% load).

5.3.7 Elastomeric spring damping

Due to change in damping, damping ratios are affected. Elastomeric spring damping affects damping ratios of car and bogie modes, where the most affected are car and bogie vertical modes among them. Due to damping changes there is minimal affect on natural frequencies. Fig. 5.7(a, b and c) shows effect of elastomeric spring damping on the performance measures for ride quality of metro vehicle. Figs. 5.7(a), 5.7(b) and 5.7(c) show similar trend in all three responses. Due to 20% increase in damping there is decrease in magnitudes of responses. This decrease is more prominent in roll acceleration as compared to vertical and pitch acceleration.

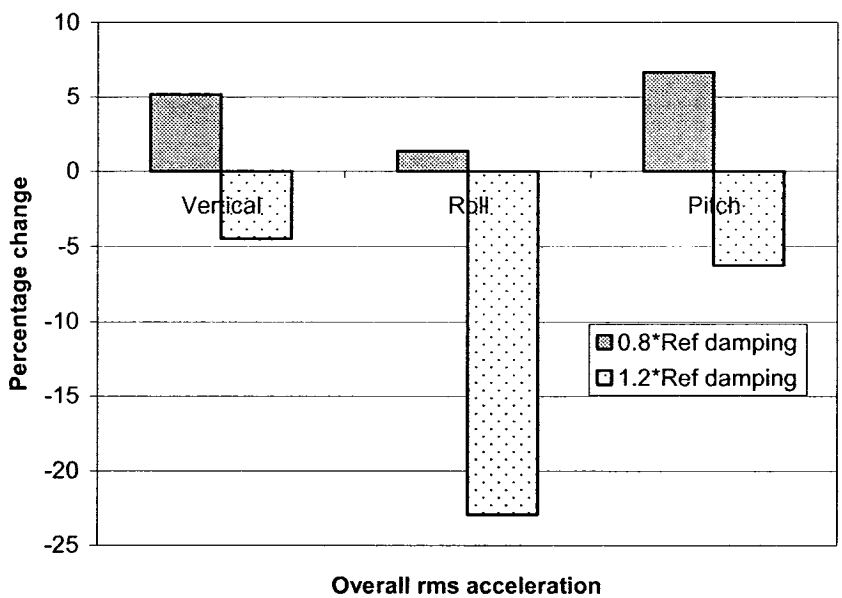

(a)

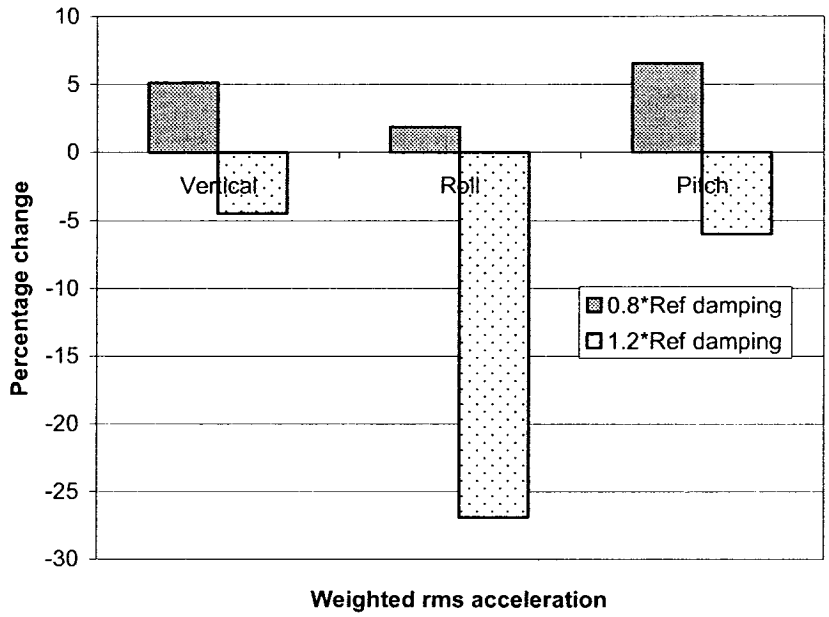

(b)

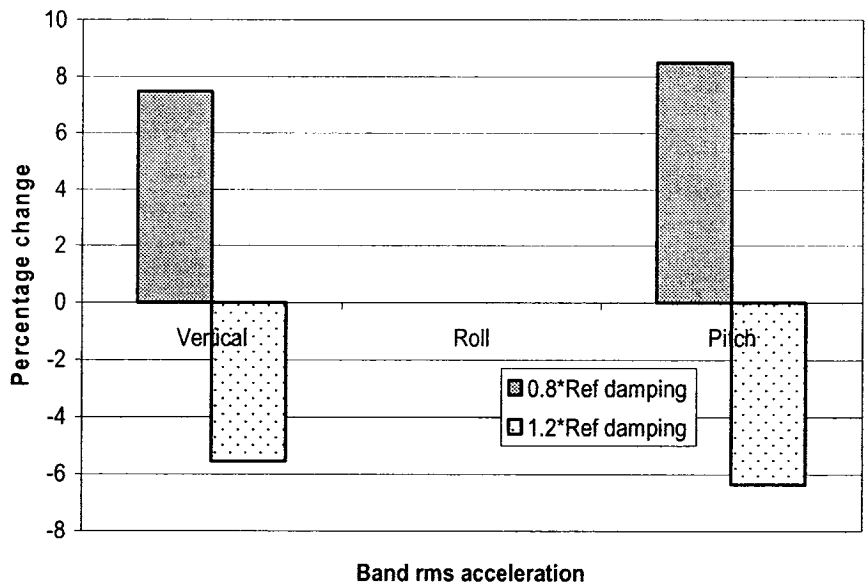

(c)

Figure 5.7: Influence of elastomeric spring damping: (a) Overall rms acceleration, (b) weighted rms acceleration and (c) band rms acceleration ($v = 60$ km/h, 100% load).

5.3.8 Bogie mass

Effect of bogie mass is illustrated in Fig. 5.8(a, b and c). Due to increase in bogie mass there is decrease in bogie vertical and axle vertical natural frequencies. Roll and pitch acceleration show similar respective trends in figure 5.8(a and b), where roll acceleration decrease due to change of bogie mass from reference value and decrease in magnitude is more at 80% of reference value. Pitch overall and weighted acceleration increases due to increase in bogie mass. Overall vertical acceleration increases due to decrease in reference value and vice-versa for increase in bogie mass. Figure 5.8(c) shows different trend in vertical direction which could be attributed to the fact that due to 20% increase in bogie mass, bogie vertical mode natural frequency becomes same as tire rolling frequency (near 6 Hz) and therefore vertical acceleration increases in the frequency range of 4-8 Hz.

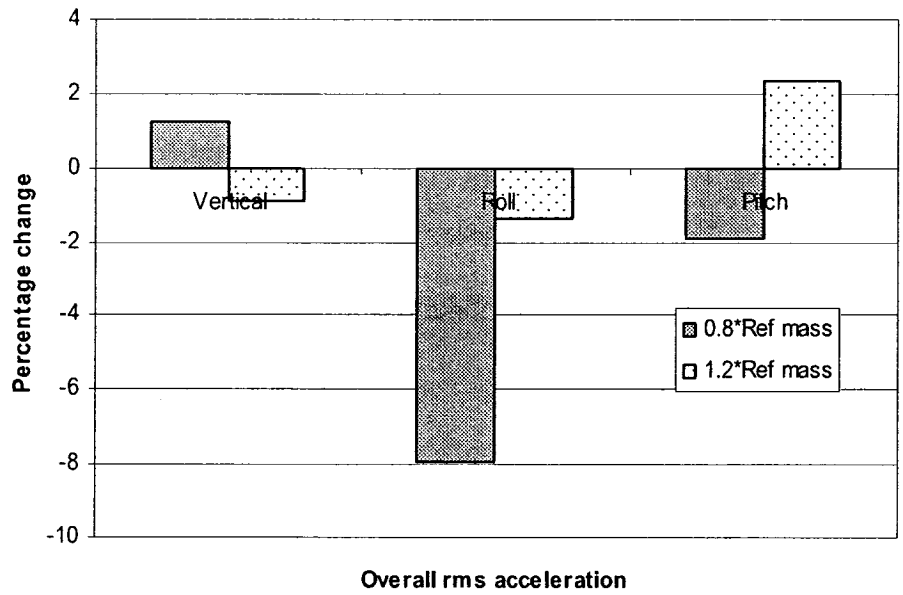

(a)

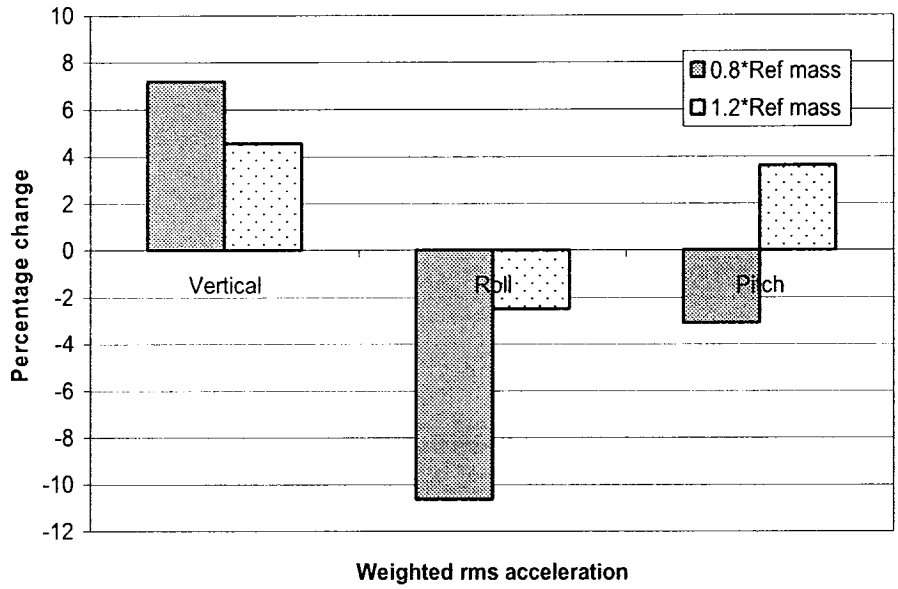

(b)

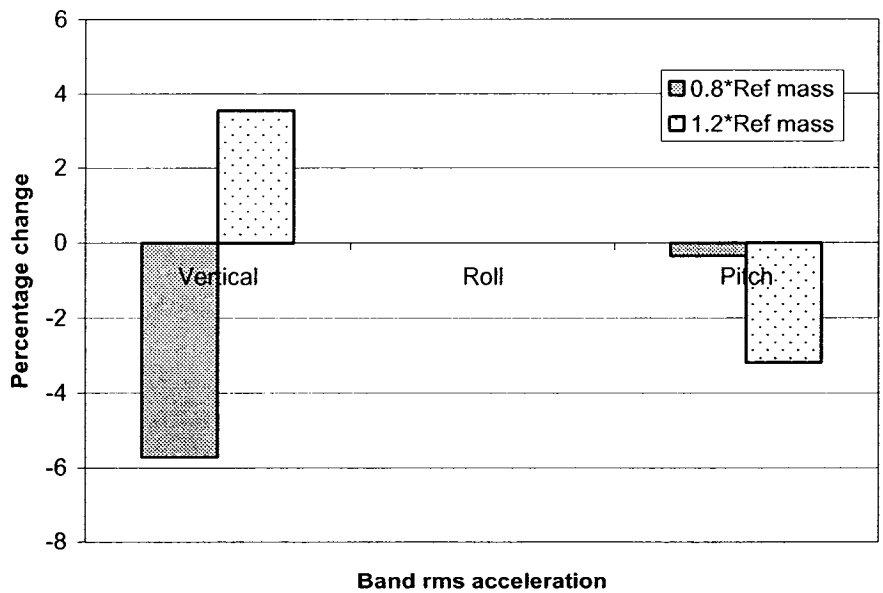

Figure 5.8: Influence of bogie mass: (a) Overall rms acceleration, (b) weighted rms acceleration and (c) band rms acceleration ($v = 60$ km/h, 100% load).

5.3.9 Bogie roll mass moment of inertia

Bogie roll mass moment of moment of inertia affects natural frequencies of axle lateral, axle roll and bogie roll modes. Due to increase in bogie roll inertia natural frequencies corresponding to above mentioned modes decrease. Figure 5.9(a, b and c) illustrates effect of bogie roll on ride comfort of operator. As seen in Fig. 5.9(a, b and c) bogie roll has little or no affect on vertical or pitch rms accelerations. Overall and weighted rms roll acceleration decrease due to change in bogie roll inertia from reference value, while the rms acceleration value decreases more due to decrease in bogie roll moment inertia as compared to inertia increase. This is due to the fact that although due to inertia increase there is an overall decrease in rms acceleration value but band rms acceleration increases.

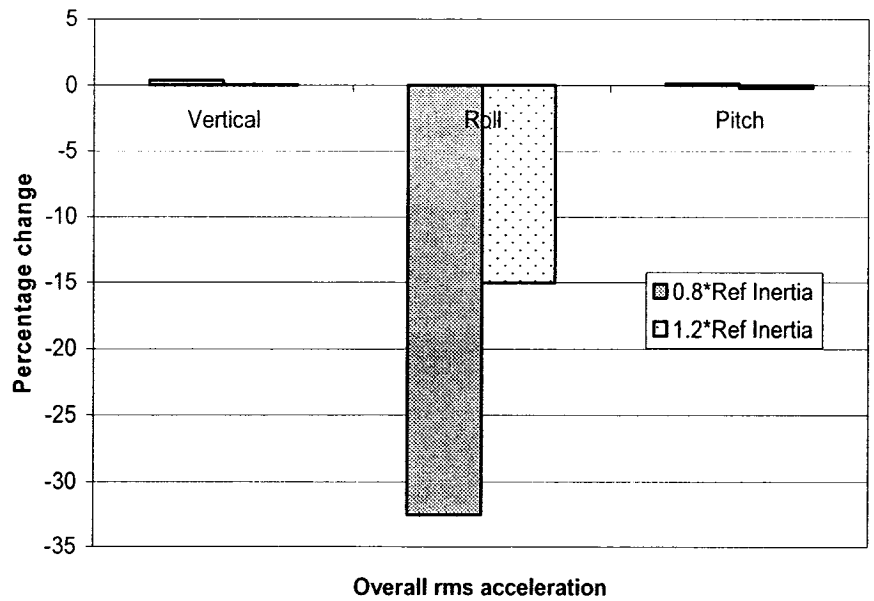

(a)

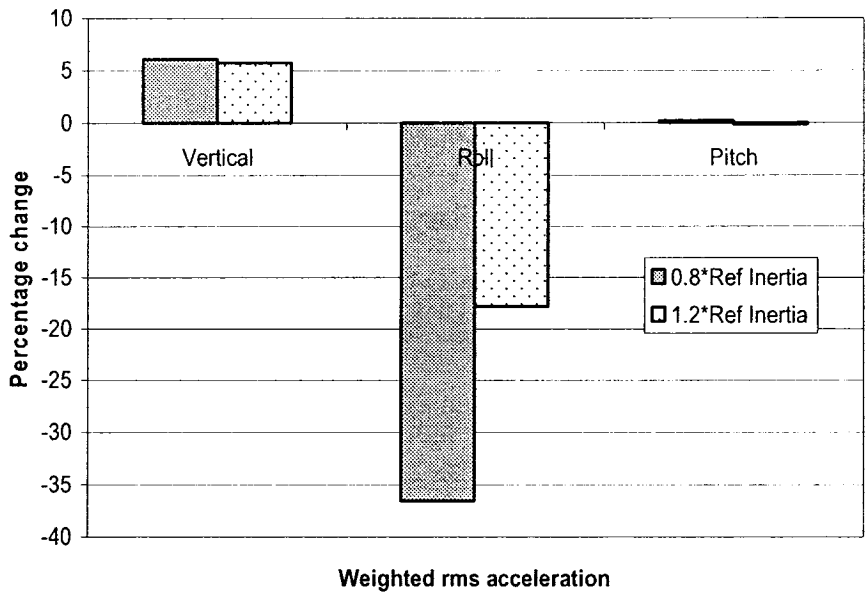

(b)

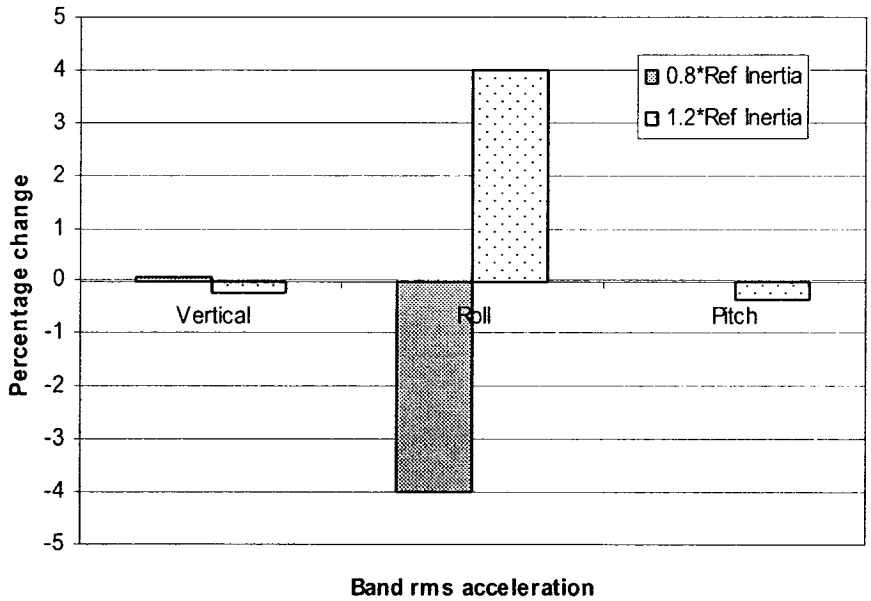

(c)

Figure 5.9: Influence of bogie mass moment of roll inertia: (a) Overall rms acceleration, (b) weighted rms acceleration and (c) band rms acceleration ($v = 60$ km/h, 100% load).

5.3.10 Bogie pitch mass moment of inertia

Effects of bogie pitch mass moment of inertia are tabulated in Fig. 5.10(a, b and c). Change in bogie pitch inertia affects axle vertical and bogie pitch mode natural frequencies. Overall rms acceleration in vertical and pitch direction show little change due to change in bogie pitch inertia. Only roll acceleration shows an increase of 4.3% due to 20% increase in inertia. Although overall vertical acceleration shows small decrease, the weighted vertical rms acceleration shows an increase of more than 5% due to 20% change in bogie pitch inertia, which shows that bogie pitch effects are more prominent in 4-8 Hz.

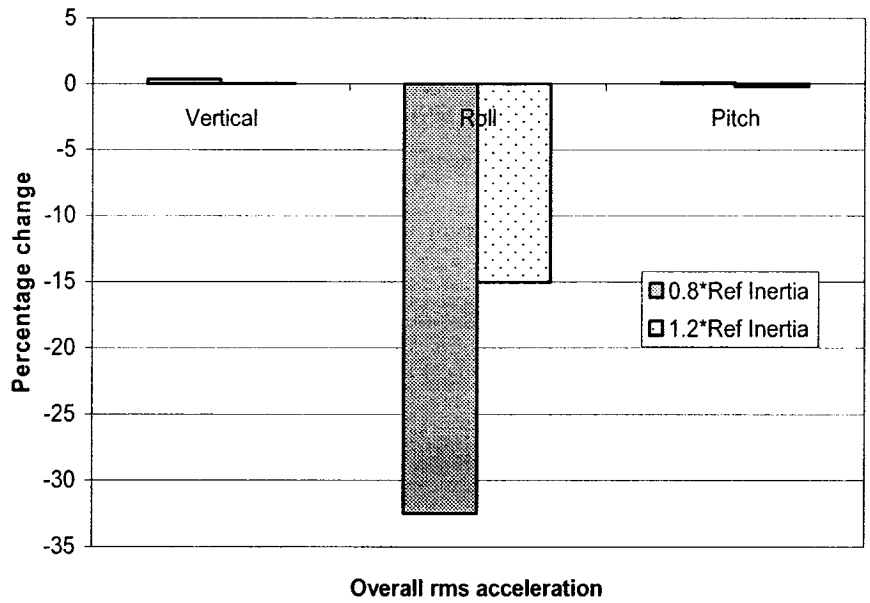

(a)

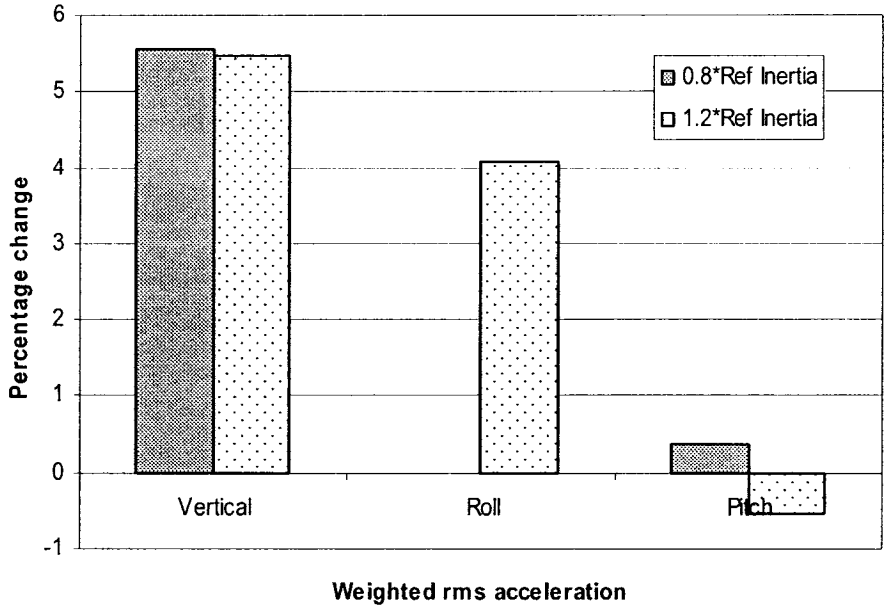

(b)

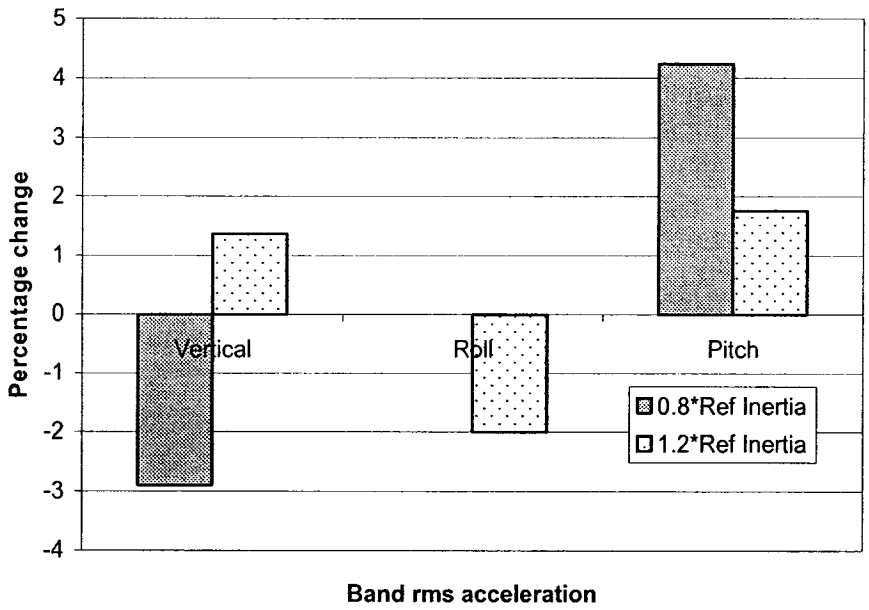

(c)

Figure 5.10: Influence of bogie pitch mass moment of inertia: (a) Overall rms acceleration, (b) weighted rms acceleration and (c) band rms acceleration ($v = 60$ km/h, 100% load).

5.3.11 Rubber mount stiffness

Each axle is connected to the bogie through four rubber mounts. Both vertical and radial stiffness of the rubber mounts are considered. Effect of rubber mount stiffness is shown in Fig. 5.11(a, b and c). Due to increase in rubber mount stiffness axle vertical, axle roll and axle lateral natural frequencies increase along with little increase in bogie pitch and car pitch mode frequencies and damping ratios for these modes decrease. While overall rms vertical acceleration increases with increase in rubber mount stiffness, there is a decreasing trend observed in weighted and band rms vertical accelerations. This implies that due to increase in stiffness there is an increase in axle response magnitude which occurs at frequencies above 16 Hz and in the frequency range of 4-8 Hz (this frequency range corresponds to bogie pitch and bogie vertical mode) there is a decrease in magnitude of vertical response as evident from Figs. 5.11(b and c). Overall and weighted rms roll accelerations decrease due to change in rubber mount stiffness from reference value and this decrease is more than 10% due to 20% decrease in stiffness. In general, it could be stated that due to increase in rubber mount stiffness response which occur at frequencies higher than 8 Hz increase in magnitude (axle modes lie in this region) and responses in the frequency range 1-8 Hz (car and bogie modes) decrease in magnitude.

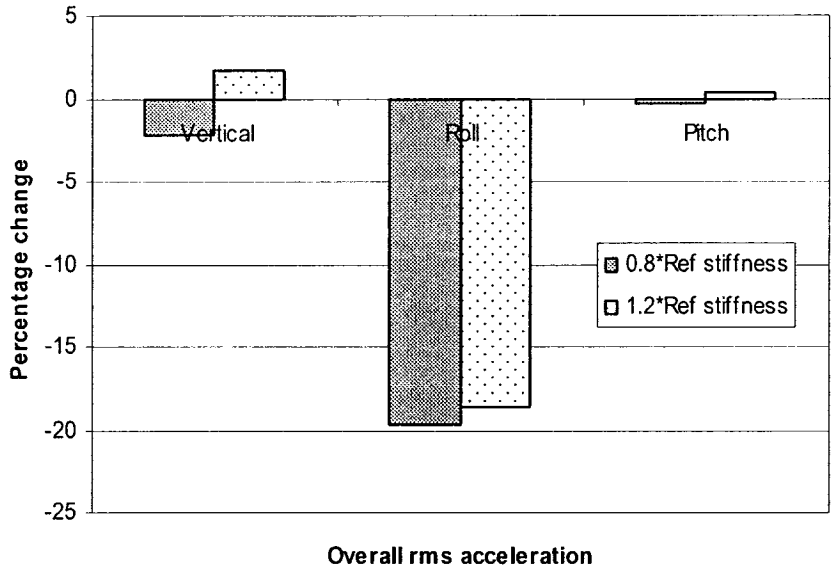
5
0
-5
-10
-15
-20
-25
Percentage change
Vertical
Roll
Pitch
0.8*Ref stiffness
1.2*Ref stiffness
Overall rms acceleration

(a)

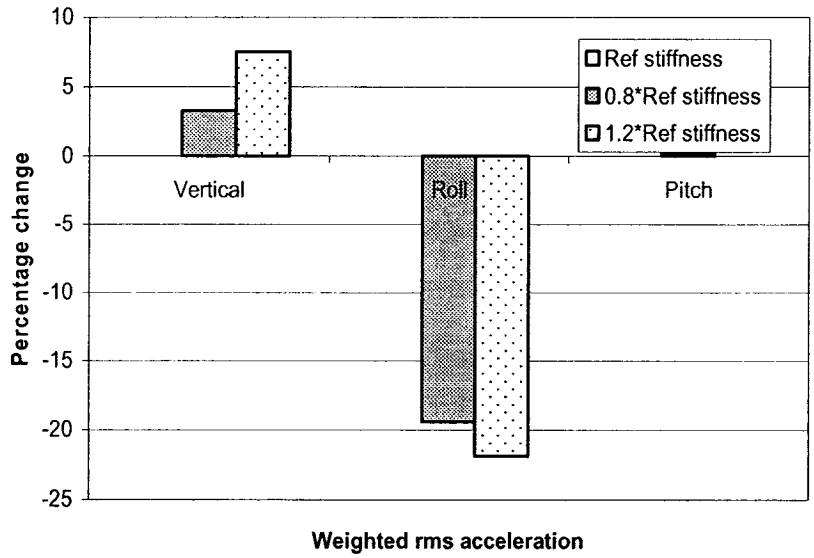
10
5
0
-5
-10
-15
-20
-25
Percentage change
Vertical
Roll
Pitch
Ref stiffness
0.8*Ref stiffness
1.2*Ref stiffness
Weighted rms acceleration

(b)

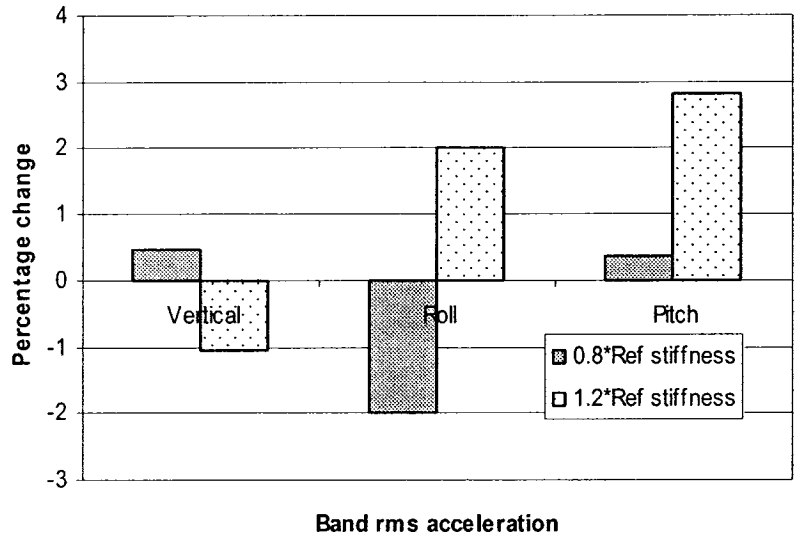

(c)

Figure 5.11: Influence of rubber mount stiffness: (a) Overall rms acceleration, (b) weighted rms acceleration and (c) band rms acceleration ($v = 60$ km/h, 100% load).

5.3.12 Rubber mount damping

Figure 5.12(a, b and c) illustrate effect of rubber mount damping on ride friendliness of the metro vehicle. Due to increase in rubber mount damping there is an increase in damping ratios of modes occurring at frequencies above 10 Hz. Bogie pitch is the only mode below 10 Hz whose damping ratio also increases. Vertical rms acceleration in Figs. 5.12(a and c) show very little or no change while weighted rms vertical acceleration shows increase in magnitude with changes in damping. This phenomenon could be attributed to the fact that rubber mount damps high frequency (higher than 10 Hz) responses only. Although high frequency responses are decreasing in magnitude, low frequency (1-8 Hz) responses increase in magnitude as is evident from Fig. 5.12(c) which shows response in 4-8 Hz frequency range. Rubber mount damping

affects roll acceleration the most as there is a decrease of 25% and 30%, respectively, in overall and weighted rms roll accelerations.

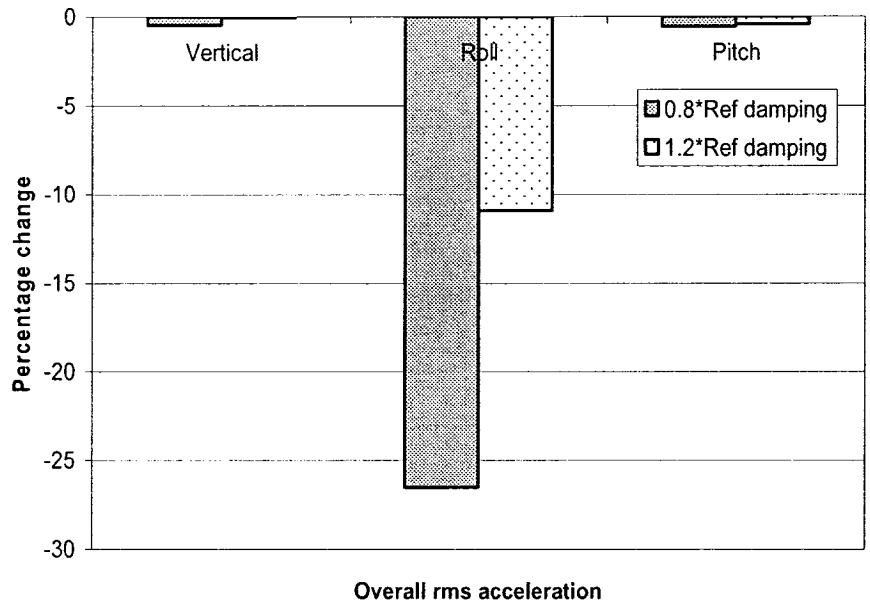

(a)

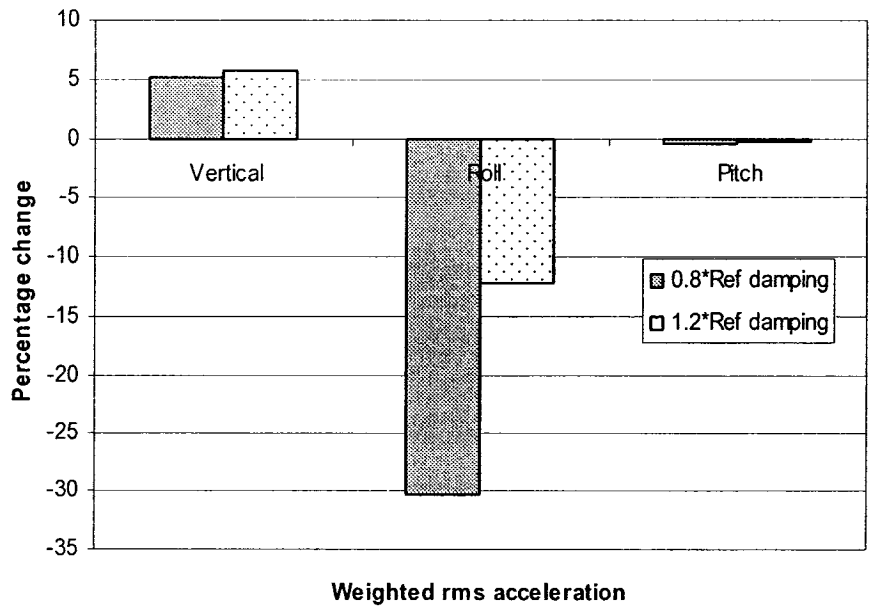

(b)

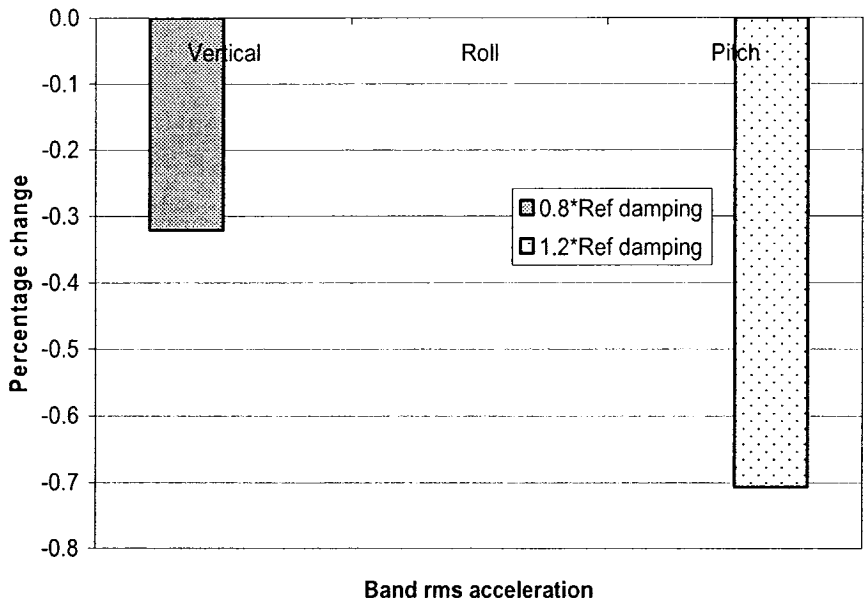

(c)

Figure 5.12: Influence of rubber mount damping: (a) Overall rms acceleration, (b) weighted rms acceleration and (c) band rms acceleration ($v = 60$ km/h, 100% load).

5.3.13 Axle mass

Figure 5.13(a, b and c) illustrate effect of axle mass on performance measures. Axle mass affects axle mode natural frequencies along with bogie vertical and bogie pitch mode natural frequency. Due to increase in axle mass there is decrease in damping ratios of lower frequency modes (car and bogie modes) and increase in damping ratios of axle modes which occur at frequencies above 10 Hz. Overall rms acceleration illustrated in Fig. 5.13(a) shows very small decrease in vertical acceleration, this is due to the fact that although responses below 10 Hz are increasing in magnitude, responses above 10 Hz are decreasing in magnitude and the overall affect is slight decrease in overall vertical rms acceleration. Figures 5.13(b and c) illustrate weighted and band rms acceleration;

these figures show an increase in vertical rms acceleration as they focus in the frequency range of 4-8 Hz. Roll and pitch accelerations in Fig. 5.13(a and b) show increase due to increase in axle mass and decrease due to 20% decrease in axle mass.

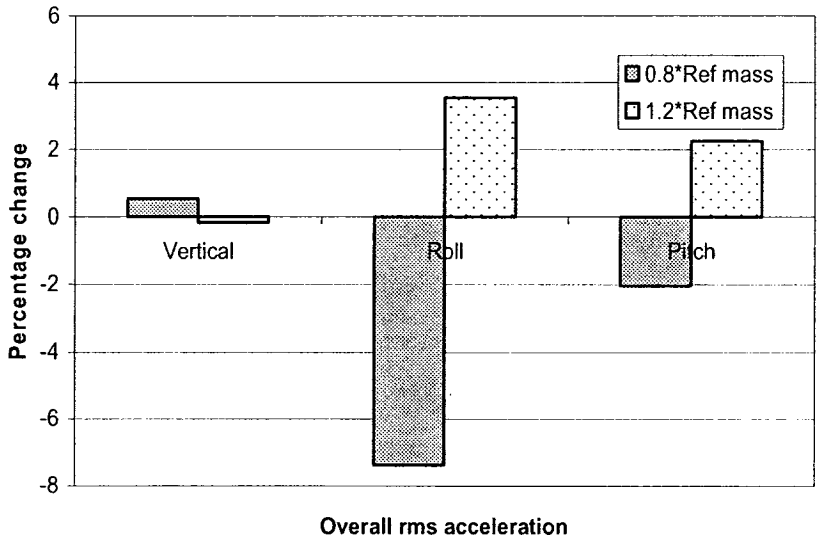

(a)

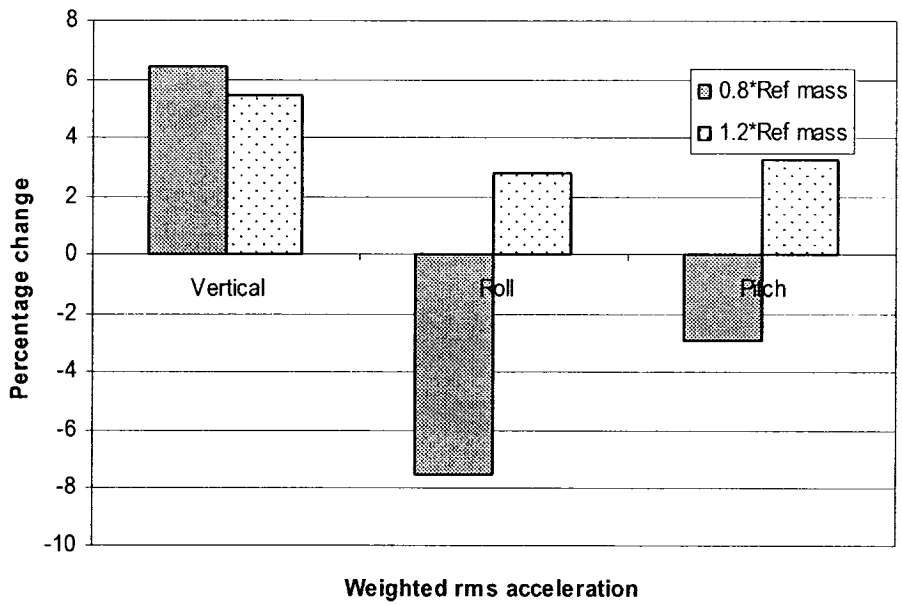

(b)

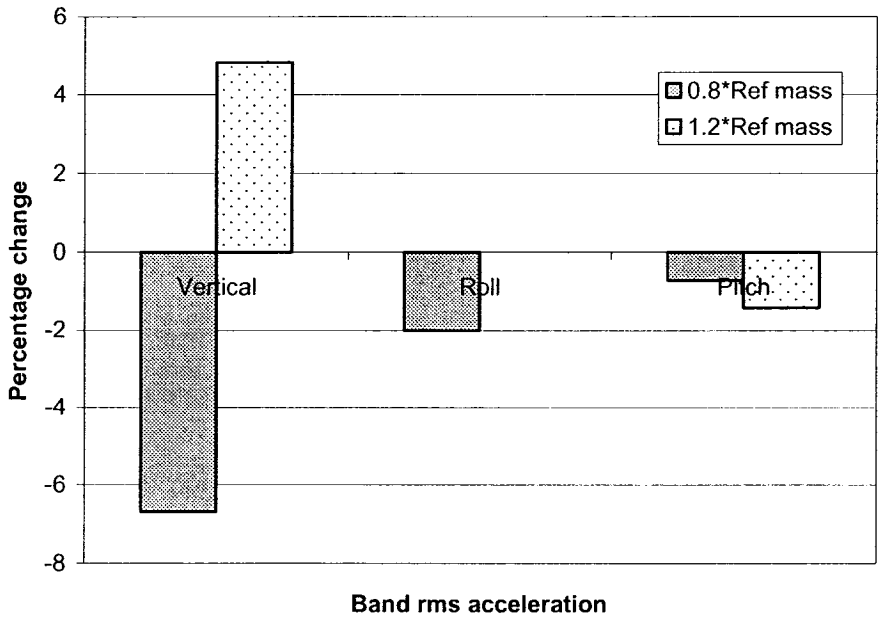

(c)

Figure 5.13: Influence of axle mass: (a) Overall rms acceleration, (b) weighted rms acceleration and (c) band rms acceleration ($v = 60$ km/h, 100% load).

5.3.14 Axle roll mass moment of inertia

Effect of axle roll mass moment of inertia is shown in Fig. 5.14(a, b and c). There is very little change in vertical and pitch responses due to change in axle roll inertia. Axle roll and bogie roll natural frequencies decrease with increase in axle roll inertia. Figures 5.14(a and c) show almost no change in rms acceleration while Fig. 5.14(b) reveals an increase of up to 5% in vertical weighted rms acceleration due to change in roll inertia. Roll rms acceleration as shown in Fig. 5.14(a and b) decrease due to change in axle roll inertia but in the frequency range of 4-8 Hz there is a decrease of 6% due to 20% decrease in inertia and increase of 6% rms acceleration due to 20% increase in inertia.

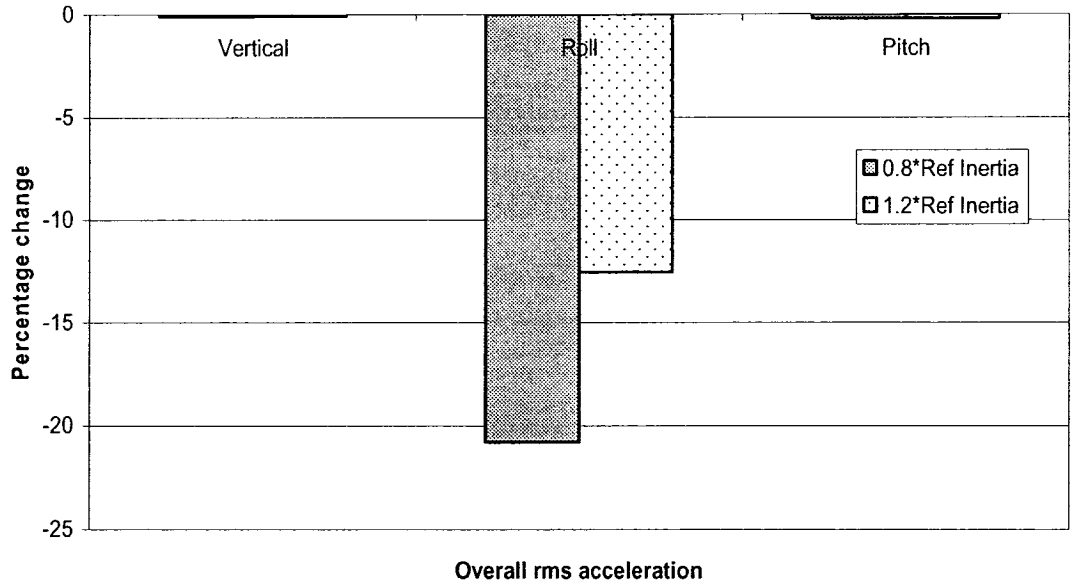
0
-5
-10
-15
-20
-25
Percentage change
Vertical
Roll
Pitch
0.8*Ref Inertia
1.2*Ref Inertia
Overall rms acceleration

(a)

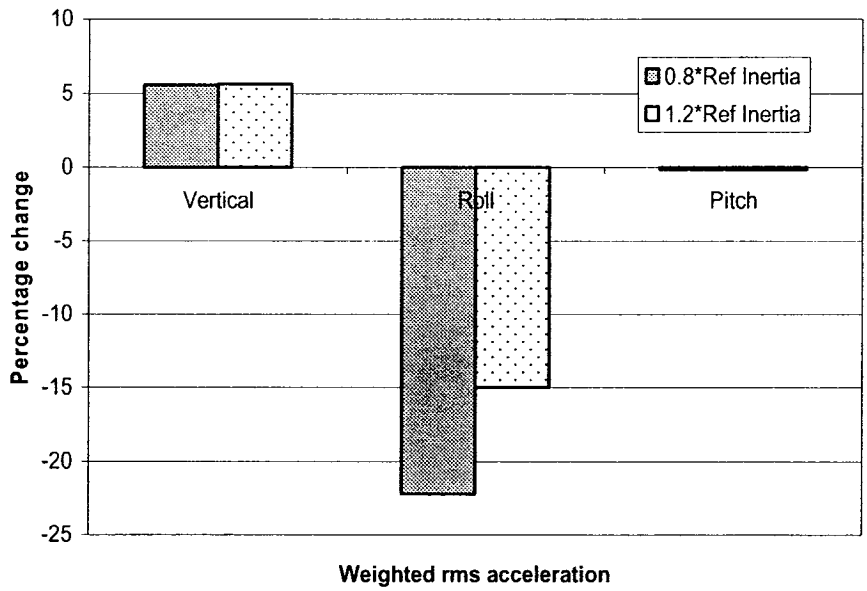
10
5
0
-5
-10
-15
-20
-25
Percentage change
0.8*Ref Inertia
1.2*Ref Inertia
Vertical
Roll
Pitch
Weighted rms acceleration

(b)

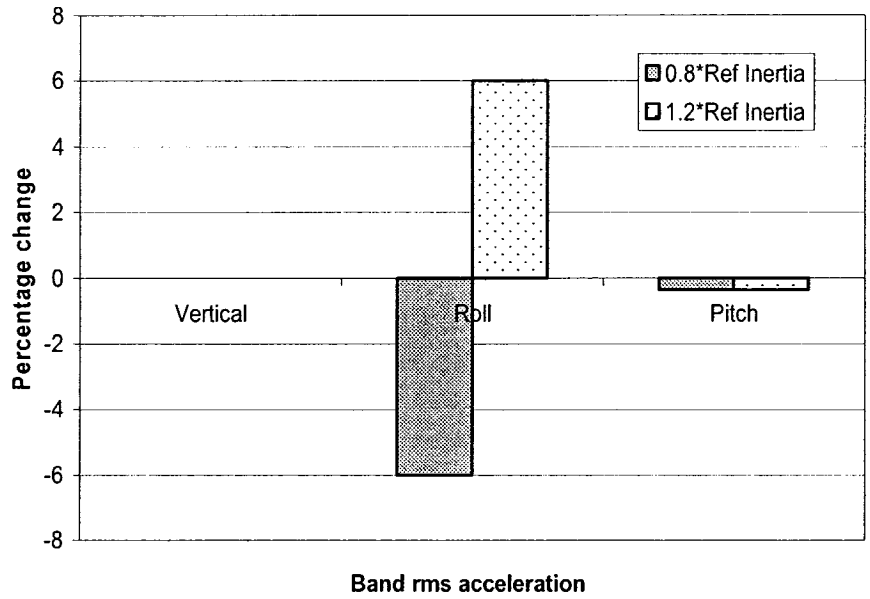

(c)

Figure 5.14: Influence of axle roll mass moment of inertia: (a) Overall rms acceleration, (b) weighted rms acceleration and (c) band rms acceleration ($v = 60$ km/h, 100% load).

5.3.15 Tire stiffness

Due to change in tire stiffness there is prominent change in natural frequencies and damping ratios corresponding to modes in the frequency range 1-16 Hz. With increase in tire stiffness there is increase in natural frequencies and decrease in damping ratios. Figure 5.15(a, b and c) illustrate effect of tire stiffness on the ride quality of the metro vehicle. Vertical, roll and pitch rms acceleration (overall and weighted) show increase in magnitude with 20% increase in tire stiffness and vice-versa due to 20% decrease. Overall and weighted pitch rms acceleration increases due to 20% change in tire stiffness but the band rms acceleration shows decrease of 17% due to 20% decrease in tire stiffness which implies that although overall there is an increase in pitch

acceleration magnitude due to decrease in tire stiffness, but in the frequency range of 4-8 Hz the magnitude of pitch acceleration decreases.

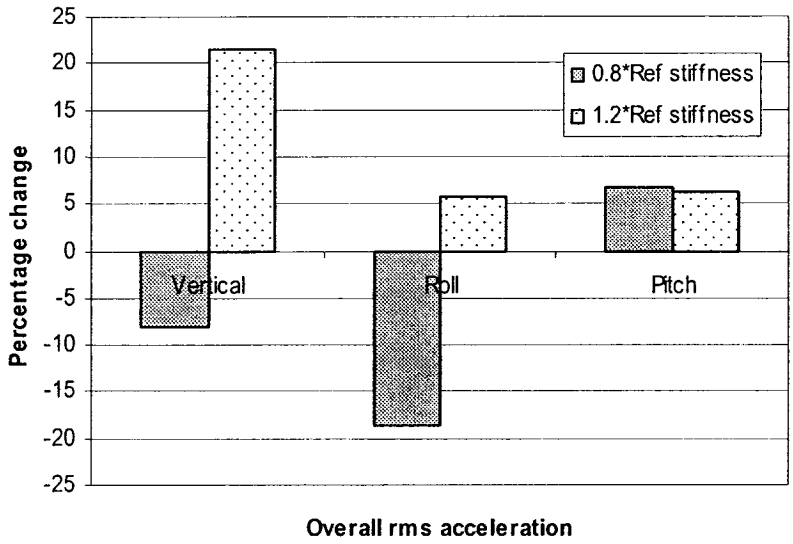

(a)

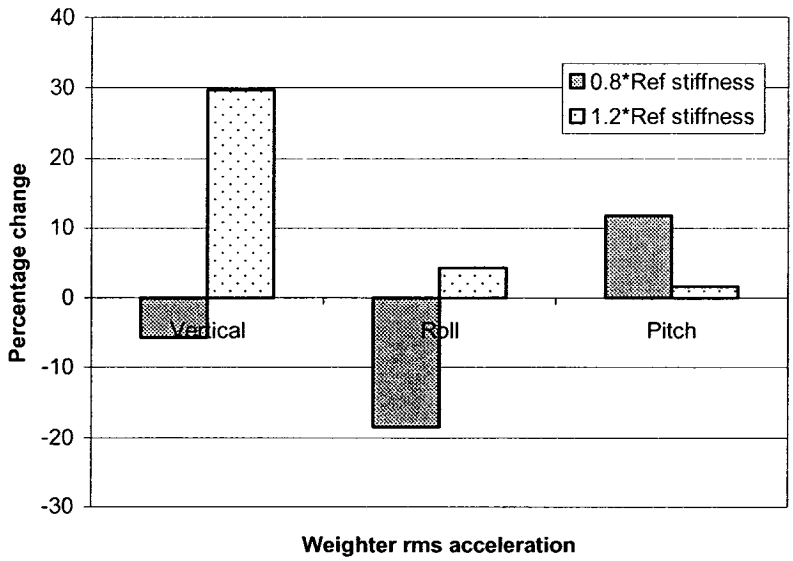

(b)

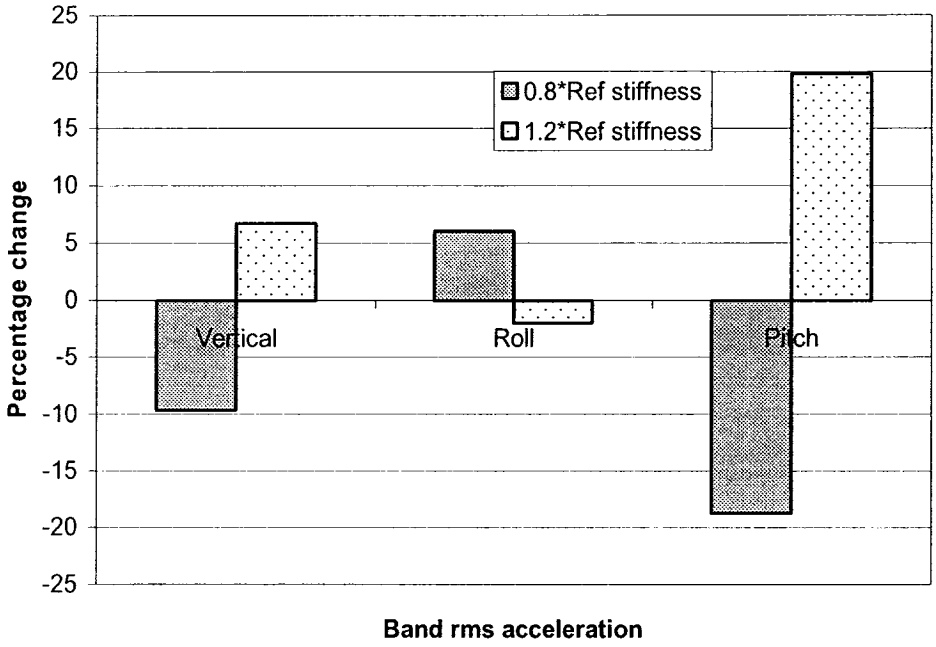

(c)

Figure 5.15: Influence of tire stiffness: (a) Overall rms acceleration, (b) weighted rms acceleration and (c) band rms acceleration ($v = 60$ km/h, 100% load).

5.3.16 Tire damping

Tire damping has minimal effect on overall vertical and pitch rms acceleration as seen from Fig. 5.16(a), while the overall roll rms acceleration decreases due to change in tire damping value from its nominal value. The overall rms acceleration decreases to 17.5% and 15% due to 20% decrease and increase, respectively, in the nominal value of the tire damping. Weighted rms acceleration in vertical direction increases up to 5% due to change in tire damping as shown in Fig. 5.16(b), suggesting increase in car vertical response in the 1-4 Hz range. The band rms acceleration (Fig 5.16 (c)) reveals a small decrease in vertical rms acceleration due to 20% in tire damping, while the band roll rms

acceleration decreases up to 2% due to 20% decrease in tire damping, suggesting very small influence of tire damping in the 4-8 Hz frequency range.

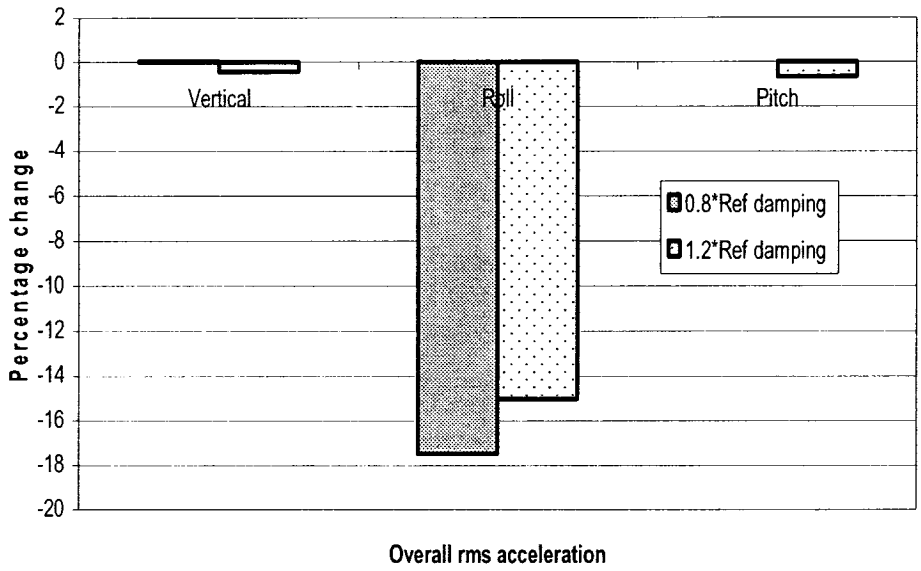

(a)

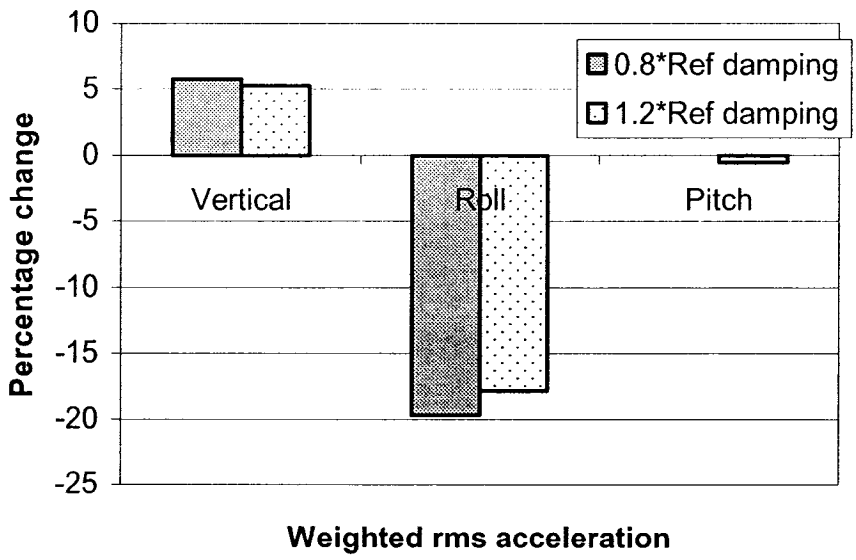

(b)

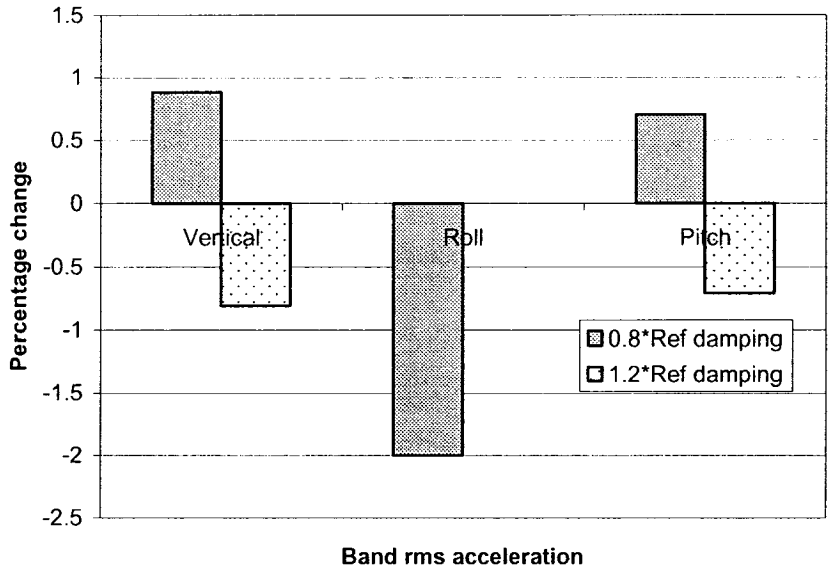

(c)

Figure 5.16: Influence of tire damping: (a) Overall rms acceleration, (b) weighted rms acceleration and (c) band rms acceleration ($v = 60$ km/h, 100% load).

5.4 OPTIMAL DESIGN PARAMETERS

In the previous sections, effect of various design parameters is studied by increasing and decreasing 20% from the nominal value of the parameter under study. In order to summarize the parametric sensitivity analysis and to come up with a set of beneficial design parameters which would result in a maximum reduction in rms acceleration, one configuration is chosen from a set of three configurations (80% of reference value, reference value and 120% of reference value) for each design parameter. The configuration which resulted in maximum decrease in overall, weighted and band rms acceleration, is chosen as an optimal design parameter. Figure 5.17(a) illustrates the percentage reduction in overall rms acceleration of car body in vertical, roll and pitch by employing optimal set of parameters. Vertical rms acceleration decreases by 12.1%,

while the roll and pitch unweighted rms accelerations decrease by 50% and 14.5%, respectively. Fig. 5.17(b) demonstrates similar decrease in weighted rms acceleration in the three coordinates by employing optimal set of parameters.

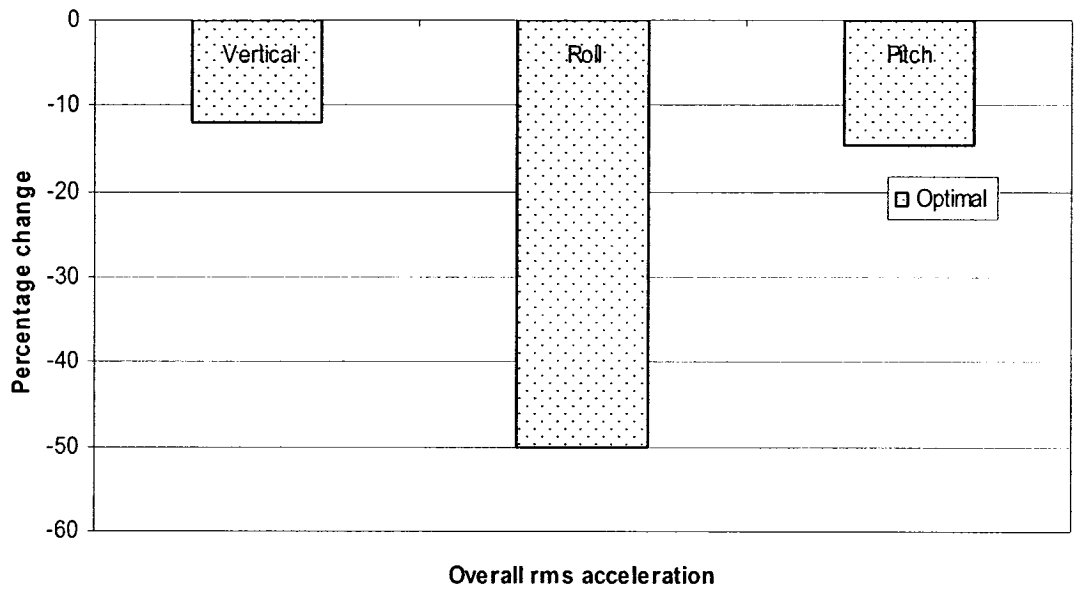

(a)

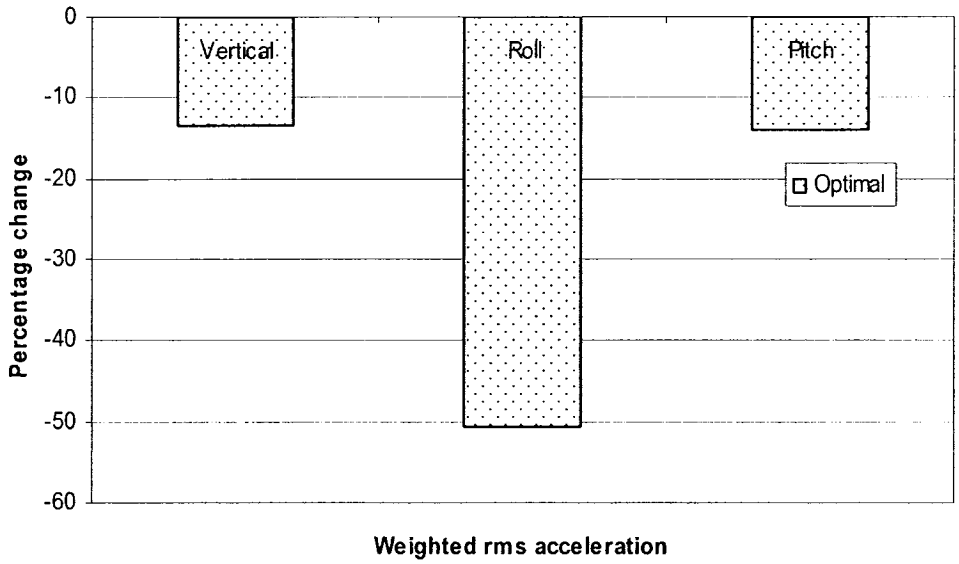

(b)

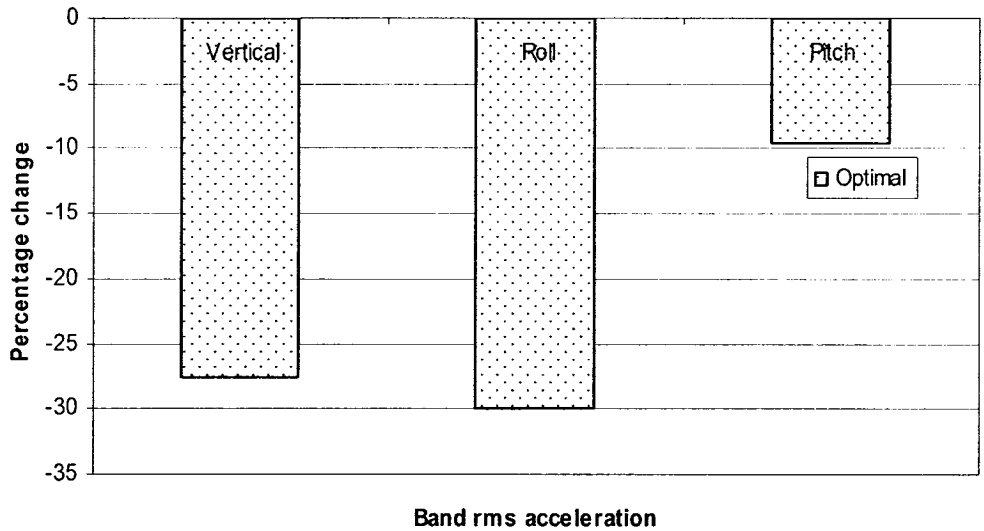

(c)

Figure 5.17: Influence of optimal parameters: (a) Overall rms acceleration, (b) weighted rms acceleration and (c) band rms acceleration ($v = 60$ km/h, 100% load).

5.5 SUMMARY

In this chapter, parametric sensitivity analysis is performed for the metro car while employing the model developed in chapter 2. Influence of operational and design parameters is studied and finally a set of beneficial parameters are identified from three configurations of each design parameter. In the following chapter, conclusions drawn from the model development and parametric sensitivity analysis are summarized.

6 CONCLUSIONS AND RECOMMENDATIONS FOR FUTURE WORK

6.1 INTRODUCTION

In this thesis the ride vibration analysis of the subway vehicle has been carried out. The major objective was to determine the ride-friendliness of the subway vehicle for the operator. Specifically, a three dimensional, lumped mass mathematical model of the subway vehicle has been developed and characterization of track roughness, mass-unbalance and non-uniformity due to tire out-of-roundness is made. Analysis of effects of various operational and design parameters on the performance measures relevant to operator's comfort has been carried out through parametric study.

6.2 HIGHLIGHTS OF THE PRESENT WORK

In this thesis, the ride vibration and ride quality analysis of a subway vehicle is carried out through analytical methods with computer simulations. The proposed analytical model is a frequency-domain ride simulation model formulated considering a three dimensional representation of the vehicle traversing over an arbitrary non-deformable track at a constant forward speed. The simulation model is a twenty three-degrees-of freedom dynamic system incorporating suspension kinematics and dynamics, and wheel-track interactions. For the purpose of dynamic modeling, the subway vehicle is divided into three major components: car body, bogie and axle. Lumped mass parameters are used to describe inertial properties and linear properties are used for describing suspension properties. Each unsprung mass is coupled to the sprung mass through the respective suspension components, modeled as parallel combinations of linear energy restoring and dissipative elements. The tire-track interactions are represented by point

contact tire model. Free vibration analysis of the analytical model is carried out to identify the important natural frequencies and modes of vibration. The analytical model is then validated by comparing the PSD of ride accelerations with the experimental results obtained previously. The vehicle model is analyzed for stochastic excitations arising from track profile in conjunction with sources of self excitation such as wheel unbalance and wheel non-uniformity.

- **Characterizations of wheel unbalance and wheel non-uniformity**

During the experiments tires were found to be out-of-round (OOR) after cars have been in operation for some time. This OOR can cause mass-unbalance and non-uniformity in tire. The unbalance can exist in any plane of the wheel, while the study in this thesis is limited to in-plane wheel unbalance only. In order to characterize the wheel non-uniformity (radial run-out), the wheel profile is assumed to be a semi-ellipse and semi-circle. The locus traced by this new wheel with radial run-out can be obtained by expressing the equation of ellipse and circle in terms of their polar co-ordinates and then deriving the expression for the variations in the radial difference as a function of the angular coordinate. This expression is then included in the equation for calculating the profile similar to track profile and is given as an input to the car in conjunction with track irregularity.

- **Parametric sensitivity analysis**

As the ride accelerations of the vehicle are strongly related to the operating and design parameters, a comprehensive parametric study is carried out to observe the influences of various operating and design parameters on the acceleration based performance measures. Main focus of the thesis is to find ride comfort of the subway

vehicle for the operator. Therefore, all the accelerations were found at operator position on the floor of the car. For assessing the affect of various parameters on the operator comfort three performance measures are used, namely, overall rms acceleration (unweighted), weighted rms acceleration, and band rms acceleration. Unweighted and weighted rms accelerations were found for the response in the frequency range of 0.5-20 Hz, while band rms acceleration was found in the frequency range of 4-7 Hz. These performance measures were evaluated in vertical, roll and pitch directions.

6.3 CONCLUSIONS

The present research work has focused on the development of an effective ride dynamic model of a subway vehicle through validation against previously carried out experimental measurements and a systematic parametric study. It has been shown that a simplified yet credible mathematical formulation of a complex vehicle-track dynamical system yields reasonably accurate ride predictions. Various conclusions drawn from the study are grouped in two categories, where the first category comprises of those drawn from the analytical modeling strategies and their assessment based on the field validation. The second category of conclusions focuses on the affect of various operational and design parameters on the ride dynamic behavior of the subway vehicle.

The major conclusions drawn from the analytical modeling approach and the ride dynamic behavior are summarized below:

- Parametric sensitivity analysis was performed, which concluded that roll rms acceleration of the car is affected by changes in pitch mass moment of inertia of the car and similarly, pitch rms acceleration is affected by changes in roll mass

moment of inertia, which suggests that a three dimensional mathematical model is necessary to understand the dynamic couplings involved in different planes.

- The ride dynamic mathematical model of the metro car developed in this dissertation was able to reproduce all the major frequency components in the frequency range of interest. From the comparison of model and experimental acceleration responses of the car body, bogie and axle, it could be concluded that the mathematical model could simulate reasonably well, the actual vibration environment of the metro car in the frequency range concerning the human vibration.

- The magnitude of weighted rms acceleration in the vertical direction for the metro car lies in the 0.38-0.63 m/s^2 range. ISO-2631-1 provides approximate range of comfort reactions to vibration environments, given by[53]:

  0.315 m/s^2 to 0.63 m/s^2 .....a little uncomfortable.

  0.5 m/s^2 to 1 m/s^2 .....fairly uncomfortable.

  The weighted rms acceleration produced by the metro car lies in the little to fairly uncomfortable zone.

- The magnitude of rms acceleration in the vertical direction was computed at the vehicle forward speeds of 45, 60 and 75 km/h. The magnitude of vertical rms acceleration at 45 and 75 km/h was higher when compared to that at 60 km/h. At 45 and 75 km/h the tire angular speed corresponds to 4.2 and 7.2 Hz, respectively, which is near the bogie pitch mode (4.5 Hz) and bogie bounce mode (6.7 Hz). Therefore it could be concluded that the rms acceleration in the vertical direction increases at those vehicle speeds which correspond to the

resonant frequencies. Alternately, it could be concluded that the ride quality of the metro car can be enhanced at speeds which do not correspond to the resonant frequencies of the rigid body modes i.e. 45 km/h and 65~70 km/h.

- Effect of passenger load was observed under the operating speed of 60 km/h. It was observed that the magnitude of rms acceleration in the vertical direction was minimum when the passenger load was maximum due to change in resonant frequencies of the car vertical mode. Thus, it could be concluded that increase in passenger load and car mass enhances the overall ride quality of the metro vehicle.

- Overall and weighted vertical ride rms acceleration decreases due to decrease in stiffness and increase in damping of the elastomeric springs. Therefore, the ride quality of the metro vehicle can be enhanced with a suspension system having softer springs and higher damping.

- Change in car roll mass moment of inertia from its nominal value decreases roll rms acceleration.

- The weighted rms acceleration in the vertical direction increases due to either increase or decrease in the nominal value of the bogie and axle mass. However, the rms acceleration in the 4-8 Hz frequency range decreases due to decrease in bogie and axle masses. The roll rms acceleration of the car also decreases due to 20% decrease in the masses of axle and bogie. It could thus be concluded that in order to improve the ride quality of the metro vehicle in the vertical direction, which concerns with the vibration environment in the 4-8 Hz frequency range, lighter bogie and axles are required.

- The weighted rms acceleration in the vertical direction are minimum at the nominal value of rubber mount stiffness and damping, while the weighted rms roll acceleration decreases significantly with either increase or decrease in the nominal value of rubber mount stiffness and damping. Therefore, roll vibration of the metro car can be reduced with a suspension element with higher stiffness and lower damping, at a small cost of increasing the vertical response. This would need further optimization studies.
- Due to decrease in tire stiffness the overall and weighted vertical and roll rms acceleration decreases, suggesting a better ride quality of the metro car by employing tires with stiffness values lower when compared to the existing tires. The effect of tire damping is more pronounced in roll rms acceleration as compared to the vertical rms acceleration of the car. It is observed that in order to decrease the roll vibration of the car the damping value of the tire should be decreased, while, decreased damping would result in slight increase in the vertical rms acceleration in the 4-8 Hz frequency range.
- By employing optimal set of parameters (varied in the range of ±20% of the nominal value) lower values of unweighted and weighted (vertical: 11%, roll: 50%, pitch: 14%) rms acceleration can be obtained in vertical, roll and pitch directions. The optimal parameters result in decreasing the vertical, roll and pitch acceleration by 27%, 30% and 9.6%, respectively, in the 4-8 Hz frequency range.

6.4 RECOMMENDATIONS FOR FUTURE WORK

The present research work resulted in a computer simulation model which has been validated using the field test data. The potential usefulness of the computer model can be further enhanced upon consideration of the following:

- Although the three dimensional model developed in this study provides reasonable correlation in the frequency range 0.5~20 Hz, it is unable to give correct responses in higher frequency range. Structural flexibility can be taken into account to study its effect on the ride acceleration responses.
- In the present study linear characteristics of the suspension system were used, non-linear properties of the suspension system could be used.
- The motor driving the vehicle is directly installed on the bogie frame beneath the driver location. It imposes considerable vibrations in the higher frequency bands. It is thus recommended to incorporate the motor components in the model. Such a model can provide significant information related to the influence of drive motor vibration on the overall ride quality. The results can then be employed to select appropriate engine and transmission mounts.
- Acceleration responses were found at car floor beneath the driver seat. Seat model could also be incorporated to study the effect of seat suspension and to get responses directly at driver-seat interface.
- The model could further be improved by including a better representation of tire non-uniformity and mass-unbalance.

REFERENCES

1 Rakheja, S., Politis, H., Juras, D. and Boileau, P.E., "Evaluation de l exposition aux vibration globales du corps des operateurs du metro de Montreal et etude du compartment dynamique et de leur systeme de suspension", Institut de Recherche Robert Sauve en Sante et en securite du Travail du Quebec, CONCAVE-2004-05.

2 Cebon, D., "Interaction between heavy vehicles and roads", The Thirty-Ninth L. Ray Buckendale Lecture, SAE Sp-951, 1993.

3 Frohling, R.D., Scheffel, H. and Ebersohn, W., "The vertical dynamic response of a rail vehicle caused by track stiffness variations along the track", Vehicle System Dynamics, 25, 1995, 175-187.

4 Dhir, A. and Sankar, S., "Analytical wheel modes for ride dynamic simulation of off road tracked vehicles", Vehicle System Dynamics, 27, 1997, 37-63.

5 Frohling, R.D., "Low frequency dynamic vehicle/track interaction: Modeling and Simulation", Vehicle System Dynamics, 29, 1997, 30-46.

6 Valesek, M., Stejskal, V., Sika, Z., Vaculin, O. and Korenda, J., "Dynamic model of truck for suspension control", Vehicle System Dynamics, 29, 1997, 496-505.

7 Manon, W.P. and Shang, J.C., "Dynamic analysis of rolling freight car", Anthology of rail vehicle dynamics – Effect of Train Action and Rail Car Vibration, Vol-2.

8 Dibok, W.B. and Bieniecki, H.S., "Suspension dynamics by computer simulation", Anthology of Rail Vehicle Dynamics – Effect of train action and rail car vibration, 2, 206-214.

9 Matsudaira, T., Matsui, N., Arai, S. and Yokose, K., "Problems on hunting of railway vehicles on test stand", Anthology of Rail Vehicle Dynamics – Effect of train action and rail car vibration, Vol-2.

10 Masayuki, M. and Hiroshi, F., "Vertical riding comfort of articulated railway vehicles", Vehicle System Dynamics, 15, 1985, 413-426.

11 Ladislav, R., "Dynamic analysis of mechanical part of a locomotive", Vehicle System Dynamics, 15, 1985, 481-495.

12 Evans, J.R., "The modeling of railway passenger vehicles", Vehicle System Dynamics, 20, 1991, 144-156.

13 Ahmed, A. K. W., "Ground Transportation Systems", Encyclopedia of Vibration, 2, 2002, 603-620.

14 Smith, A. R., "Frame bending, fifth wheel locations–special body moving and loading problem", SAE special report SR 260, 1965.

15 Ribartis, Aurell, J. and Andersers, E., "Ride comfort aspects of heavy truck design", SAE Tran., 781064, 1975, 4046-4069.

16 Michelberger, P. and Szole, D., "Speed dependent vertical vibrations of elastic vehicle bogies", Int. J. Vehicle Design, 8(1), 1985, 8-95.

17 Rakheja, S. and Woodrooffe, J.H.F., "Role of suspension damping in enhancement of road friendliness of heavy vehicles", Heavy Vehicle Systems, Int. J. of Vehicle Design, 3, 1996.

18 Stiharu, I. and Rakheja, S., "Laboratory Testing and Characterization of an Air Ride Spring", Prepared for Forestry Engineering Research Institute of Canada, 1995.

19 Ibrahim, I.M., Crolla, D.A. and Barton, D.C., "Effect of frame flexibility on the ride vibration of trucks", Computers & Structures, 58(4), 1996, 709-713.

20 Stribersky, A., Moser, F. and Rulka, W., "Structural dynamics and ride comfort of a rail vehicle system", Advances in Engineering Software, 33, 2002, 541-552.

21 Elchberger, A. and Schittenhelm, M., "Implementations, applications and limits of tire models in multi body simulation", Vehicle System Dynamics, 43, 2005, 18-29.

22 Sjoberg, M. and Kari, L., "Non linear behavior of a rubber isolator system using fractional derivatives", Vehicle System Dynamics, 37, 2002, 217-236.

23 Koeller, R.C., "Application of fractional calculus to the theory of viscoelasticity", Journal of Applied Mechanics, 51, 1984, 299-307.

24 Payne, A.R. and Whittaker, R.E., "Low strain dynamic properties of filled rubbers", Rubber Chem. Tech., 44, 1971, 440-478.

25 Sjoberg, M., "Rubber isolators- Measurements and modeling using fractional derivates and friction", S.A.E, Paper No. 2000-01-3518.

26 Dhir, A. and Sankar, S., "Analytical wheel modes for ride dynamic simulation of off road tracked vehicles", Vehicle System Dynamics, 27, 1997, 37-63.

27 Davis, D.C., "A radial-spring terrain-enveloping tire model", Vehicle System Dynamics, 1, 1975, 55-60.

28 Lloyd, N.A., "Effect of wheel non-uniformities on tire-wheel assembly and the vehicle", SAE, 680005.

29 Ni, E. J., "A mathematical model for tire/ wheel assembly balance", Tire Science and Technology, TSTCA, 21(4), 1993, 220-231.

30 Stutts, D.S., Krousgrill, C. M. and Sodel, W., "Parametric excitation of tire-wheel assemblies by a stiffness non-uniformity", Journal of Sound and Vibration, 179(3), 1995, 499-512.

31 Bohler, H., "Simulation of the dynamic loads of a tractor with the help of a multi-body-system program", ISTVS, 13th Int. Conf., Munich, Germany, 1999.

32 Pacejka, H. B. and Bekker, E., "The magic formula tire model", Vehicle System Dynamics, 21, 1993, 1-18.

33 Demic, M., "The definition of the tires limit of admissible non-uniformity by using the vehicle vibratory model", Vehicle System Dynamics, Vol-31, 1999, 183-211.

34 Mitschke, M., "Dynamic der Kraftfahrzeuge", Springer, 1973.

35 Simic, D., "Vehicle dynamics", (in Serbian) Naucna Knjiga, Belgrade, 1980.

36 Kenny, T., "Quantifying tire, rim and vehicle effects on ride quality", SAE 890369, SAE Warrendale, PA, 3/89.

37 Ni, E. J., "A mathematical model for tire/ wheel assembly balance", Tire Science and Technology, TSTCA, 21(4), October-December, 1993, 220-231.

38 Dorfi, H., "Tire non-uniformities: Comparison of analytical and numerical tire models and correlation to experimentally measured data", Vehicle System Dynamics, 43, 2005, 223-240.

39 Deodhar, A., "Ride dynamic response of commercial vehicles subjected to wheel unbalance and non-uniformity effects", Concordia University, Phd Thesis, 2005.

40 Kortum, W., "Review of multibody computer codes for vehicle system dynamics", Vehicle System Dynamics, Supplement, 22, 1993, 3-26.

41 Crolla, D. and M. Abdel-hady., "Active suspension control: performance comparisons using control laws applied to a full vehicle model", Vehicle System Dynamics, 20, 1991, 107-120.

42 Wong, J. Y., "Theory of ground vehicles", New York, John Wiley & Sons. 1993, 2nd ed.

43 Parsons, K. D., Whitham, E. M. and Griffin, M. J., "Six axis vehicle vibration and its effect on comfort", Ergonomics, 22(2), 1979, 211-225.

44 Goldman, D. E., "A review of subjective responses to vibratory motion of the human body in the frequency range 1 to 70 cps", Naval Medical Research Institute, Report No. 4, 1948.

45 Janeway, R. N., "Passenger vibration limits", SAE Journal, 56, 1948, 48-49.

46 Society of Automotive Engineers (1965), "Ride and vibration data manual", SAE HS/006A, Society of Automotive Engineers, Warrendale, Pennsylvania.

47 Van Deusen, B. D., "Human response to vehicle vibration", SAE Transactions, Paper No. 680090, 1968, 328-345.

48 Von Eldik Thieme, H.C.A., "Passenger riding comfort criteria and cethods of analyzing ride and vibration data", SAE Paper No. 295 A, 1961.

49 Butkunas, A. A., "Power spectral density and ride evaluation", SAE Transactions Paper No. 660138, 1966, 681-687.

50 Pradko, F. and Lee, R. A., "Vibration comfort criteria", Automotive Engineering Congress, Detroit, Michigan, Paper 660139, 1966, January 10-14.

51 Lee, R., and Pradko, F., "Analytical analysis of human vibration", SAE Transactions paper No. 680091, 1968, 346-370.

52 Griffin, M. J., "The evaluation of vehicle vibration and seats", Applied Ergonomics, 9, 1978, 15-21.

53 International Organization for Standardization, "Mechanical vibration and shock-evaluation of human exposure to whole body vibration", ISO-2631-1, 1997.

54 Dupuis, H. and Zerlett, G., "Whole-body vibration and disorders of the spine", International Archives of Occupational and Environmental Health, 1987, 59, 323-336.

55 Johanning, E., Wilder, D.G., Landrigan, P.J. and Pope, M.H., "Whole-body vibration exposure in subway cars and review of adverse health effects", Journal of Occupational Medicine, 33(5), 1991, 605-612.

56 Johanning, E., "Back disorders and health problems among subway train operators exposed to whole –body vibration", Scand J Work Environ Health, 17, 1991, 414-419.

57 Bongers, P.M. and Boshuizen, H.C., "Back disorders and whole-body vibration", University of Amsterdam, Ph.D. thesis, 1990.

58 Dupuis, H., "Vibration exposure and back disorders", Occupational Musculoskeletal Disorders: Occurrence, Prevention and Therapy, Eular Publishers, 1991, 51-57.

59 Hansson, T.H. and Holm, S., "Clinical implications of vibration-induced changes in the lumbar spine", Orthopedics Clinics of North America, 22, 1991, 247-252.

60 Ozkaya, N., Willems, B. and Goldsheyder, D. and Nordin, M., "Whole-body vibration exposure experienced by subway train operators", Journal of Low Frequency Noise and Vibration, 13(1), 1994b, 13-18.

61 Ozkaya, N., Willems, B. and Goldsheyder, D., "Effect of subway car design on vibration exposure", International Journal of Industrial Ergonomics, 19, 1997, 377-385.

62 Hunt, H.E.M., "Modeling of rail vehicles and track for calculation of ground-vibration transmission into buildings", Journal of Sound and Vibration, 193(1), 1996, 185-194.

63 Richard, M.J., "Évaluation du profil de la surface des pistes de roulement du métro de Montréal", Institut de Recherche Robert Sauve en Sante et en securite du Travail du Quebec, R-344.

64 Van Deusen, B. D., "Analytical techniques for design riding quality into automotive vehicles", SAE Transactions, Paper No. 670021, 1968, 328-345.

65 Wong, J. Y., "Effect of vibration on the performance of Off-Road vehicles", Journal of Terramechanics, 8(4), 1972.

66 Mandapuram, S., Rakheja, S. et al., "Influence of back support conditions on the apparent mass of seated occupants under horizontal vibration", Journal of Industrial Health, 43, 2005, 421-435.

67 Lundstrom, R, and Holmlund, P., "Absorption of energy during whole-body vibration exposure", 215(4), 1998, 789-799.

APPENDIX: A

FREQUENCY WEIGHTING TRANSFER FUNCTIONS

Frequency weightings are employed for determining the weighted rms acceleration in the principal directions. In the following appendix, the frequency weighting transfer functions are presented. The high pass filter $H_h(p)$ is expressed as:

$$|H_h(p)| = \left| \frac{1}{1 + \sqrt{2}\omega_1 / p + (\omega_1 / p)^2} \right| \tag{A.1}$$

in which, $\omega_1 = 2\pi f_1$, $p = j2\pi f$ and f_1 is the corner frequency (intersection of asymptotes).

$H_l(p)$ is low pass transfer filter function and expressed as:

$$|H_l(p)| = \left| \frac{1}{1 + \sqrt{2}p / \omega_2 + (p / \omega_2)^2} \right| \tag{A.2}$$

in which, $\omega_2 = 2\pi f_2$, and $f_2 = 100$ Hz is the corner frequency. Eqns. (A.1) and (A.2) are illustrated in Fig. A.1. The band limiting transfer function is determined from the product of high-pass and low-pass filters and is given by Eq. (A.3) and illustrated in Fig. A.2:

$$\text{Band pass filter} = H_h(p).H_l(p) \tag{A.3}$$

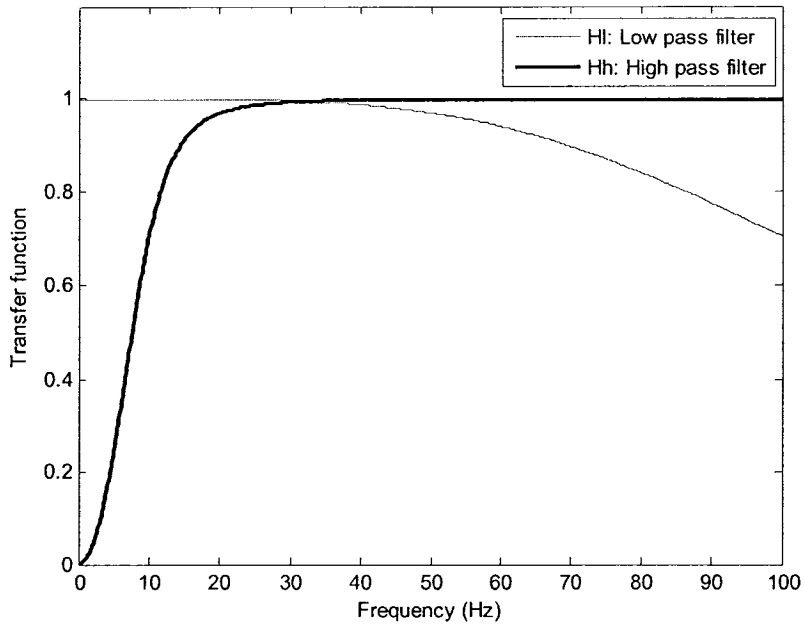

(a)

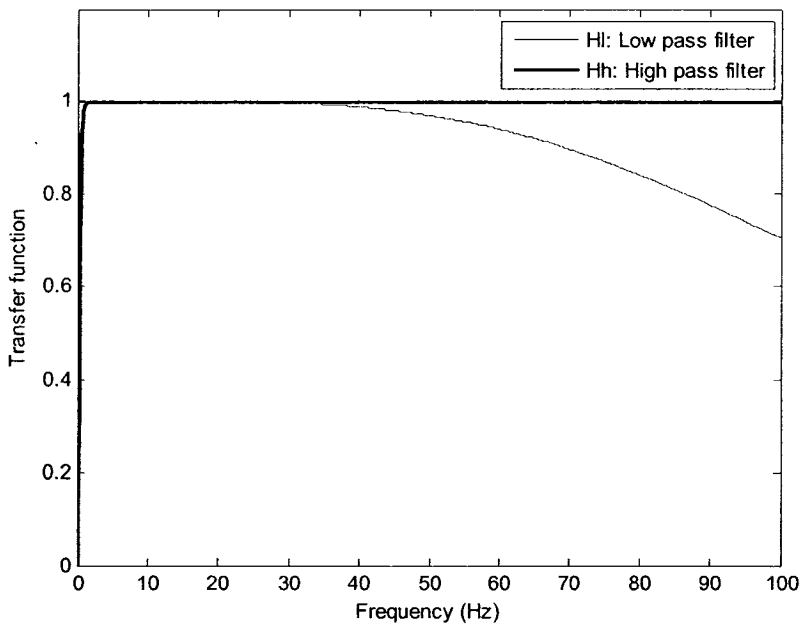

(b)

Figure A.1: High-pass and low-pass frequency weighting transfer function: (a) f_1=10 Hz, (b) f_1=10 Hz.

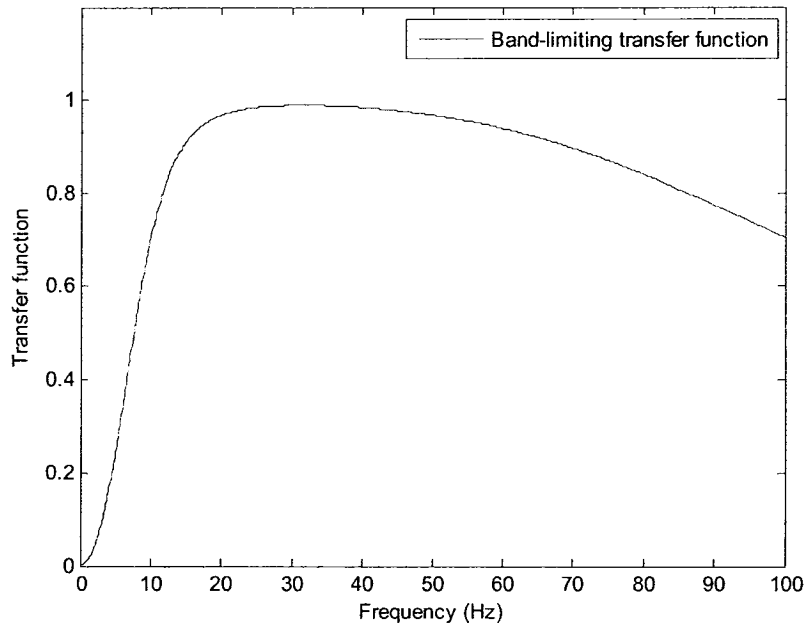

(a)

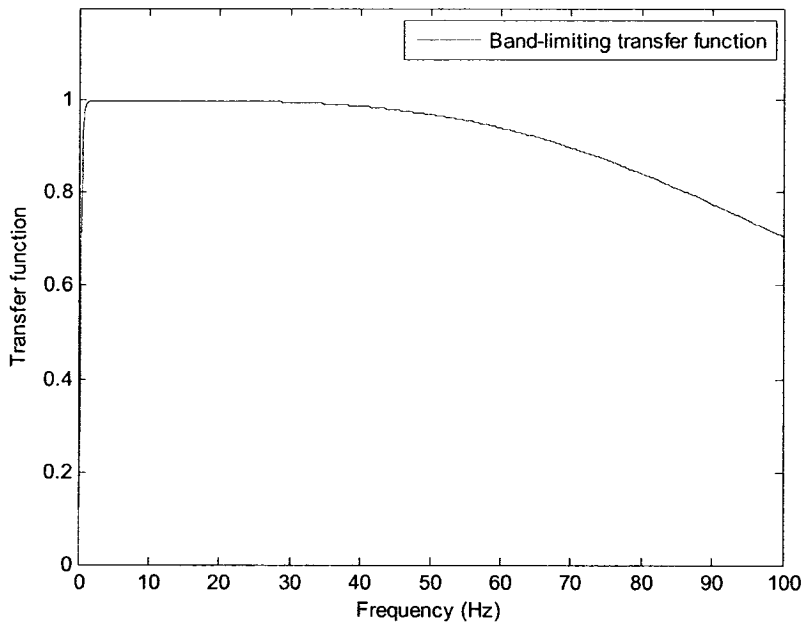

(b)

Figure A.2: Band limiting frequency weighting transfer function: (a) f_1=10 Hz, (b) f_1=10 Hz.

The acceleration-velocity transfer function $H_t(p)$ is expressed as:

$$H_t(p) = \left| \frac{1 + p/\omega_3}{1 + p/(Q_4\omega_4) + (p/\omega_4)^2} \right| \tag{A.4}$$

in which, $\omega_3 = 2\pi f_3$, and $\omega_4 = 2\pi f_4$.

The upward step transfer function $H_s(p)$ is given by:

$$H_s(p) = \left| \frac{1 + p/(Q_5\omega_5) + (p/\omega_5)^2}{1 + p/(Q_5\omega_6) + (p/\omega_6)^2} \left(\frac{\omega_5}{\omega_6} \right)^2 \right| \tag{A.4}$$

Figure A.3 illustrates the acceleration-velocity and the upward step transfer functions. The weighting transfer function is determined from the product of acceleration-velocity and upward step transfer function, $H_t(p).H_s(p)$. Figure A.4 illustrate the weighting transfer function.

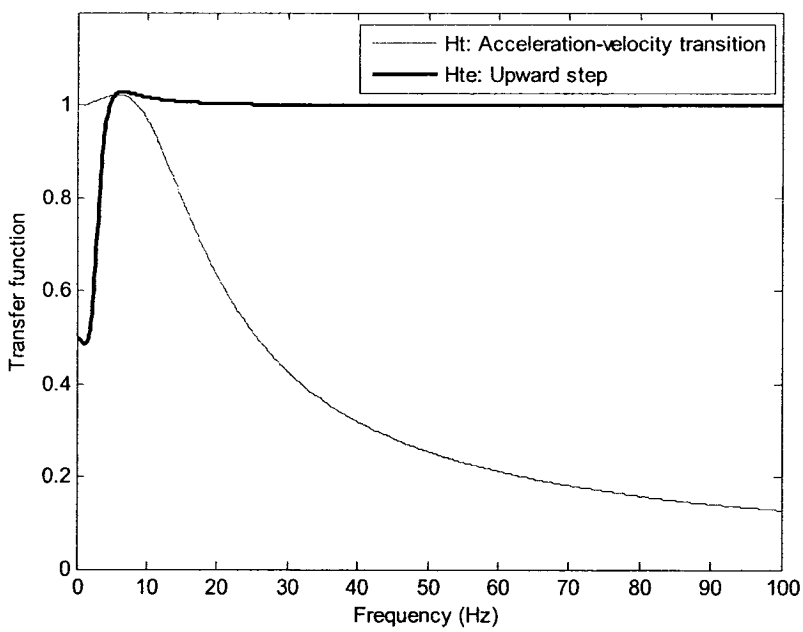

(a)

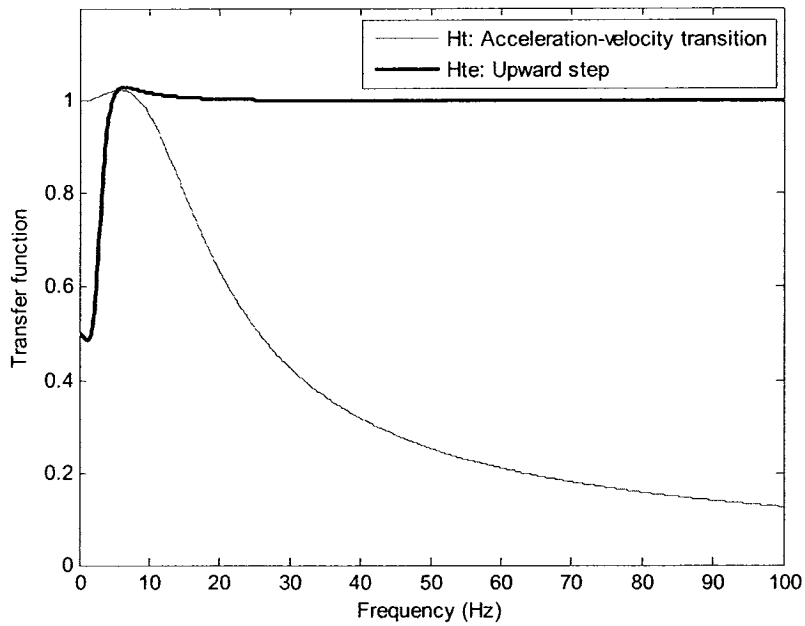

(b)

Figure A.3: Acceleration-velocity and upward step transfer function: (a) f_1=10 Hz, (b) f_1=10 Hz.

The total frequency weighting function is obtained by Eq. (A.5) and is illustrated in Fig. A.6:

$$H(p) = H_h(p).H_l(p).H_t(p).H_s(p) \tag{A.5}$$

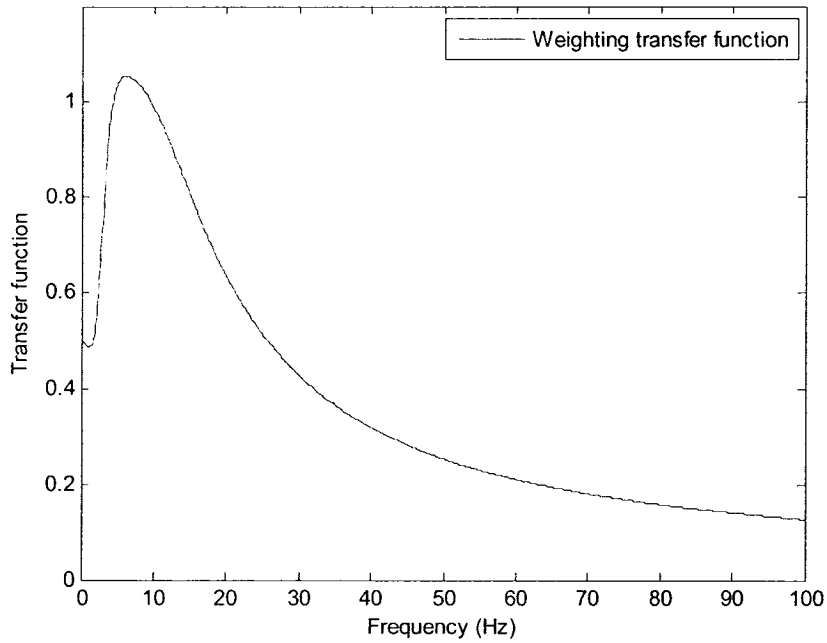

(a)

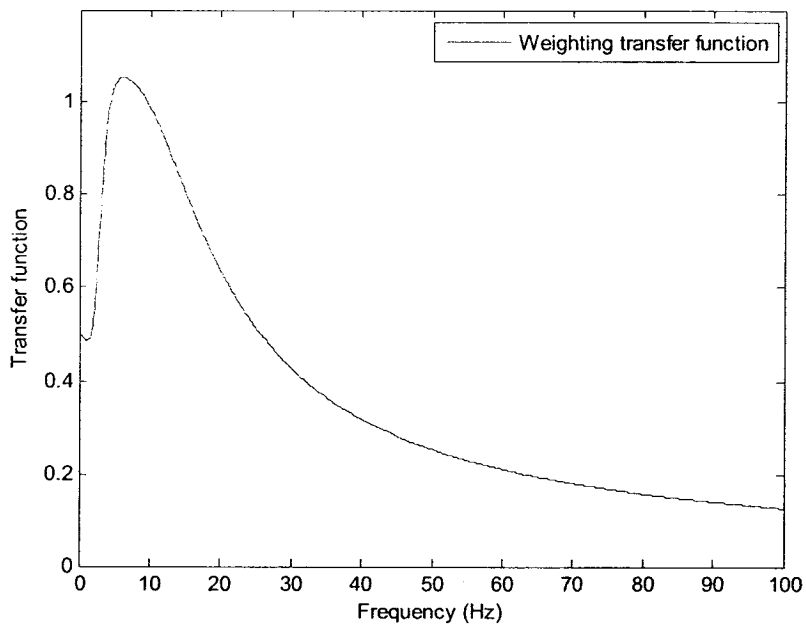

(b)

Figure A.4: Weighting transfer function: (a) f_1=10 Hz, (b) f_1=10 Hz.

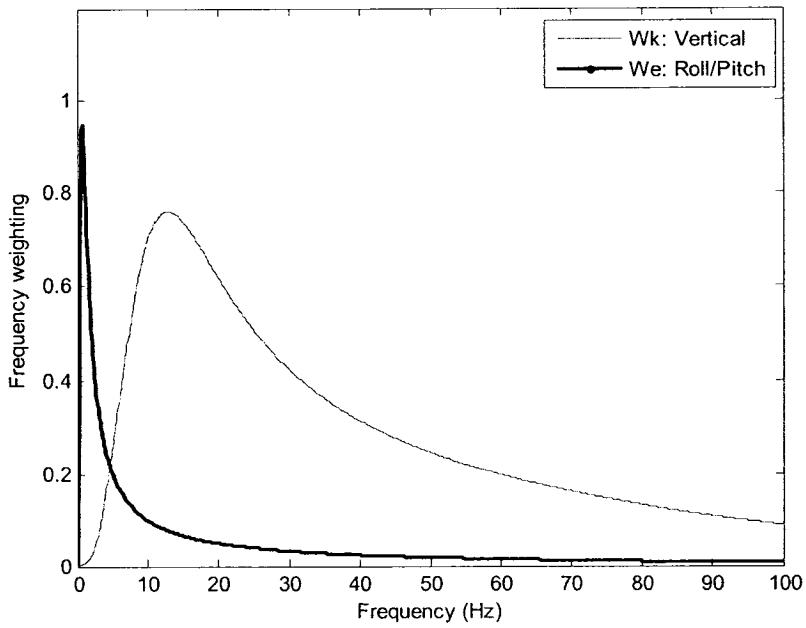

(a)

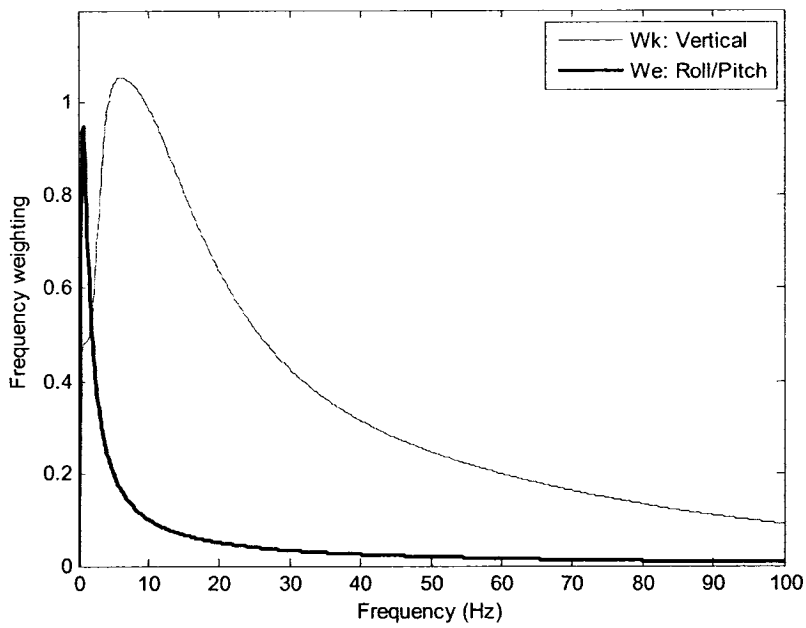

(b)

Figure A.5: Total frequency weighting curves for principal weighting in vertical (W_k) and roll/pitch (W_e) directions: (a) f_1=10 Hz, (b) f_1=10 Hz.